Hyperloop Tube Breach

Analysis of unsteady blast wave effects

Yorrick Bauer

Master of Science Thesis

Delft University of Technology

Aerodynamics, Wind Energy,
Flight Performance and Propulsion

Hyperloop Tube Breach
Analysis of unsteady blast wave effects

Master of Science Thesis

For the degree of Master of Science in Aerospace Engineering at Delft University of Technology

Yorrick Bauer

August 31, 2022

Faculty of Aerospace Engineering · Delft University of Technology

Copyright © Aerospace Engineering, Delft University of Technology
All rights reserved.

Delft University of Technology
Department of
Aerospace Engineering, Delft University of Technology

The undersigned hereby certify that they have read and recommend to the Faculty of Aerospace Engineering for acceptance the thesis entitled

Hyperloop Tube Breach

by

Yorrick Bauer

in fulfilment of the requirements for the degree of

Master of Science Aerospace Engineering

Dated: August 31, 2022

Supervisor(s):

dr.ir. F.F.J. Schrijer

Reader(s):

dr.ir. B.W. van Oudheusden

dr.ir. D. Ragni

Abstract

A loss of vacuum accident in the hyperloop tunnel will likely occur during its operation, and it may have a severe impact on its operational safety. Nevertheless, the hyperloop tube breach has only been researched superficially.

Two aerodynamic phenomena due to the breach are identified: a (quasi-)steady underexpanded jet and an unsteady blast wave. The overpressure due to the confined blast wave impacting the hyperloop vehicles is determined using various methods.

Numerical simulations of the breach applying the 3-dimensional Euler equations show that quasi-1-dimensional (Q1D) approaches only suffice for smaller holes. Although their analytical implementation is less involved than numerical analyses, the Q1D models underpredict the blast wave overpressure, because they cannot account for energy input after the critical shock formation. The (pressure) drag on a vehicle inside the evacuated tube may increase more than an order of magnitude due to the blast wave emanated from the breach location.

Preface

The thesis that you are about to read contains information about my findings on modelling the effects of a hyperloop tube breach. It is the culmination of my work at Delft University of Technology as a student: completing this project feels like the end of an era.

I would like to thank my academic supervisor Ferry Schrijer who guided me through the project. Due to his valuable feedback and help I got back on track when I could no longer see the wood for the trees. I also wish to thank Mark Miedema for the nice discussions we had about the hyperloop and graduation, which were therapeutic for both of us I think. Finally and most importantly, I want to thank my family, friends and colleagues for their patience and support throughout.

I would like to end this preface with a quote:

> Je n'ai fait celle-ci plus longue que parce que je n'ai pas eu le loisir de la faire plus courte. — Blaise Pascal

Yorrick Bauer
Bad Ischl, August 2022

Table of Contents

Abstract **i**

Preface **iii**

List of Figures **viii**

List of Tables **ix**

Nomenclature **xi**

1 Introduction **1**

1.1 Hyperloop development 2
  1.1.1 From conventional trains to hyperloop 2
  1.1.2 From hyperloop to breach 3
1.2 Research questions 4
1.3 Thesis outline 5

2 Hyperloop pod aerodynamics **7**

2.1 Pod flow regime 7
  2.1.1 Compressibility: Mach number 9
  2.1.2 Viscous effects: Reynolds number 10
  2.1.3 Continuity: Knudsen number 10
2.2 Pod-nozzle equivalence 11
2.3 Choking: Kantrowitz limit 12
2.4 Basic drag analysis 15
  2.4.1 Pressure drag 15
  2.4.2 Skin friction drag 17
  2.4.3 Results 18
2.5 State-of-the-art: hyperloop literature study 20

3 Breach aerodynamics **23**

3.1 Steady underexpanded jet 26

3.1.1 Introduction 26

3.1.2 Mach disc 27

3.1.3 Farfield zone 27

3.1.4 Effect of nozzle geometry 28

3.1.5 Discharge coefficient 30

3.2 Unsteady blast wave 34

3.2.1 Euler equations 34

3.2.2 Three dimensional formulation 35

3.2.3 Quasi-one-dimensional formulation 35

3.2.4 Rankine-Hugoniot equations 36

3.2.5 Analytical strong shock 37

3.2.6 Empirical TNT shock relations 39

3.3 State-of-the-art: loss of vacuum accident 42

4 Quasi 1D model **45**

4.1 Riemann shock tube 45

4.2 Shock geometry 47

4.3 Volumetric energy method 50

4.4 Planar method 51

4.4.1 CCW model 51

4.4.2 GSD model 53

4.5 Comparison of Q1D models 53

5 CFD model **57**

5.1 Model setup 57

5.1.1 General settings 58

5.1.2 Initial and boundary conditions 59

5.1.3 Mesh (convergence) 59

5.2 CFD analysis results 61

5.2.1 Pressure contour plots 61

5.2.2 Velocity contour plots 65

5.2.3 Overpressure versus hole size 71

5.3 Comparison of models 74

6 Conclusion **77**

6.1 Model validity 77

6.2 Additional drag due to breach blast wave 78

6.3 Recommendations 78

A Additional information **81**

A.1 Shock between two throats 81

Bibliography **83**

List of Figures

1.1 Artist's rendition of the hyperloop as envisioned by Hardt Hyperloop. 1
1.2 Thesis outline. 6

2.1 Conceptual pod design provided by Hardt Hyperloop (above) with its axially varying cross-sectional area (below). 8
2.2 Flow regimes dictated by the Knudsen number. (From: Moss and Bird [2003]) . 11
2.3 Left to right: moving pod, pod frame, convergent-divergent nozzle. 11
2.4 Pressure ratio of isentropic and Kantrowitz limited flow for varying blockage ratios. 14
2.5 A nozzle with two throats and a normal shock wave (NSW). 16
2.6 Results of the drag analysis during normal operation. 19
2.7 Blockage ratio versus freestream Mach number and resulting maximum Mach number due to the blockage. (From: Opgenoord and Caplan [2018]) 20
2.8 Rapid drag increase beyond the Kantrowitz limit. (From: Opgenoord and Caplan [2018]) 20

3.1 Introduction to the phenomenology. 23
3.2 The initial stages of the developing underexpanded jet. (From: Vuorinen et al. [2013]) 25
3.3 Schematic representation of the initial breach. (From: Radulescu and Law [2007]) 25
3.4 Highly underexpanded jet. (From: Franquet et al. [2015]) 26
3.5 A notational nozzle may be used to omit computing the nearfield zone. (From: Franquet et al. [2015]) 28
3.6 Schlieren images of free jets from a nozzle with 5.0 aspect ratio at pressure ratios **a.** 2.9; **b.** 5.2; **c.** 10.3; **d.** 20.3. (From: Rajakuperan and Ramaswamy [1998]) . 29
3.7 Exaggerated view of a vena contracta (v.c.) after an orifice. 29
3.8 The coefficient of contraction for axisymmetric orifices depends on the pressure ratio. (From: Patterson et al. [1970]) 30

3.9 Comparison of methods to derive the discharge coefficient dependence on pressure ratio for a sharp-edged axisymmetrical orifice. 32
3.10 Blast wave by nuclear explosion. (Photo by: Berlyn Brixner [1945]) 34
3.11 Friedlander curve showing the overpressure due to a blast wave. 38
3.12 Comparison of free field decay laws. 40
3.13 Flow velocity fields in the torus and air jet contour 1 s after initial inflow. (From: Gélain et al. [2015]) 43

4.1 Geometry of a Riemann shock tube problem. 45
4.2 The (x, t)-diagram showing the developing expansion wave and shock wave. . . . 46
4.3 Critical shock definition. 47
4.4 Spatiotemporal development of a confined spherical blast wave. 48
4.5 Free-field and 1D overpressure decay. 49
4.6 Chisnell function evaluated for pressure ratios larger than unity. 52
4.7 Final shock pressure for a 1 m diameter tunnel depending on the hole size. . . . 52
4.8 Blast wave decay models compared for four breach hole sizes. 54

5.1 The mesh geometry of a 30 cm radius breach hole setup. 58
5.2 The pressure development along the tunnel center line for several mesh refinements. 60
5.3 Tube pressure contour plots in time domain $0 \leq t \leq 10$ ms with 1 ms time step showing the blast wave development. 64
5.4 Tube velocity magnitude contour plots in time domain $0 \leq t \leq 10$ ms with 1 ms time step showing the blast wave development in the tube midplane. 68
5.5 Tube velocity magnitude contour plots of the tube top view in time domain $4 \leq t \leq 10$ ms with 1 ms time step showing the blast wave development near the walls. 70
5.6 The pressure distribution along the pod axis for three different breach holes (at small overpressures). 72
5.7 The pressure distribution along the pod axis for three different breach holes (at large overpressures). 73
5.8 Comparison of results obtained by Q1D models and the CFD model. 75

6.1 Comparison of total aerodynamic drag during normal operation and due to a tube breach. 79

A.1 A nozzle with two throats and a normal shock wave (NSW). 82

List of Tables

2.1 Overview of physical and design parameters. 9

4.1 Breach initial conditions. 47

5.1 Overpressure results for each of the analysed hole diameters. 71

6.1 Model strengths and weaknesses. 78

Nomenclature

List of Abbreviations

1D	one-dimensional
3D	three-dimensional
CCW	Chester–Chisnell–Whitham
CD	contact discontinuity
CFD	computational fluid dynamics
CFL	Courant–Friedrichs–Lewy
GSD	geometric shock dynamics
ECF	energy concentration factor
JB	jet boundary
LES	large eddy simulation
LOVA	loss of vacuum accident
MOC	method of characteristics
ODE	ordinary differential equation
OSW	oblique shock wave
PDE	partial differential equation
Q1D	quasi-one-dimensional
RANS	Reynolds-averaged Navier–Stokes

TE	trailing edge
TNT	trinitrotoluene, $C_6H_2CH_3(NO_2)_3$
TP	triple point
TvNS	Taylor–von Neumann–Sedov
v.c.	vena contracta

List of Symbols

Latin Symbols

ℓ	mean free path
$\mathcal{H}$	Heaviside step function
A	Area
a	speed of sound
C_d	discharge coefficient
c_f	friction coefficient
c_p	specific heat capacity at constant pressure
c_v	specific heat capacity at constant volume
D	diameter or drag
E	energy
f	Chisnell function
h	specific enthalpy
L	length
M	Mach number
n	energy concentration factor (ECF)
p	pressure
R	air gas constant or blast radius
T	temperature
t	time
U	velocity magnitude
V	volume
W	TNT mass
x	axial position
Z	reduced distance, $R/\sqrt[3]{W}$
Kn	Knudsen number
Re	Reynolds number

Greek Symbols

β	blockage ratio, OSW angle, or constant

Δ	difference operator
δ	boundary layer thickness
γ	specific heat ratio, c_p/c_v
κ	contraction coefficient
μ	dynamic viscosity or post-shock Mach number
ϕ	friction coefficient
π	3.141592. . .
ρ	density
τ	shear stress
θ	OSW deflection angle or shock incident angle
ε	yield energy
ζ	overpressure, $\Delta\ p/p_0$

Subscripts

∞	far field
e	exit
p	peak or pod
s	shock
0	initial or stagnation
H	Henrych
KG	Kinney–Graham
MD	Mach disk
req	required
TvNS	Taylor–von Neumann–Sedov
t	tube

Superscripts

$\star$	critical

Other

$[x]$	$x_2 - x_1$
$\cdot$	time rate of change, d/dt
$\partial/\partial x$	partial derivative with respect to x
'	derivative

Chapter 1

Introduction

The hyperloop concept in Figure 1.1 is an attempt to combine the convenience of trains with the speed of aircraft. Its magnetically levitated vehicles (pods) are propelled to transonic speeds through a tunnel operating under near-vacuum conditions. This low pressure environment reduces energy losses due to drag, but requires a completely new infrastructure.

HARDT
HYPERLOOP

Figure 1.1: Artist's rendition of the hyperloop as envisioned by Hardt Hyperloop.

Even though the hyperloop concept once realised may offer great opportunities, it is not without critics exposing its weak points. One of the major threats is the inherent risk of a tunnel leakage, in which case ambient air flows into the low-pressure tunnel. Although the occurrence of a sudden leakage (tube breach) during the operational lifetime is certain, the expected impact is still unknown.

This is primarily because the hyperloop concept has not been studied as extensively as conventional (or established) modes of transport: the lack of a full-scale realisation and the use of many components with low technology readiness level render physical experiments more expensive. Most published hyperloop research focuses on normal operation of the hyperloop. It is vital, however, to also ensure passenger safety during emergencies, such as a tube breach scenario. Forecasting the effects of a tube breach by aerodynamic modelling is thus important and this forms the core of this thesis.

This introductory chapter gives an account of the evolution from hyperloop precursors to its current state, in an attempt to transfer the state-of-the-art from one field to the other. The extrapolation is however not straightforward. Section 1.1 also refers to the current industry vision on breach safety, reiterating the above-mentioned lacking but important research. The specific research questions for this thesis are discussed in Section 1.2 and the report is outlined at the end of this chapter, in Section 1.3.

1.1 Hyperloop development

The overarching concept of the hyperloop is not new. Aerospace engineer Robert Goddard is often credited as founder of the modern vacuum train (or vactrain, in short). His sketches, posthumously patented to his wife (Goddard [1945]), date back to 1904.

Later, companies such as SwissMetro [1999], TransPod (Janzen [2017]), Rand (Salter [1972]) and Evacuated Tube Transport Technologies (ET3, Oster et al. [2011]) further developed the vactrain design, although they never realised a fully operational system. Then, entrepreneur Elon Musk [2013] adopted and popularised the vactrain design in his white paper, renaming it the Hyperloop.

1.1.1 From conventional trains to hyperloop

Alternative research fields have to be consulted due to the lack of published papers on the topic of hyperloop with its economic potential. Public research on conventional high-speed trains presents such an alternative. Both the transonic hyperloop and the conventional high-speed trains research domains share their interest in obtaining high velocities on a predetermined route. The following attempts to project the implications of the research of high-speed trains onto the hyperloop domain.

Raghunathan et al. [2002] argue that the goal of increasing train speed was typically realised by increasing power input rather than by reducing aerodynamic drag. This practise inevitably led to high energy losses, since drag grows quadratically with speed. High-speed train designs could no longer ignore the energy losses. Hence noise, passenger discomfort and impulse waves due to oncoming trains and tunnels became areas of interest.

Takayama et al. [1995], for instance, discuss the pressure variations and tunnel sonic boom for their 1:300 scaled model. This weak shock wave occurs when compression waves coalesce. They propose two ways to reduce the shock overpressures. First, an entrance hood prevents the coalescence of the compression waves. This only works for compression waves which have relatively small overpressures. The other method, more suitable for high speeds, is to perforate the tunnel walls. The shock wave strength is reduced due to the mass suction, and thus momentum and energy loss.

Takayama et al. [1995] conclude a combination of both methods can reduce the peak overpressure in the scaled model up to 80% at high speeds. Extending this design reasoning to the hyperloop: a shock wave in a hyperloop tube could theoretically be weakened by perforating the tube adding an outer tube.

Baron et al. [2001] investigated high-speed trains in "very long tunnels". Specifically, they used a quasi one-dimensional numerical simulation for trains travelling at 120 m/s in a 60 km tunnel. A small tunnel diameter is preferred as they are "tentatively proportional" to the construction costs. However, the higher blockage ratio then leads to higher propulsion costs. This trade-off is also encountered in the hyperloop design. A 52% blockage ratio (i.e. pod to tube cross-sectional area ratio) already produces supersonic air flows at standard atmospheric pressure. They show that reducing the tunnel diameter by a factor of 2 leads to the required power increase by a factor of 7. Not wanting to lower the cruise speed, Baron et al. [2001] therefore also propose to create a partial vacuum at 10 kPa, which is still 100 times greater than the proposed hyperloop pressure. Instead of the perforated walls, they employ pressure relief ducts to a parallel tunnel, creating a two-way connection. They note that this configuration is also found in the Channel tunnel. Large unsteady aerodynamic loads due to trains travelling in opposite direction form a disadvantage to this tunnel network. Finally they note that the air temperature rises with at least 40 K. This does not present an urgent problem as the tunnels are underground, which offers a thermal reservoir. This is not the case if the tunnel is built above ground level and it may then require a cooling system.

1.1.2 From hyperloop to breach

All hyperloop concepts have one fundamental physical advancement in common: they reduce the aerodynamic drag of the vehicles by depleting their environment from most of the air. Even though the depressurisation and retention of a partial vacuum require energy and the tunnel infrastructure adds to the total project cost, it is asserted that it is still less expensive compared to current alternatives such as train and air travel. Additionally, the proposed transonic speeds are comparable to those of aircraft. Note that the hyperloop operates at only a *partial* vacuum of about 100 Pa or 1/1000 of standard sea level pressure, because a higher vacuum requires too much pumping complexity for its possible benefits. However, the downside of this approach is that the total pressure and thus pressure drag rises when transonic speeds are achieved due to an internal choking effect known as the Kantrowitz limit, (named after Kantrowitz and Donaldson [1945]) which is discussed in Section 2.3.

Although the hyperloop design offers many advantages over conventional transportation methods, simultaneously it presents safety risks which need to be addressed. One major concern is a loss of vacuum accident. That is, the low-pressure tunnel may become damaged, such that air leaks into the tube.

In order to shed light upon the current available notion of safety of the hyperloop, the FAQ section of two prominent hyperloop developers is consulted:

> Pods will continue to travel safely to the next portal even with a large breach. Our response to a breach would be to intentionally repressurize the tube with small valves places along the route length while engaging pod brakes to safely bringing all pods to rest before it is deemed safe to continue to the next portal. A sustained leak could impact performance (speed) but

> would not pose a safety issue due to vehicle and system architectural design choices. This assessment is based in solid understanding and analysis of the complex vehicle load behaviors during such an event. — Virgin Hyperloop One [2020]

> The only way in which a substantial breach in the tube would occur, as the tube construction is extremely strong, is in a case of major impact. This concerns risks to which every infrastructure is subject. As with any form of transport, in such a case it would be desirable to shut down the line in which the breach occurred until the calamity has been solved. The pipes are segmented, with air seals located every couple kilometers, so that in the event of a leak, this can be limited to a certain area. By means of sensors along the infrastructure that measure the pressure the vehicles will be notified. The intervehicle communications system allows vehicles to act as one and immediately and jointly brake, leaving no room for human error. The emergency braking system will know a deceleration that you can expect during any emergency stop of other modalities. As air would vastly flow into the tube creating an environment equivalent to that of the atmosphere around us, the increase in air resistance will help the vehicles to naturally slow down. Due to the pressure level in the tube this impact will be gradual. — Hardt Hyperloop [2020]

In short, the risk is mitigated with a focus on emergency brakes and pipe segmentation. Hyperloop TT and Transpod do not specifically mention a vacuum breach, but about safety in general they concentrate on benefits of automation and the insurability of the project. Shifting to governmental documentation, the Ministry of Infrastructure and Environment of the Netherlands commissioned a report about the applications of the hyperloop concept in the Netherlands. They acknowledge that the hyperloop tube "poses safety related issues that need to be addressed. But no fundamental showstoppers are currently foreseen." (Arup et al. [2017]) Unfortunately, in all cases a thorough quantitative analysis substantiating the claims is lacking.

Thus, despite the accelerated development of and new excitement for the hyperloop, one aspect remains invariably neglected: safety. Still, the tunnel structure is as accessible as conventional train tracks, increasing the likelihood of damage due to weather influence or even malicious actors. Even more than conventional railway transport systems, however, the hyperloop could be prone to cascading failures due to the enclosed low-pressure environment. Hence, the present research aims to support the development of a safe hyperloop and to cover part of its corresponding current research gap.

1.2 Research questions

The contextualisation of the hyperloop tube breach above implies that thorough analyses of its effects have not been publicised. Critics think a breach is devastating, whereas investors who claim the hyperloop is safe, think a tube breach is a hurdle easily overcome by leak detectors, increased vacuum pump power and emergency brakes. The research gap described by this juxtaposition forms the basis of this thesis' research objective and research questions.

The research objective is to offer hyperloop developers recommendations concerning how to improve their design for safety in case of a loss of vacuum in the tube by developing a validated design tool analysing the unsteady aerodynamic forces in such a scenario.

The main question of the thesis is formulated as follows:

What are the additional aerodynamic forces on hyperloop pods that may be expected in case of a given near-vacuum tube breach scenario according to a validated one-dimensional analysis?

This question is split into six sequential sub-questions:

1. *What are the aerodynamic forces on hyperloop pods during normal operation?*

   Before the additional forces are analysed it is wise to first analyse the aerodynamic forces on a normally operating hyperloop.

2. *What are the typical aerodynamic phenomena expected during a tube breach?*

   Identification and exploration of the problem is the next step into solving the main research question.

3. *What models are useful to simulate those typical phenomena?*

   The now expected phenomena can be analysed using models. Models simplify the problem: too simple yields inaccurate results, and too complex yields computationally expensive results. A trade-off decides what is important and what may be neglected.

4. *What is the (spatiotemporally varying) overpressure magnitude throughout the tube caused by a given breach scenario according to those models?*

   Now applying the models allows to quantitatively analyse the breach and find the overpressure necessary to find additional forces.

5. *What is the accuracy of the predictions made by the one-dimensional model?*

   The quasi-one-dimensional (Q1D) model is verified with an inviscid computational fluid dynamics (CFD) analysis. Hence, two models are required by the research questions: a Q1D analysis tool and a three-dimensional (3D) inviscid CFD verification. The simpler model is developed in the programming language Python. The more sophisticated CFD analysis is done with Ansys software.

6. *What is the magnitude of the expected additional forces?*

   Generally, a Q1D model supported with CFD is used for these conditions. The overpressure due to a breach then yields additional forces.

1.3 Thesis outline

This thesis is set up as shown in Figure 1.2 on the next page. The top items are more general than the bottom items. The lower items lean on the ideas discussed in the upper items. Pod aerodynamics and breach aerodynamics are separately discussed but they eventually merge in the conclusion. These two chapters conclude with a brief literature review of the state-of-the-art. The link between the steady jet and the Q1D model is weak: it only pertains to the discharge coefficient description.

First, Chapter 2 discusses the aerodynamic theory required to estimate the drag force on the pod under normal operations. Once the flow regime has been identified, isentropic flow is used to describe how phenomena such as the Kantrowitz limit increase the drag. Ultimately, the drag is estimated using the pressure distribution and a basic skin friction model.

Then, Chapter 3 identifies two aerodynamic phenomena occurring due to a sudden leak: the unsteady blast wave and steady underexpanded jet. General models of both phenomena are discussed, which form the basis of the models specific for the hyperloop in the next chapters.

Next, Chapter 4 quantifies the unsteady blast wave for several hyperloop tube breach scenarios using three distinct (quasi) one-dimensional (Q1D) approaches: Riemann shock tube, TNT-equivalency and geometric shock dynamics. Chapter 5 compares those models to a three-dimensional (3D) computational fluid dynamics (CFD) results applying the Euler equations.

Finally, Chapter 6 discusses the results and answers the main research question. Furthermore, it proposes several recommendations for further research.

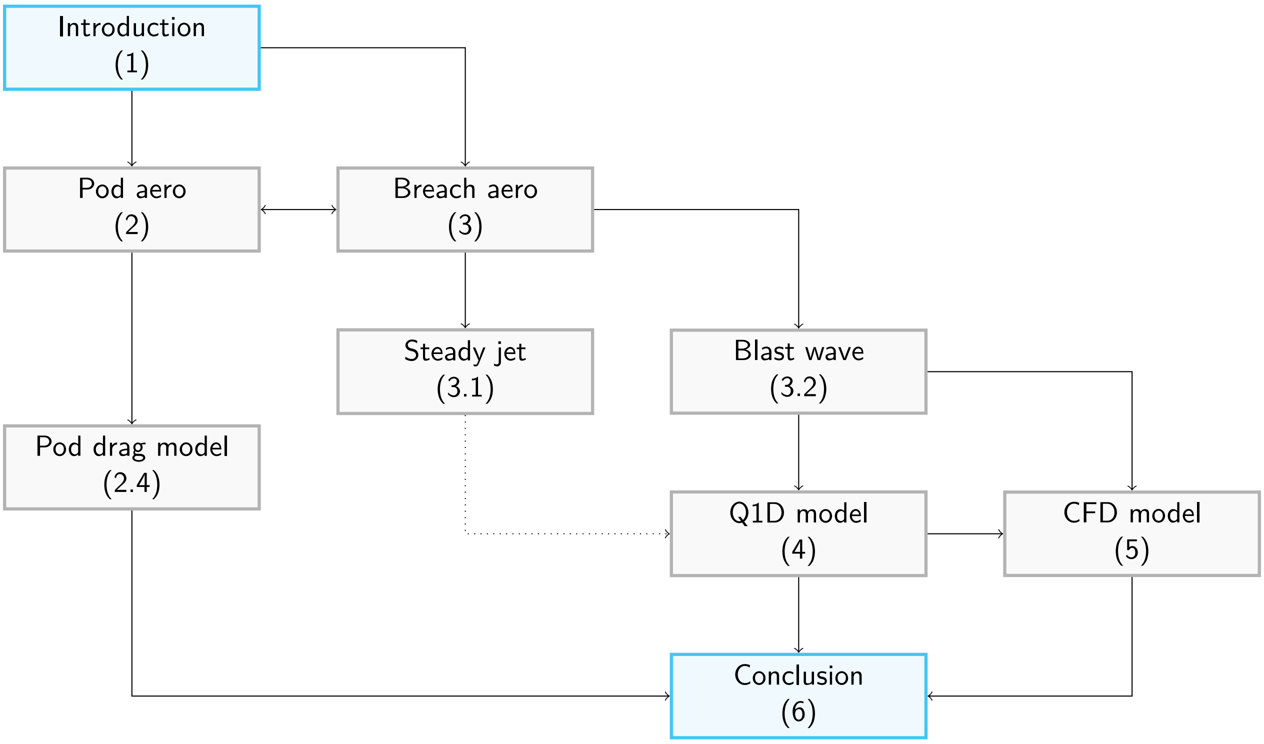
Introduction
(1)
Pod aero
(2)
Breach aero
(3)
Steady jet
(3.1)
Blast wave
(3.2)
Pod drag model
(2.4)
Q1D model
(4)
CFD model
(5)
Conclusion
(6)

Figure 1.2: Thesis outline.

Chapter 2

Hyperloop pod aerodynamics

This chapter addresses the first research sub-question: *What are the aerodynamic forces on hyperloop pods during normal operation?* To this end, aerodynamic theory is applied to the hyperloop pod. First an overview of relevant parameters is given. These parameters may then be used to derive that the flow around the pod is viscous, compressible and a continuum. It is thus required to analyse the flow with isentropic relations. This leads to an exploration of the phenomenon called the Kantrowitz limit. Synthesising all previous information, an estimation of the drag on the pod is computed and compared with literature approaches.

2.1 Pod flow regime

Identifying the flow regime of a hyperloop pod during normal operation (cruise) offers important information. First of all because this categorisation shows which models are valid and which ones lead to large errors. Secondly, these models turn out to be applicable to the breach modelling subsequently as well.

Identification is done with dimensionless similarity parameters such as the Reynolds, Mach and Knudsen number, which depend on geometry and fluid properties. However, no full-scale hyperloop system exists, besides proof-of-concept prototypes. The proposed values are therefore indicative and represent the current state-of-the-art sufficiently, such that flow regime can be identified. In other words: the following hyperloop design parameters reflect reasonable order of magnitude estimates based on current design consensus.

The geometry of the pod and tunnel in particular vary widely. The following pod design provided by Hardt Hyperloop is analysed in this thesis, see Figure 2.1. The pod maximum diameter D_p is 0.84 m, its length is 6 m and it travels at U 300 m/s. Hardt suggested for their pod design approximately 70% blockage ratio to yield a tube diameter of 1.0 m. The cross-sectional area of the pod A_p, the tube area A_t and the bypass area $(A_p - A_t)$ varying with axial position x are then shown in Figure 2.1 below.

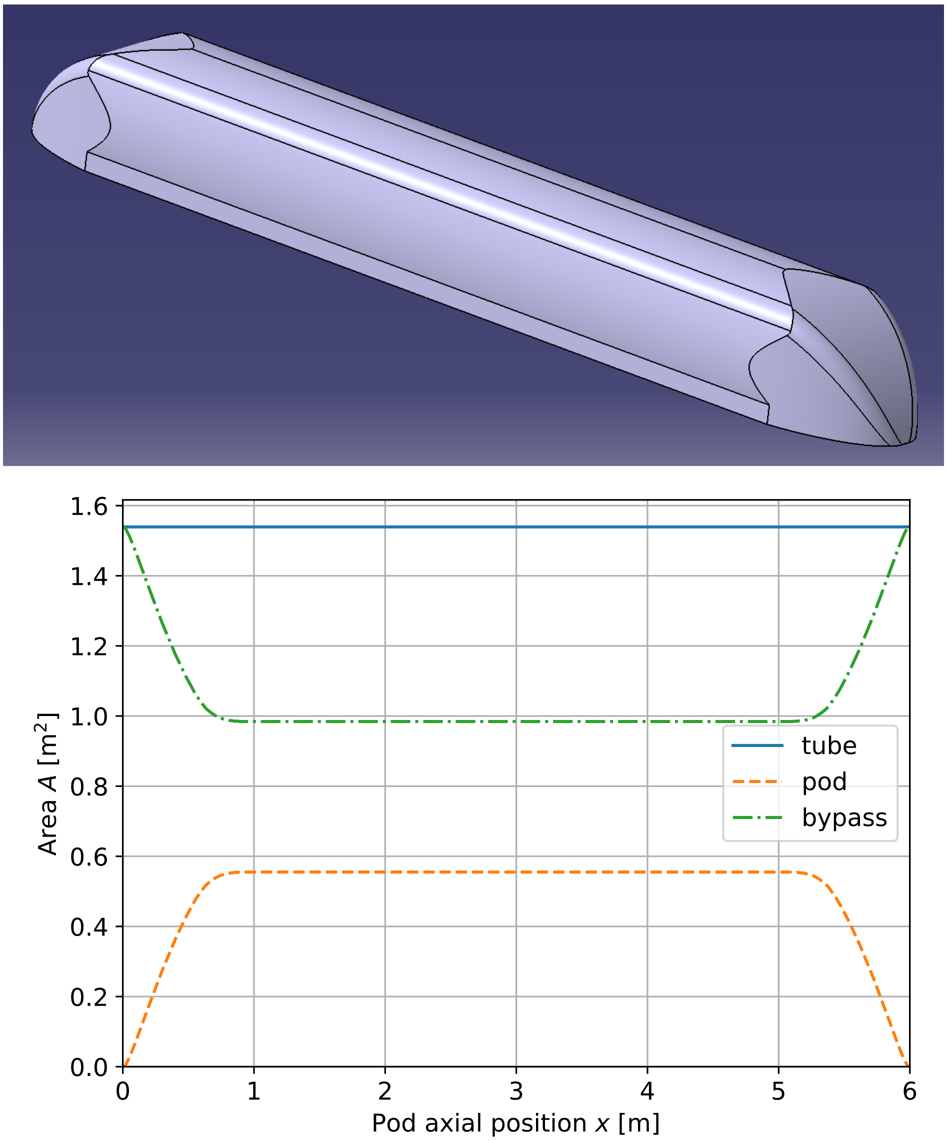

Figure 2.1: Conceptual pod design provided by Hardt Hyperloop (above) with its axially varying cross-sectional area (below).

The hyperloop tube operational pressure p is approximately 100 Pa or a thousandth of standard atmospheric conditions at sea level. This pressure is a trade-off between reducing drag losses and increasing vacuum pump requirements.

Without active thermal control, the tube is in thermal equilibrium with the ambient environment. The ambient air temperature at standard sea level conditions is 15 °C or 288 K. This is then equal to the tube air temperature T. Using Sutherland's law, the dynamic viscosity of air μ at this temperature is 1.8 × 10^{-5} Pa s. Note that the viscosity is independent of pressure.

Applying the ideal gas law ($p = \rho RT$) reveals that the air density ρ is also a thousandth of the atmospheric air density, i.e. 1.2 × 10^{-3} kg/m^3. The specific gas constant for air R is 287 J/(kg K). The specific heat ratio γ is 1.4 for air.[1] The speed of sound is then $a = \sqrt{\gamma RT} = 340$ m/s.

Table 2.1 summarises the physical properties of air and (geometric) design parameters. These parameters allow to estimate the similarity parameters, which characterise the flow regime.

Table 2.1: Overview of physical and design parameters.

	Parameter	Symbol	Value	Unit
Air	Gas constant	R	287	J/kg K
	Specific heat ratio	γ	1.4	-
	Dynamic viscosity	μ	1.8E-5	Pa s
	Speed of sound	a	340	m/s
Tube	Diameter	D_t	1.0	m
	Pressure	p	100	Pa
	Temperature	T	288	K
	Density	ρ	1.2E-3	kg/m^3
Ambient	Pressure	p_0	101325	Pa
	Temperature	T_0	288	K
	Density	ρ_0	1.225	kg/m^3
Pod	Length	L	6.0	m
	Speed	U	300	m/s
	Diameter	D_p	0.84	m

Three similarity parameters are discussed to describe the flow regime and to simplify the general conservation laws: the Reynolds number, Mach number and Knudsen number. They are appropriate for e.g. steady single-species gas flows where electromagnetic, thermal and gravity effects are small. They provide information on the compressibility, viscous effects and continuity of the flow, respectively.

2.1.1 Compressibility: Mach number

The Mach number M represents the ratio of the flow velocity U and the speed of sound a,

$$M \equiv \frac{U}{a} = 0.88$$

---

[1] This is the ratio of specific heat at constant pressure c_p over the specific heat at constant volume c_v.

The hyperloop pods travel at transonic speeds, i.e. $M \approx 1$. Hence, the compressibility of the fluid has to be considered. This means that the isentropic relations have to be employed instead of the simpler incompressible Bernoulli equation.

Moreover, shock waves may occur when the Mach number exceeds unity. They are discussed in Section 3.2. Note that although the pod travels at subsonic speeds, locally the air velocity may exceed the speed of sound.

Further, the tunnel temperature may vary, which also affects the speed of sound, although this contribution is likely smaller. For example, a temperature rise or fall of 30 °C constitutes a 10% change in absolute temperature, but only affects the speed of sound by 5% due to the square root proportionality ($a \propto \sqrt{T}$).

2.1.2 Viscous effects: Reynolds number

The Reynolds number Re is defined as the ratio between the inertial and viscous forces, mathematically

$$\mathrm{Re} \equiv \frac{\rho U L}{\mu} = 1.2 \times 10^5$$

With density ρ, velocity U, characteristic length L and dynamic viscosity μ. Using the length of the pod as characteristic length, the Reynolds number of the air around the pod is $\mathrm{Re} = \mathcal{O}(10^5)$. Direct numerical simulations at this large Reynolds number are computationally too expensive. Moreover, turbulent flows may typically be found in this high Reynolds number flow regime.

Note that the flow approaches zero velocity near the walls due to viscous forces, i.e. the no-slip condition. This also implies that the Reynolds number can become arbitrarily small near the walls. This is why it is useful to split the flow into a viscous boundary layer near the walls and inviscid flow in the remaining flow, further discussed in Section 3.2.

Furthermore, note that the characteristic length also approaches zero towards the leading edge. This is why laminar flow can be expected near the nose of the pod. The transition zone from laminar to turbulent flow is generally hard to model. A relatively simple approach is used in Section 2.4.

2.1.3 Continuity: Knudsen number

The final dimensionless parameter discussed is the Knudsen number Kn, which is defined as the ratio of the mean free path ℓ to the characteristic length scale. It can be shown that the Knudsen number is related to the Reynolds number and Mach number as follows

$$\mathrm{Kn} \equiv \frac{\ell}{L} = \frac{M}{\mathrm{Re}}\sqrt{\frac{\gamma\pi}{2}} = 1.1 \times 10^{-5} \ll 1$$

The air thus may be modelled as a continuum rather than a rarefied gas. This is due to the fact that the Knudsen number is well below unity, i.e. the mean free path of a fluid element is much smaller than the characteristic length scales. Moreover, the slip at the walls is indeed negligible in this flow regime and the no-slip condition remains valid.

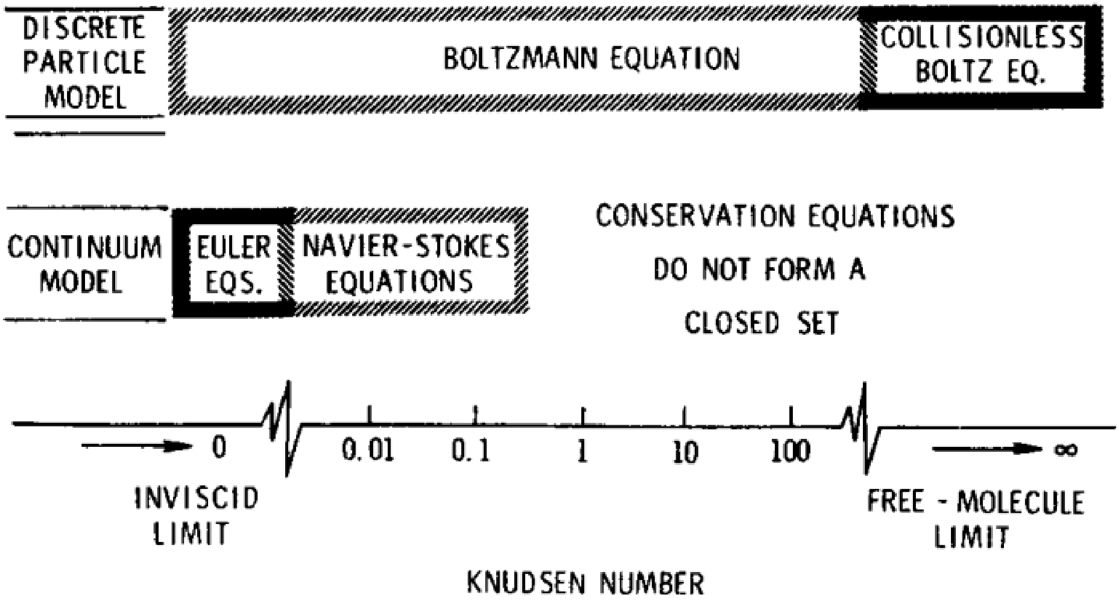
DISCRETE PARTICLE MODEL
BOLTZMANN EQUATION
COLLISIONLESS BOLTZ EQ.
CONTINUUM MODEL
EULER EQS.
NAVIER-STOKES EQUATIONS
CONSERVATION EQUATIONS DO NOT FORM A CLOSED SET
0
0.01
0.1
1
10
100
∞
INVISCID LIMIT
FREE - MOLECULE LIMIT
KNUDSEN NUMBER

Figure 2.2: Flow regimes dictated by the Knudsen number. (From: Moss and Bird [2003])

The hyperloop tube may be referred to as a vacuum tunnel. However, different vacuum qualities exist, and the 100 Pa absolute pressure in the tube is only a low (rough) vacuum. This is far from a perfect vacuum of 0 Pa absolute. In fact, more extreme vacua have been achieved in lab setups below 10^{-9} Pa.

Figure 2.2 graphically represents an overview of the four flow regimes dictated by the Knudsen number, which are in order of stronger vacua: continuum, slip flow, transitional and free molecular flow. The Navier–Stokes equations hold for $Kn < 0.2$ but for $Kn > 0.03$ the no-slip condition becomes the velocity- and temperature-slip condition. The free molecular flow for $Kn > 1$ is characterised by "individual molecular impacts" (Anderson Jr. [2006]).

In summary, the flow inside the hyperloop can be characterised as a continuum, but is compressible and may contain shocks. Also, inviscid flow occurs only outside the viscous boundary layers. The characterisation of the hyperloop pod flow initiates the analysis of the aerodynamic forces during normal operation and isentropic flow seems an apt model. The next section outlines an implementation method.

2.2 Pod-nozzle equivalence

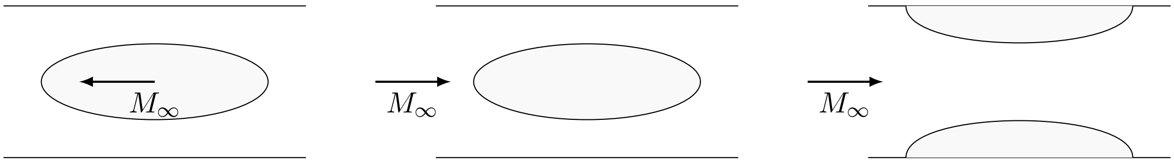
M_∞
M_∞
M_∞

Figure 2.3: Left to right: moving pod, pod frame, convergent-divergent nozzle.

The hyperloop pod may be modelled as a convergent-divergent nozzle. Figure 2.3 illustrates the equivalence for a quasi-one-dimensional (Q1D)[2] case. On the left is the lab reference frame, in which the vehicle travels through the hyperloop tunnel at Mach number M_∞. Equivalently, in the reference frame of a passenger aboard the hyperloop, the pod is stationary while air is approaching at M_∞. This is similar to a wind tunnel setup. This change of reference frame allows for a direct relation between the pod Mach number and the total pressure. The isentropic flow relations are presented in the next section.

In absence of boundary layers, walls of the pod may be superimposed on the tunnel walls. This superposition creates the convergent-divergent nozzle structure, displayed on the right. The far-field Mach number M_∞ remains the same. Note that the pod thus effectively decreases the area through which the air has to travel. This is the bypass, which in this reference frame acts as the nozzle throat.

The pressure drag on a pod can now be determined solely based on the tube pressure and pod velocity and geometry.[3] Specifically, if the cross-sectional area of the pod varying with pod position (from nose to tail) $A_p(x)$ is known, then the pressure distribution $p(x)$ on the pod can be found using the Mach number distribution $M(x)$. Choked flow and the Kantrowitz limit must be discussed in order to assess this methodology in more detail.

2.3 Choking: Kantrowitz limit

The isentropic flow relations are

$$\frac{T_0}{T} = 1 + \frac{\gamma - 1}{2} M^2 \tag{2.1a}$$

And

$$\frac{p}{p_0} = \left(\frac{T}{T_0}\right)^{\frac{\gamma}{\gamma-1}} = \left(\frac{\rho}{\rho_0}\right)^{\gamma} \tag{2.1b}$$

The 0 subscript refers to total (i.e. stagnant) conditions, obtained when the air flow is brought to rest isentropically. These relations with the ideal gas law may be substituted into the one-dimensional (1D) mass flow equation. This yields for the (constant) mass flow $\dot{m}$

$$\dot{m} = \rho A U = A p_0 M \sqrt{\frac{\gamma}{R T_0}\left(1 + \frac{\gamma - 1}{2} M^2\right)^{-\frac{\gamma+1}{\gamma-1}}} \tag{2.2}$$

This shows that the mass flow depends linearly on the nozzle cross-sectional area A and the ambient (stagnant) pressure p_0 and inversely on the square root of the ambient (stagnant) temperature T_0. Also, the heat capacity ratio γ and air gas constant R offer proportionality constants since they are constant for the considered temperature range.

---

[2] The model is *quasi*-1-dimensional, because although the variables are considered in only one (x-)coordinate, it also considers the cross-sectional area A. It is valid to neglect two-dimensional effects if changes in A(x) are small. (Anderson [2003])

[3] Note that viscous effects such as a boundary layers are not taken into account. As it turns out later in Section 2.4.3, the skin friction is negligible with respect to the pressure drag.

The mass flow can be increased by lowering the downstream pressure, until the maximum mass flow has been obtained at Mach 1:

$$\dot{m}^\star = A^\star p_0 \sqrt{\frac{\gamma}{RT_0}\left(\frac{2}{\gamma+1}\right)^{\frac{\gamma+1}{\gamma-1}}} \tag{2.3}$$

Due to mass continuity, the sonic ($M = 1$) conditions occur at the minimum nozzle cross-sectional area, the throat $A^\star$. In case of a pod, this is the minimum bypass area. The flow is choked at the critical (downstream) pressure $p^\star$,

$$p^\star = p_0 \left(\frac{2}{\gamma+1}\right)^{\frac{\gamma}{\gamma-1}} \tag{2.4}$$

Which is simply the isentropic flow relation (2.1) at $M = 1$. A larger difference between upstream and downstream pressure does not yield higher flow velocity at the throat. Nonetheless, upstream of the throat the air velocity is subsonic and downstream of the throat it is supersonic.

Choked flow thus occurs when the downstream pressure is below the critical pressure and it is therefore also referred to as supercritical flow — this is in contrast to the unchoked, subcritical flow. Using the (constant) specific heat ratio for air from Table 2.1, the critical pressure for choked flow is 54% of the total pressure.

The continuity of the flow dictates that the mass flow be constant, and thus a nozzle (or pod) geometry $A(x)$ can be related to the local Mach number using the mass flow equation at the throat and at an arbitrary other location x. Dividing the compressible mass flow equation (2.2) at an arbitrary location and at a choked throat (where $M = 1$) yields

$$\frac{A(x)}{A^\star} = \frac{1}{M}\sqrt{\left(\frac{2+(\gamma-1)M^2}{\gamma+1}\right)^{\frac{\gamma+1}{\gamma-1}}} \tag{2.5}$$

Thus, in the Q1D case, if the pod geometry and thus bypass area distribution $A(x)$ is known, the Mach distribution $M(x)$ can be found with Equation 2.5. Even if the nozzle is fully subsonic, a virtual sonic throat may be added to still obtain the Mach number distribution.

Now more realistically, although the pods themselves travel subsonically, the surrounding air may accelerate to supersonic flow. Transonic aircraft wings must be swept in order to prevent supersonic flow over the similarly accelerating flow. Unlike the external flow on transonic aircraft, the hyperloop pods are experiencing an internal flow, limited by the tube walls. The choking limit in the internal flow case is the *Kantrowitz limit.* (Kantrowitz and Donaldson [1945])

Substitution of the pod Mach number M_∞ into 2.5 yields an area ratio. If this ratio is larger than the actual tube area to throat area ratio (i.e. $A_{\text{bypass}} > A^\star$) then the nozzle is fully subsonic. On the other hand, if the ratio is smaller than the actual ratio (i.e. $A_{\text{bypass}} < A^\star$), then the actual throat is too small to attain the required mass flow. That is, the Kantrowitz limit has been exceeded.

The Kantrowitz limit can be exceeded as follows. Since the downstream pressure cannot drop below the critical pressure, the total pressure is increased instead. The pod (propulsive system) converts some of its work into compressing the air. The total pressure can subsequently be found.

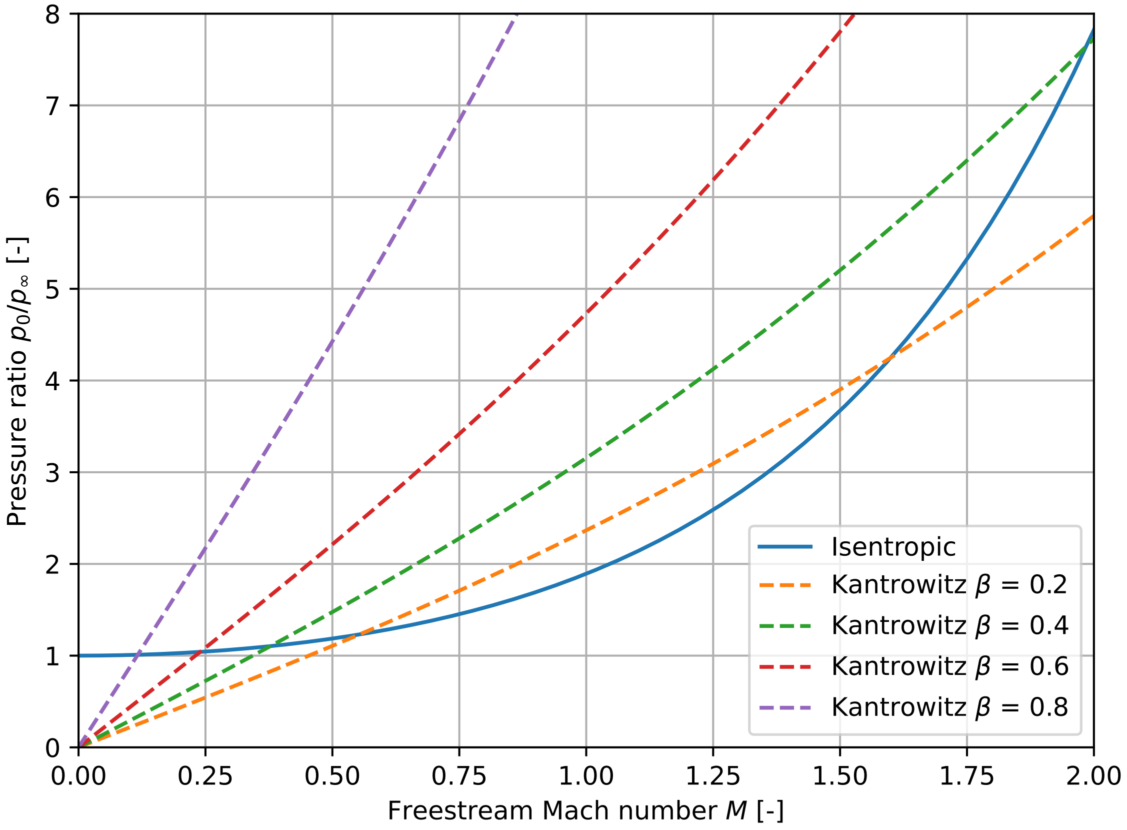

Figure 2.4: Pressure ratio of isentropic and Kantrowitz limited flow for varying blockage ratios.

Recall from Equation 2.2 that a choked flow can only increase the mass flow rate by increasing the total pressure or lowering the total temperature. The total temperature T_0 in the tube depends on the freestream Mach number M_∞ (i.e. the pod speed) and is found with the isentropic flow relation. The required mass flow rate $\dot{m}_{\text{req}}$ is in a tube with cross-sectional area A_t, using the equation of state

$$\dot{m}_{\text{req}} = \rho_\infty A_t U_\infty = \frac{p_\infty}{RT_\infty} A_t M_\infty \sqrt{\gamma R T_\infty} = \dot{m}^\star$$

The total pressure p_0 to achieve this required mass flow can be found by rearranging:

$$p_0 \overset{(2.3)}{=} \frac{A_t}{A^\star} p_\infty M_\infty \sqrt{\left(1 + \frac{\gamma - 1}{2} M_\infty^2\right) \left(\frac{\gamma + 1}{2}\right)^{\frac{\gamma+1}{\gamma-1}}}$$

If the Kantrowitz limit is exceeded, this total pressure is higher than the total pressure as calculated by the isentropic flow equations. Figure 2.4 shows the pressure ratio depending on the freestream Mach number for both isentropic flow and flow exceeding the Kantrowitz limit. The area ratio $(A_t/A^\star)$ is represented by the pod blockage ratio β,

$$\beta \equiv \frac{A_{\text{pod}}}{A_t} = 1 - \frac{A^\star}{A_t}$$

The pressure ratio is higher than the isentropic pressure ratio when the Kantrowitz limit is exceeded. For higher pod blockage, the Kantrowitz limit is exceeded at lower pod velocities. For instance, at 20% blockage, the total pressure increases when the pod travels at $M_\infty = 0.55$, whereas at 80% blockage the speed limit reduces to $M = 0.12$. It is interesting that at sufficiently high supersonic pod speeds, the Kantrowitz limit is not exceeded anymore, but this requires the pod to break the sonic barrier.

The drag increases linearly with the total pressure, because it is proportional to the dynamic pressure ($q \equiv \rho U^2/2$) and recall that for an ideal gas the density is proportional to the pressure. This discussion on the Kantrowitz limit thus quantifies one of the challenges of transonic pods travelling in low pressure tunnels.

Ideally the pods shall minimally block the air flow, but then the tunnel diameter must be large. The hyperloop project costs increase with tunnel diameter due to construction costs and stricter vacuum pump requirements. Therefore, some designs such as the one described by Musk [2013] propose to use an on-board compressor to prevent the total pressure increment. This, however, also increases the cost, risk and complexity of the design. This is why Opgenoord and Caplan [2018] opted to not implement a compressor in their design and accept the pressure (and drag) increment.

In summary, the pressure distribution $p(x)$ over the pod has to be computed in order to find the pressure drag. This distribution can be now found with the isentropic flow equation (2.1), which requires the total pressure p_0 and the Mach number distribution $M(x)$. The former may be higher than the tunnel pressure due to exceeding of the Kantrowitz limit. The latter is found with the nozzle geometry $A(x)$.

2.4 Basic drag analysis

The pod drag during normal operation can now be estimated using the nozzle equivalency principle. The drag is found by integrating all aerodynamic forces over the pod surface. The aerodynamic forces consist of (normal) pressure and shear stresses, leading to pressure drag D_p and skin friction drag D_s, respectively. Both are quantified in the next two sections.

2.4.1 Pressure drag

The discussion of the Kantrowitz limit in Section 2.3 explained how the pressure distribution can be found using isentropic flow. This is valid for a fully subsonic flow around the pod. However, the flow regime in the equivalent nozzle changes at transonic pod speeds as already indicated by the increase of total pressure due to exceeding the Kantrowitz limit. At increasing speeds the tail of the pod experiences partially to fully supersonic flow. The supersonic flow can jump back to subsonic flow due to a shock wave. The total pressure p_0, tube back pressure p and tube to throat area ratio $A/A^\star$ ultimately dictate the flow regime and where shock waves may form.

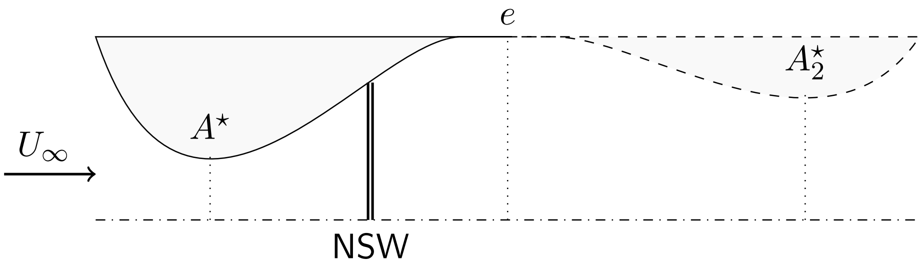

Figure 2.5: A nozzle with two throats and a normal shock wave (NSW).

The location of the shock wave on the pod can be determined by adding a virtual throat (or second pod) after the first one (Figure 2.5). The shock will lie between the throat and trailing edge (TE) of the pod. Its location can be found using the following steps.

First the trailing edge Mach number is found with the pressure and area ratio with respect to the virtual throat. Mass conservation between the trailing edge and real throat combined with adiabatic flow yields (see Appendix A.1)

$$M_{\mathsf{TE}} = \sqrt{\frac{\sqrt{1 + 2(\gamma - 1)\left(\frac{2}{\gamma+1}\right)^{\frac{\gamma+1}{\gamma-1}}\left(\frac{A^\star}{A_{\mathsf{TE}}}\frac{p_0}{p_{\mathsf{TE}}}\right)^2} - 1}{\gamma - 1}}$$

This Mach number yields the virtual isentropic area ratio (see Equation 2.5) and thus the area ratio with the real throat. Mass conservation between both throats in adiabatic flow yields

$$\frac{p_{0_2}}{p_{0_1}} = \frac{A_1^\star}{A_2^\star}$$

This total pressure ratio is then used to find the Mach number of the normal shock wave M_s with the implicit normal shock wave relation

$$\frac{p_{0_2}}{p_{0_1}} = \left[\frac{(\gamma+1)M_s^2}{(\gamma-1)M_s^2+2}\right]^{\frac{\gamma}{\gamma-1}}\left[\frac{\gamma+1}{2\gamma M_s^2 - (\gamma-1)}\right]^{\frac{1}{\gamma-1}}$$

Knowing the shock wave location allows to determine $p(x)$ over the full length of the pod (from leading to trailing edge). The total pressure drag on the pod is then

$$D_p = \iint_A p(x)\, dA$$

This concludes the discussion of the pressure drag. The second part of the drag originates from shear forces, i.e. the skin friction drag.

2.4.2 Skin friction drag

The skin friction drag is estimated with the flat plate formulas. The main distinction is made by the flow type: either laminar or turbulent air flow. The transition location may be approximated with the critical Reynolds number $\text{Re}^\star = 5 \times 10^5$ as follows (Incropera et al. [2006])

$$x^\star = \frac{\mu}{\rho U}\text{Re}^\star$$

Using the design parameters of Table 2.1, transition from laminar to turbulent flow occurs around $x = 25$ m. This means that before the transition location the Blasius solution for the friction coefficient c_f of a flat plate can be used, derived in e.g. Anderson [2011], i.e.

$$0 \leq x \leq x^\star : \qquad c_f = \frac{0.664}{\text{Re}_x} \qquad \text{(laminar)}$$

Whereas after the transition location, the Prandtl's 1/7 power law is applied, i.e.

$$x^\star \leq x \leq L : \qquad c_f = \frac{0.027}{\text{Re}_x^{1/7}} \qquad \text{(turbulent)}$$

The total skin friction drag is then

$$D_f = \iint_A c_f(x)\frac{\rho(x)U^2(x)}{2}\,dA$$

And the total drag is the sum of both pressure and skin friction drag.

A note on boundary layer and displacement thickness

It is common to divide the flow field around an object into two parts: an attached boundary layer where the viscous effect are significant and an outer inviscid region where viscous effect may be neglected. The boundary layer develops because of the no-slip condition: the velocity at the object's walls is zero. This creates a velocity gradient, which in turn leads to friction. The shear stress τ experienced at the walls is linearly proportional to the velocity gradient at the walls, mathematically

$$\tau = \mu\frac{\partial u}{\partial y}\bigg|_{y=0}$$

The boundary layer conventionally ends where the velocity has reached 99% of the freestream velocity. This is where the inviscid region starts. The boundary layer thickness δ for laminar flow over a flat plate can be described by the Blasius solution, again derived in Anderson [2011], i.e

$$0 \leq x \leq x^\star : \qquad \delta = \frac{5.0x}{\sqrt{\text{Re}_x}} \qquad \text{(laminar)}$$

This means that the boundary layer thickness increases with the square root of the length. The turbulent boundary layer thickness is

$$x^\star \leq x \leq L: \qquad \delta = \frac{0.37x}{\mathsf{Re}_x^{1/5}} \qquad \text{(turbulent)}$$

The displacement thickness $\delta^\star$ practically provides the thickness with which the walls should be increased to create a body with similar aerodynamic characteristics, but without a boundary layer. That is, adding the displacement thickness to the original body creates the shape which only experiences inviscid flow. For a flat plate, these are for the laminar and turbulent case, respectively

$$0 \leq x \leq x^\star: \qquad \delta^\star = \frac{1.72x}{\sqrt{\mathsf{Re}_x}} \qquad \text{(laminar)}$$

And

$$x^\star \leq x \leq L: \qquad \delta^\star = \frac{0.020x}{\mathsf{Re}_x^{1/7}} \qquad \text{(turbulent)}$$

Hence, the displacement thickness also increases over the length of the body. This means that the throat conditions of the pod occur at the end of the constant area mid section.

2.4.3 Results

The cross-sectional area of the pod model geometry in Figure 2.6 has been determined at several axial positions. Using the previously described methodology, the Mach number, static pressure and temperature distribution may be determined for varying pod speeds. The values are constant at the constant cross-section pod domain. Here, the blockage ratio is 0.71, which is the maximum value.

The Mach number distribution shows how the fully subsonic pod may accelerate to a partially supersonic flow regime at subsonic pod speeds (up to 210 m/s). At higher (but still subsonic) pod speeds, the trailing edge flow regime is fully supersonic up to $M = 2.5$.

The static pressure distribution shows that above the fully subsonic flow regime, the leading edge static pressure exceeds the 100 Pa tube pressure. The pressure reaches a fourfold of the static pressure at the leading edge at the highest analysed speed of 310 m/s. The fully supersonic regime drops below the ambient pressure at the trailing edge, whereas the partially supersonic regime returns to the tube pressure at the trailing edge.

The static temperature distribution shows the temperature increase due to exceeding the Kantrowitz limit up to 40 K at the leading edge at the top speed. The temperature drops due to increasing Mach number and returns to the ambient tube temperature if a shock wave occurs on the trailing edge. However, if the trailing edge is fully supersonic, the temperature drops further to 150 K or -123 °C.

Finally, the contributions of the pressure distribution and the skin friction to the total drag are shown. Clearly, the skin friction is negligible with respect to the pressure drag. At low speeds below the Kantrowitz limit, the drag barely increases. Beyond this limit, however, the drag rapidly increases. The drag at maximum speed is approximately 430 N. The power required to propel the pod to overcome the drag at maximum speed is then $P = DU$, yielding 134 kW.

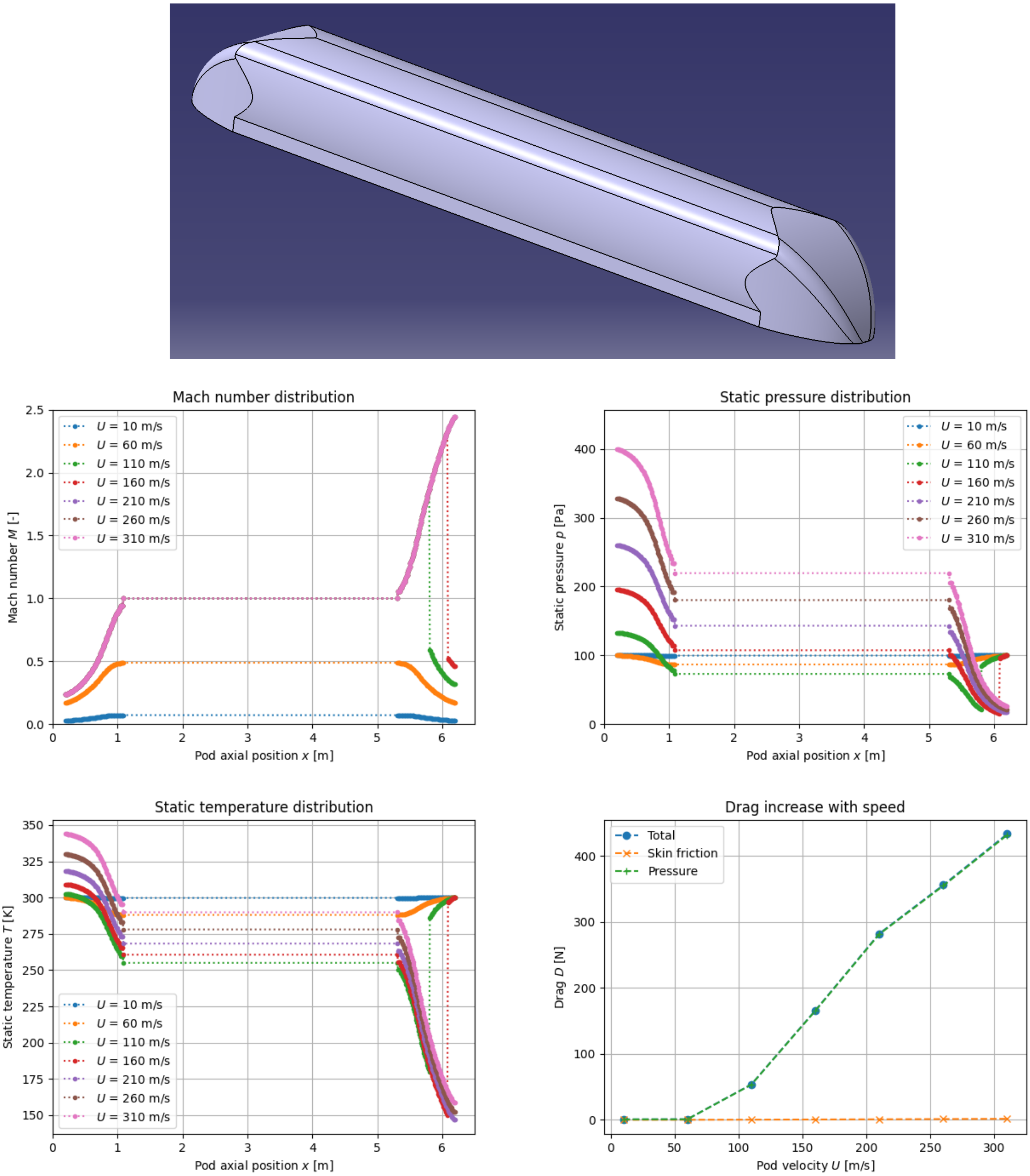

Figure 2.6: Drag analysis of the pod (above) yields the Mach number, static pressure and temperature distribution and the drag contributions at several pod speeds.

2.5 State-of-the-art: hyperloop literature study

Most hyperloop aerodynamic research focuses on the reduction of the pod drag varying its shape. Initially, the Hyperloop Pod Competition by SpaceX [2018] gave rise to several research papers. Opgenoord and Caplan [2018], for instance, note that the hyperloop pod flow regime is "unconventional", encountering relatively small Reynolds numbers at high Mach numbers. This is important because laminar to turbulent flow transition may be expected on the pod. Their drag reduction strategy was thus to move the transition location upstream in order to delay flow separation. The added skin friction due to a turbulent (but attached) flow on the one hand is smaller than the increased pressure drag due to separation on the other hand.

They also considered the Kantrowitz limit but argue that mitigation is unnecessary in their design: the freestream Mach number (at 110 m/s) is $M = 0.3$ at 30 percent blockage ratio. Figure 2.7 then shows that under these conditions the external flow accelerates to $M = 0.5$ at most, indicated by the red dot. The Kantrowitz limit is reached at the speed of sound ($M = 1$), indicated by the black solid line. Most full-scale hyperloop designs however advertise travel speeds near speed of sound, say, $M = 0.9$. This speed regime is far past the choking limit for any reasonable tube diameter (i.e. blockage ratio). Musk [2013] proposes to implement a compressor to bypass more air, whereas Opgenoord and Caplan [2018] realise this requires too much development effort due to the current lack of compressors designed for this flow regime. Another possibility is to accept the resulting higher pressure drag, but this may defeat the purpose of a near-vacuum environment. Figure 2.8 shows the rapid drag increase beyond the choking limit.

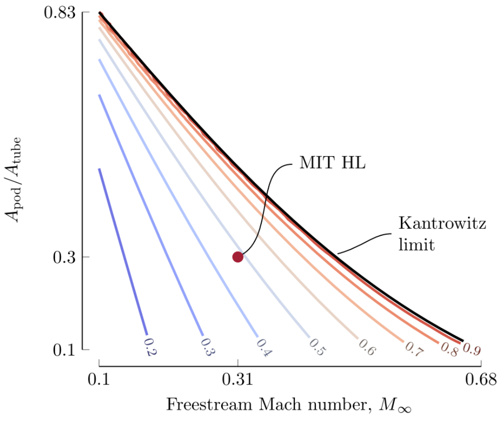

Figure 2.7: Blockage ratio versus freestream Mach number and resulting maximum Mach number due to the blockage. (From: Opgenoord and Caplan [2018])

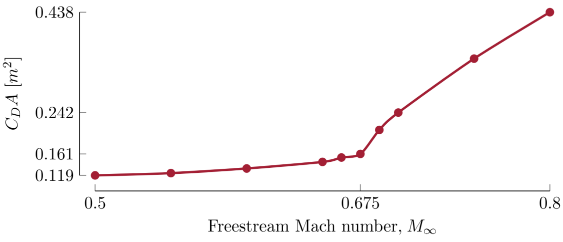

Figure 2.8: Rapid drag increase beyond the Kantrowitz limit. (From: Opgenoord and Caplan [2018])

Braun et al. [2017] took a similar approach in the same competition and agree with Opgenoord and Caplan [2018] that a compressor is obsolete for their design goal. Their approach focused on generating lift in addition to reducing drag. This design strategy should relieve the (maglev) levitating system requirements, whereas minimising drag only benefits the propulsive system. They do not justify *why* this relieve is required, even though one could argue that design for lift can create unnecessary instability issues. Drag fluctuations can be compensated by adaptive energy input by the propulsive system. The maglev system under this increased lift design only requires less effort at cruise speeds, just as the propulsive system. The peak energy requirement will thus remain at low speeds.

They estimate the one dimensional aerodynamic performance as follows. The pressure distribution on the pod is calculated from the local Mach numbers which are found from the *isentropic* mass conservation. Viscous effects from the laminar compressible boundary layer are computed solving the Karman momentum integral equation. This yields a (wall) friction coefficient and displacement thickness. Comparing with a two dimensional (2D) computational fluid dynamics (CFD) simulation, they conclude that the (1D) reduced model is accurate enough. Interestingly, unlike Opgenoord and Caplan [2018], they conclude neither flow separation nor transition to turbulent flow occurs on their pod design in tube pressures below 1 kPa.

A full-scale drag minimisation routine has been performed by Wong [2018] for a hyperloop company. His quasi one-dimensional isentropic nozzle solver conceptually follows the 1D method by Braun et al. [2017]. On average his model overestimated the pressure by approximately 10 percent, with the largest discrepancies at the nose of the pod, compared to his three dimensional CFD analysis.

Kim et al. [2011] claim that the three most sensitive parameters that dictate the total drag are blockage ratio, tube pressure and pod velocity. First, the blockage ratio dictates the “critical speed”, i.e. the Kantrowitz limit. Secondly, they show that the total drag is linearly proportional to the tube pressure and to the velocity squared, cf. $D = \frac{1}{2}\rho U^2 C_D A$.

Wong [2018], then, realised that those three parameters were already fixed by other requirements before his research initiated. Hence, he had to revert to optimising the shape of the pod, based on other maglev trains. He notes that the relatively thick boundary layer due to low Reynolds numbers decreases the bypass area. A sonic throat forms on the transition from constant cross-section to tail, where the displacement thickness is largest and thus the bypass minimal.

The aerodynamics research discussed above already shows a suitable methodology to analyse and design the hyperloop. Generally, a simple and quick one-dimensional problem analysis (see Section 2.4) allows to differentiate the relatively good designs from the bad ones. Furthermore, the design is reduced to a few parameters in order to reduce optimisation effort. The best designs are then fine-tuned and more thoroughly analysed with more advanced methods: usually CFD software is used. The hyperloop tube breach however has not been extensively analysed. This is the topic of the next chapter.

Chapter 3

Breach aerodynamics

The previous chapter aimed at the hyperloop pod aerodynamics during normal operation. The focus now shifts to the aerodynamics of a tube breach. Generally, fluids flow from high pressure to low pressure regions. Therefore, high pressure atmospheric air flows into the low pressure tube when its walls fail. The hyperloop tube breach can be characterised by two phenomena in chronological order: blast wave and underexpanded jet.

Figure 3.1 schematically shows the development of the shock and subsequent underexpanded jet inside a hyperloop tube. First on the left side the tunnel breaches. This initially leads to the formation of a bow shock, travelling supersonically through the tunnel in the middle subfigure. The blast wave flattens to two bidirectional normal shock waves, while a quasi-steady underexpanded jet forms at the hole, and impinges on the opposite tunnel wall. Note that the shocks have travelled further from the breach location after 1 s than shown (indicated by the break).

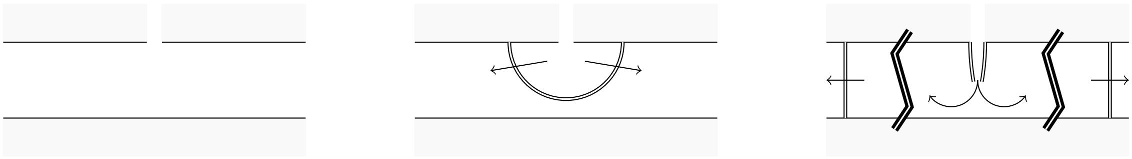

(a) $t = 0$

(b) $t \ll 1$ s

(c) $t > 1$ s

Figure 3.1: Introduction to the breach phenomenology: (a) tube breach, (b) bow shock formation, (c) impinging underexpanded jet (center) and normal shock wave (tube ends).

The hyperloop tube breach may be analysed as a short (convergent-divergent) nozzle emitting into a low pressure environment. Its length is then the tube thickness. The tube pressure is lower than the critical pressure using the outside atmospheric pressure in Equation 2.4. If the ambient pressure inside the tube is lower than the exit pressure of the nozzle, an underexpanded jet forms.

Figure 3.2 shows numerical schlieren images from a large eddy simulation (LES) of the development of an underexpanded jet due to a 6.5 total pressure ratio. Note that for the hyperloop the total pressure ratio is in the order of one thousand. Moreover, the jet will impinge on the opposite wall. The next section (3.1) explains the underexpanded jet in more detail.

Initially however, the discontinuity of the breach creates a bow shock. A more schematic representation of the bow shock is given by Radulescu and Law [2007] in Figure 3.3. The dissimilarity with the hyperloop tube for this phenomenon is that the depicted bow shock wave is unrestricted, whereas the tube walls confine the domain. This unsteady effect is analysed after the underexpanded jet, in Section 3.2. The bow shock that eventually becomes a normal shock is referred to as the blast wave because the rapid inflow of (kinetic) energy reminds of the shock waves due to explosions, i.e. rapid chemical energy release.

Hence, Section 3.1 reviews the underexpanded jet, which occurs due to the high pressure inflow into a low ambient pressure environment. Initially, however, a blast wave propagates through the tunnel, explained in Section 3.2. This chapter thus considers the following two sub-questions:

- *What are the typical aerodynamic phenomena expected during a tube breach?*
- *What models are useful to simulate those typical phenomena?*

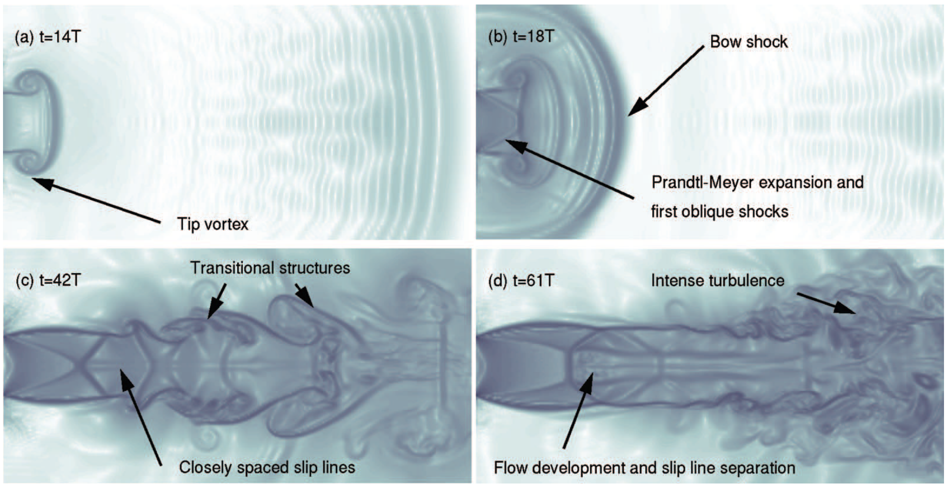

Figure 3.2: The initial stages of the developing underexpanded jet. (From: Vuorinen et al. [2013])

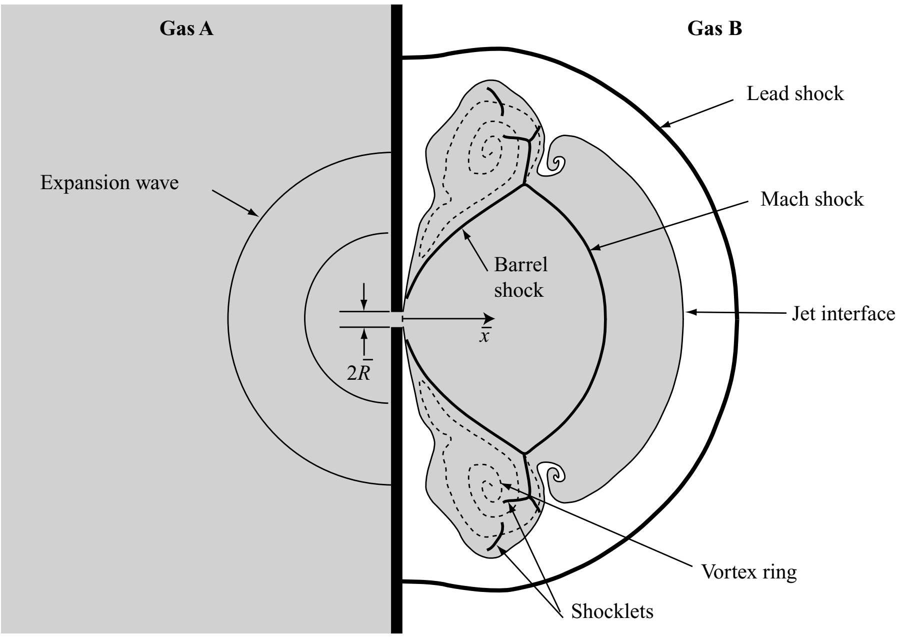
Gas A
Gas B
Lead shock
Expansion wave
Mach shock
Barrel shock
Jet interface
$\bar{x}$
$2\bar{R}$
Vortex ring
Shocklets

Figure 3.3: Schematic representation of the initial breach. (From: Radulescu and Law [2007])

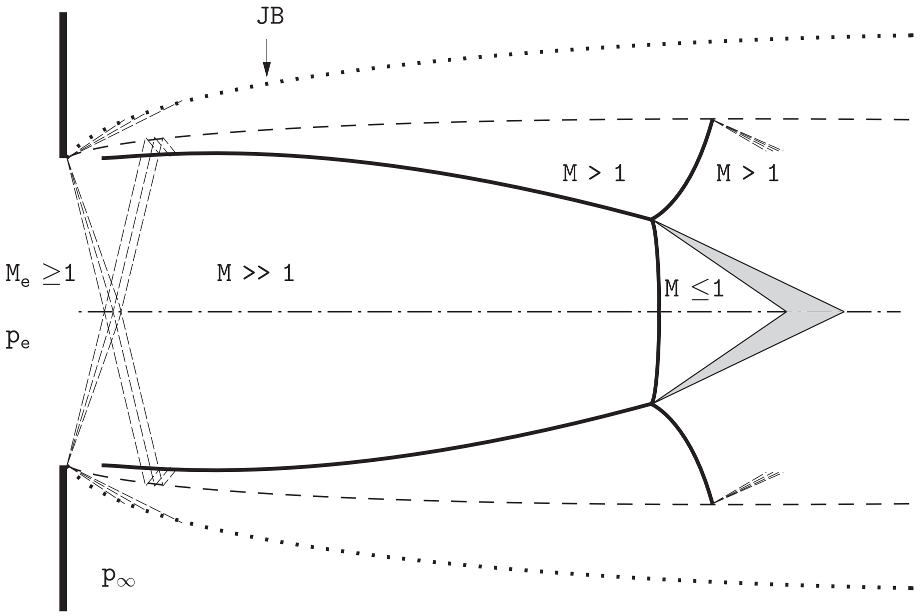

Figure 3.4: Highly underexpanded jet. (From: Franquet et al. [2015])

3.1 Steady underexpanded jet

An underexpanded jet develops when the ambient pressure downstream of a nozzle[1] (the back pressure) is lower than the pressure at the end of the nozzle. If the pressures are equal, isentropic expansion occurs. If the back pressure is higher than the nozzle exit pressure an overexpanded jet with oblique shock waves occurs.

The basis for the underexpanded jet theory — isentropic flow — was already discussed in the previous chapter. If a critical pressure difference is obtained, the mass flow is choked. The ratio of the pressures upstream and downstream of the nozzle, i.e. the nozzle pressure ratio, yields even more information about the flow regime.

First, Section 3.1.1 introduces the nomenclature of the underexpanded jet graphically supported by a typical sketch of this jet showing the details of the flow. Then, Section 3.1.2 quantifies the Mach disk location based on an empirical formula. Next, Section 3.1.3 discusses how the farfield may be modelled and Section 3.1.4 explains the effects of a non-circular hole on the underexpanded jet, supported by Schlieren images. Finally, the non-ideal behaviour of an orifice with respect to a regular nozzle is corrected by the discharge coefficient, which is introduced in Section 3.1.5.

3.1.1 Introduction

According to Franquet et al. [2015], extremely underexpanded jets occur where the total pressure is at least seven times the back pressure. The structure of the cross-section of this jet is schematically represented in Figure 3.4.

---

[1] In this introductory stage, the breach hole is considered an ideal nozzle. Section 3.1.5 describes how the discharge coefficient can compensate for this modelling inaccuracy.

Starting on the left where the flow originates, the exit pressure p_e and exit Mach number M_e are indicated. Prandtl-Meyer expansion fans (dashed) emanate from the lips (fat vertical lines) causing an expansion and acceleration of the downstream flow, increasing the Mach number. The expansion fans reflect off the dotted jet boundary (`JB`) and the dashed ambient pressure p_∞ streamline. The resulting compression waves converge and intersect, forming an oblique shock wave or intercepting shock, illustrated with a thick line. At a critical angle, where the intercepting shock reflects away from the central flow, a normal shock or Mach disk is formed. After the Mach disk the flow becomes subsonic. The reflection point where the intercepting shock coincides with the Mach disk, is referred to as the triple point. Note that the jet is axisymmetric about the (dash-dot) central axis, provided the hole is circular.

A slip stream emanates from the triple point separating the subsonic inner jet from the supersonic outer jet. At more moderate pressure ratios, the barrel structure may repeat. However, in the case of a loss of vacuum of the hyperloop tube, the initial total pressure ratio is approximately 1000. The Mach disk formed then has a diameter larger than the exit (hole) diameter and therefore cannot form a second barrel. (Chen et al. [2018])

3.1.2 Mach disc

The position of the Mach disk L_{MD} mainly depends on the pressure ratio, and this correlation is empirically found to be (Franquet et al. [2015])

$$\frac{L_{\text{MD}}}{D_e} = 0.65\sqrt{\frac{p_0}{p}} \tag{3.1}$$

Substitution of the breach pressure ratio suggests that the Mach disk initially arise at around 20 times the hole diameter D_e. In the current configuration, this means that initially the hole diameter has to be smaller than 50 mm such that a Mach disk can form before the flow hits the tunnel wall opposite the hole. However, as the pressure in the tube rises, the Mach disk retreats towards the puncture.[2]

3.1.3 Farfield zone

The following summarises the identification of the three main zones found in an underexpanded jet as categorised by Franquet et al. [2015]. The previous discussion focused on the effects relatively close to the breach, usually called the *nearfield zone*. This is usually split up into two parts: the core and the mixing layer. As what their names suggest, the core only consists of fluid particles originating from the jet, whereas the mixing layer also includes the ambient fluid — in the case of a breach, the tube air. Figure 3.2(d) shows how turbulence causes mixing of the jet and ambient (tube) air. The mixing layer completely replaces the core in the so-called *transition zone*, where both fluids mix better due to smaller differences in parameters such as pressure.

Eventually, the pressure homogenises to the ambient tube pressure in the fully developed *farfield zone*, so the jet is now perfectly expanded. Longitudinally, the temperature and velocity decrease inversely proportional to the distance from the breach location and radially, the velocity may be

---

[2] Note that in Figure 3.2(d) the Mach disk indeed follows Equation 3.1 for which $L/D = 1.66$.

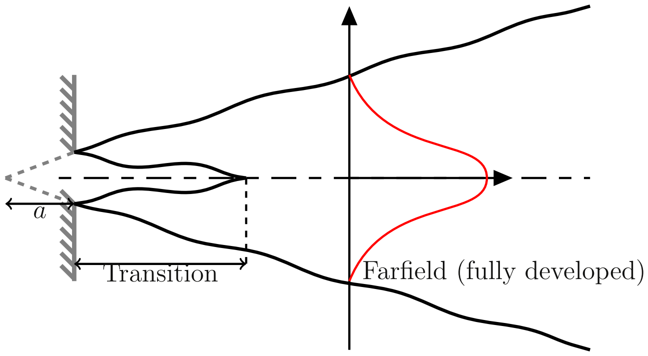

Figure 3.5: A notational nozzle may be used to omit computing the nearfield zone. (From: Franquet et al. [2015])

described by a Gaussian bell curve with the peak at the centre line of the jet, see Figure 3.5. The main benefit in the analysis of the farfield zone is its "little memory of its recent past" (Franquet et al. [2015]). One could therefore replace the original nozzle with a hypothetical equivalent nozzle, the *notational nozzle*, and realise the same resulting flow. The pseudo-source in Figure 3.5 different from the original breach point may then be used to omit the computation of the nearfield zone.

Nevertheless, the farfield zone is less interesting for a tube breach because the farfield may be interacting with the wall opposite of the breach hole.

3.1.4 Effect of nozzle geometry

The previous discussions focused on a circular nozzle exit. Unless a hole is purposefully manufactured in the hyperloop tube, a breach will most likely not be perfectly circular. It is nonetheless the easiest case to analyse.

Rajakuperan and Ramaswamy [1998] performed several experiments on oval nozzles of varying aspect and pressure ratios, see Figure This showed that low aspect ratio oval exits (e.g. 1.4 in the experiment) still acted similar to circular exits. For larger aspect ratios, the minor axis plane showed no shock barrel structure (but an oblique shock instead) and a much higher jet spreading rate with respect to the major axis. The minor axis plane jet was also more affected by the pressure ratio. Moreover, the cross-sectional area of the jet was larger for the asymmetrical jet than for an axisymmetrical jet, so more mixing occurred. The cross-sectional shape evolution of the asymmetrical jet goes from the exit oval shape to a circle to a larger oval where major and minor axis switched.

Li et al. [2017] analysed the flow characteristics of circular, elliptic, square and rectangular nozzles at 5.60 pressure ratio using LES. They conclude that the "key flow features" are similar for a circular and square nozzle. Also, the ellipse and rectangle show similar results along their minor and major axes.

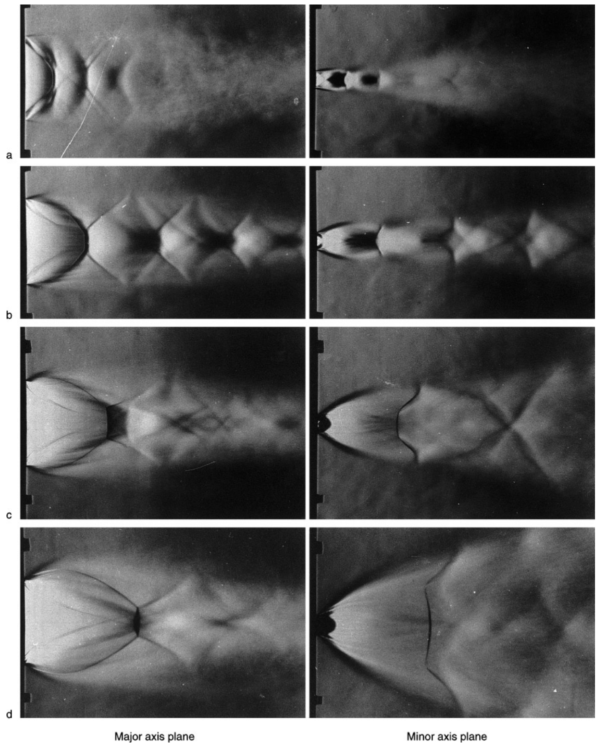
a
b
c
d
Major axis plane
Minor axis plane

Figure 3.6: Schlieren images of free jets from a nozzle with 5.0 aspect ratio at pressure ratios **a.** 2.9; **b.** 5.2; **c.** 10.3; **d.** 20.3. (From: Rajakuperan and Ramaswamy [1998])

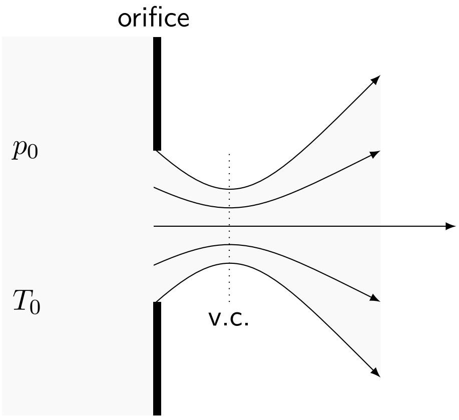
orifice
p_0
T_0
v.c.

Figure 3.7: Exaggerated view of a vena contracta (v.c.) after an orifice.

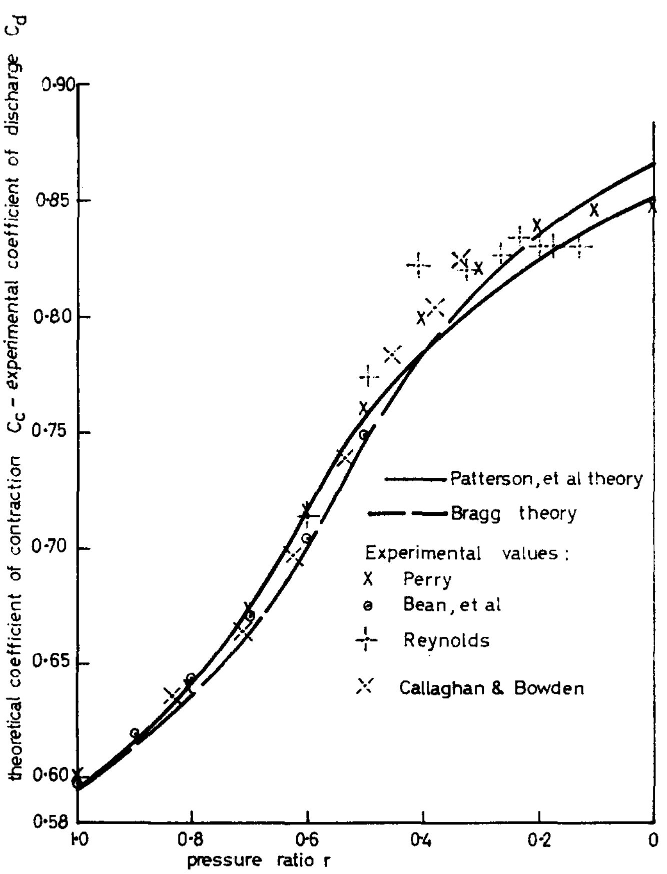

Figure 3.8: The coefficient of contraction for axisymmetric orifices depends on the pressure ratio. (From: Patterson et al. [1970])

3.1.5 Discharge coefficient

Up to this point the breach hole was assumed to act as an ideal nozzle, whereas real orifice flows usually demonstrate a vena contracta effect (Figure 3.7).

The isentropic mass flow equation (2.2) often yields a higher value than the actual obtained mass flow rate, mainly due to the effect of friction ϕ and contraction κ of the air after the hole. (Jitschin et al. [1999]) For a thin orifice and high Reynolds number flow, where the boundary layers remain relatively thin, the friction is negligible: $\phi \approx 1$. The contraction, however, can play a significant role and is often referred to as the *vena contracta*, sketched in Figure 3.7. The contraction coefficient is

$$\kappa = \frac{A_{\text{v.c.}}}{A_{\text{hole}}}$$

For axisymmetrical orifices κ can be found using one-dimensional (1D) theory, see e.g. Figure 3.8 from Patterson et al. [1970]. It can be seen that the contraction ratio for the initial breach is $\kappa = 0.85$, whereas near the equilibrium state it decreases to $\kappa = 0.6$.[3] The ratio of the actual flow and the ideal, isentropic flow is the discharge coefficient C_d, which includes the friction and contraction effects:

---

[3] Note that the pressure ratio in Figure 3.8 is the vena contracta pressure divided by the total pressure. This is different from the total pressure ratio in Equation 2.1.

$$C_d = \phi\kappa = \frac{\dot{m}_{\text{real}}}{\dot{m}_{\text{ideal}}} = \frac{\dot{m}_{\text{3D}}}{\dot{m}_{\text{1D}}}$$

By definition, then, the discharge coefficient of an ideal nozzle is 1. The discharge coefficient thus acts as an efficiency factor. Generally, determining the discharge coefficient a priori is not trivial as it may depend on many parameters. Three works are discussed next to outline a methodology.

By means of a dimensional analysis with the Buckingham π theorem, Binder et al. [2015] suggest seven dimensionless quantities affect the discharge coefficient for circular orifices of which they investigate three. They exclude the Reynolds number because Deckker and Chang [1965] have experimentally shown independence for Re $> 10^4$. Moreover, the influence of the Mach number is excluded, because it highly depends on the pressure ratio (see e.g. the isentropic flow equations). Keeping the temperature ratio constant during the experiments, they investigate and provide correlations for the effect of pressure ratio, length-to-diameter ratio and chamfer-to-diameter ratio. Since adding chamfer increases the similarity with a nozzle, the discharge coefficient increases. Their focus however lies on the application to turbomachinery, whereas the discharge coefficient near the choking point is the main interest of the present thesis.

Ward-Smith [1979] studied the influence of the axial length on C_d for choked circular orifices without chamfer. When the orifice thickness is 1 to 7 diameters, the critical discharge coefficient remains constant. For higher length-to-diameter ratios, the boundary layer increases friction, the flow becomes Fanno choked and the discharge coefficient decreases. For smaller ratios, the discharge ratio increases.

Finally, Linfield [2000] provides an engineering algorithm to find the discharge coefficient based on cubic splines. It is capable to take into account the effects of pressure ratio, wall angle, area ratio, specific heat ratio and edge rounding for axisymmetrical and planar flow.

Figure 3.9 compares the contraction coefficient of Patterson et al. [1970] with the discharge coefficient of Linfield [2000] for air through a sharp edged axisymmetrical orifice dependent on the pressure ratio. Note that the supersonic flow regime starts at the critical pressure ratio according to Equation 2.4, i.e. $z^\star = 0.53$. For extremely underexpanded jets it is thus to be expected that the discharge coefficient is 0.85, approximately.

More specifically, Figure 3.9 uses two piecewise cubic splines for the discharge coefficient: one for the subsonic case above the critical pressure ratio and one for the supersonic case below the critical pressure ratio. The cubic splines require the value of both the discharge coefficient and the partial derivative of the discharge coefficient with respect to the pressure ratio z at both end points, marked with green dots.

For completeness, the used (least squares fit) equations by Linfield [2000] are repeated here for a $\pi/2$ rad wall angle α and air specific heat ratio 1.4 in order of incompressible ($z = 1$), critical ($z = z^\star$) and upper choked flow limit ($z = 0$).

$$C_d\big|_{z=1} = \frac{1}{1+\frac{2}{\pi}} = 0.61 \tag{3.2a}$$

$$\left.\frac{\partial C_d}{\partial z}\right|_{z=1} = -\frac{C_d|_{z=1}\left(1 - C_d|_{z=1}\right)}{\gamma} = -0.17 \tag{3.2b}$$

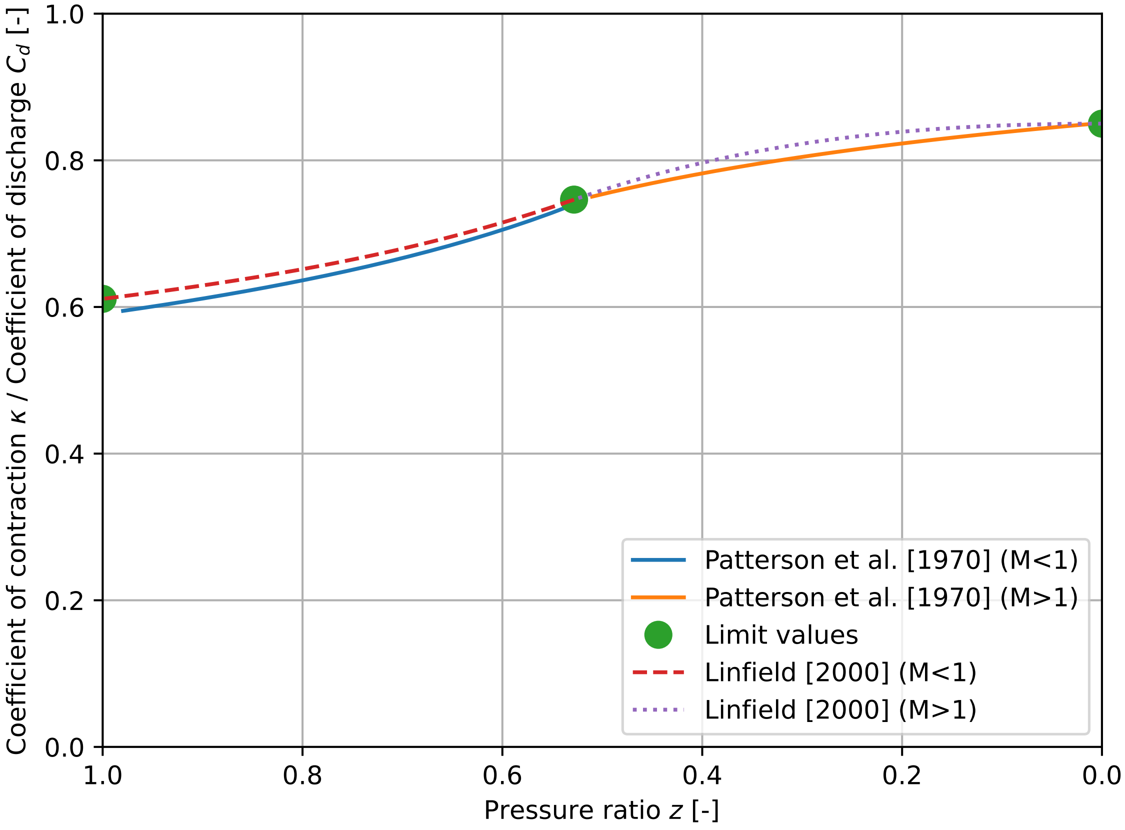

Figure 3.9: Comparison of methods to derive the discharge coefficient dependence on pressure ratio for a sharp-edged axisymmetrical orifice.

$$A_1 = 1 - 0.5103\left(\frac{\alpha}{\pi}\right) + 0.05644\left(\frac{\alpha}{\pi}\right)^2 + 0.1360\left(\frac{\alpha}{\pi}\right)^3 = 0.77$$

$$B_1 = -0.07373\left(\frac{\alpha}{\pi}\right) + 0.07731\left(\frac{\alpha}{\pi}\right)^2 - 0.02848\left(\frac{\alpha}{\pi}\right)^3 = -0.021$$

$$C_d\big|_{z=z^\star} = A_1 + B_1\gamma = 0.75 \tag{3.3a}$$

$$A_2 = 0.1549 - 0.01177\gamma = 0.138$$

$$B_2 = 0.934 + 0.6433\gamma = 1.83$$

$$\left.\frac{\partial C_d}{\partial z}\right|_{z=z^\star} = \frac{\frac{\alpha}{\pi}}{A_2 + B_2\frac{\alpha}{\pi}} = 0.47 \tag{3.3b}$$

$$A_3 = 1 - 0.2702\left(\frac{\alpha}{\pi}\right) + 0.1322\left(\frac{\alpha}{\pi}\right)^2 = 0.90$$

$$B_3 = 0.0488\left(\frac{\alpha}{\pi}\right) - 0.06124\left(\frac{\alpha}{\pi}\right)^2 + 0.04805\left(\frac{\alpha}{\pi}\right)^3 = -0.015$$

$$C_d\big|_{z=0} = A_3 + B_3\gamma = 0.85 \tag{3.4a}$$

$$\left.\frac{\partial C_d}{\partial z}\right|_{z=0} = 0 \tag{3.4b}$$

And the equations used by Patterson et al. [1970] for the subsonic and supersonic regime, respectively, are following, where $I = 0.095$, $I_I = 0.0293$, $I_{II} = 0.0127$

$$\kappa = \begin{cases} \dfrac{(\gamma-1)(1-z)}{z^{1/\gamma}-z}\left((I+0.5) - \dfrac{I_I(z-1)}{\gamma} - \dfrac{2\gamma-1}{3\gamma^2}I_{II}(z-1)^2\right) & \text{for } z > z^\star \\ \\ \dfrac{1}{(\gamma+1)z^\star - z}\left((z-1) + 2(z^\star-1)I - \dfrac{2}{\gamma}I_I(z^\star-1)^2 - \dfrac{2}{3\gamma}I_{II}(z-1)^3\right) & \text{for } z < z^\star \end{cases} \tag{3.5}$$

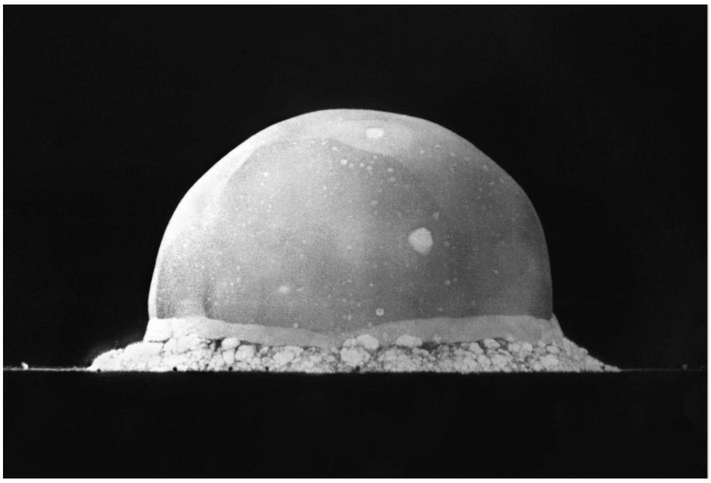

Figure 3.10: Blast wave by nuclear explosion. (Photo by: Berlyn Brixner [1945])

3.2 Unsteady blast wave

Whereas the previous discussion mainly pertains to the *steady* flow characteristics locally near the breach hole, the following discussion emphasises the *unsteady* effects throughout the tube. It was seen in Figure 3.2 that a bow shock emanates from the breach hole and initiates the (extremely) underexpanded jet due to the sudden breach. It turns out that this bow shock eventually travels as a normal shock wave bidirectionally through the complete hyperloop tube until complete dissipation.

Shock waves are usually analysed with the Euler equations, the set of partial differential equations which describes inviscid flow. They are introduced in Section 3.2.1, formulated in three dimensions in Section 3.2.2 and in quasi-one-dimensional form in Section 3.2.3, from which the Rankine-Hugoniot equations are derived in Section 3.2.4.

Blast waves are shock waves due to a sudden local eruption of energy. If this energy impulse is released at the boundary of a semi-infinite domain (i.e. an open field), the blast wave strongly resembles the bow shock wave of Figure 3.2. For instance, compare the figure with the blast wave due to the trinity nuclear detonation test in Figure 3.10. Two methods of analysing blast waves are proposed and compared: the analytical strong shock (Section 3.2.5) and the empirical TNT shock relations (Section 3.2.6).

3.2.1 Euler equations

The governing formulas as derived in e.g. White [2006], Anderson [2011] are the conservation of mass, the conservation of momentum and the conservation of energy. Unsteady, inviscid, compressible flow is described by the Euler equations, the inviscid formulation of the viscous Navier–Stokes equations. For a three-dimensional problem this yields five quasi-linear hyperbolic partial differential equations for six unknowns: three components of the velocity, density, pressure and energy. The system of equations is closed with equations of state.

This system is solved in the domain bounded by boundary conditions and over a time bounded by initial conditions. A physical boundary condition for inviscid flow is the flow tangency condition at the walls. This states that the velocity normal to the wall is zero. In practice, the walls become streamlines and no mass flow is allowed through the wall. In contrast, for viscous flows the stricter no-slip condition is applied, imposing zero velocity at the wall. Note that these boundary conditions dictate the solution at the boundary and are thus Dirichlet (first-type) boundary conditions. For unsteady flows an initial condition is required, for instance an initially stagnant gas $\mathbf{u}(t_0) = \mathbf{0}$ throughout the domain.

The three-dimensional (3D) and quasi-one-dimensional (Q1D) formulation of the Euler equations without body forces and heat transfer are presented in the next two sections.

3.2.2 Three dimensional formulation

The conservative formulation of the Euler equations consists of the conservation of mass:

$$\frac{\partial \rho}{\partial t} + \nabla \cdot (\rho \mathbf{u}) = 0 \tag{3.6a}$$

The conservation of momentum:

$$\frac{\partial (\rho \mathbf{u})}{\partial t} + \mathbf{u} \cdot \nabla (\rho \mathbf{u}) + \nabla p = 0 \tag{3.6b}$$

And the conservation of energy:

$$\frac{\partial (\rho E)}{\partial t} + \nabla \cdot (\mathbf{u}(\rho E + p)) = 0 \tag{3.6c}$$

Here, the dependent variables are density ρ, pressure p, velocity vector $\mathbf{u} = (u, v, w)^T$ and specific total energy $E = e + |\mathbf{u}|^2/2$. They are functions of two independent variables: position $\mathbf{x} = (x, y, z)^T$ and time t. Note that the conservation of momentum consists of three equations and excludes body forces such as gravity and electromagnetism, besides the viscous surface forces. No general closed-form solutions have been found (yet) for the Euler equations and they are difficult to solve analytically. Therefore, usually the system of equations is solved numerically with computational fluid dynamics (CFD) software. This is done in Chapter 5.

3.2.3 Quasi-one-dimensional formulation

A less ambitious and computationally cheaper option is found in 1D analysis. In order to still capture the effect of area changes, a Q1D approach is used. That is, $A'(x) \neq 0$. Moreover, using the isentropic flow assumption, the energy equation can be replaced by constant entropy along a particle path. Then, the governing equations for unsteady Q1D flow without friction, mass addition and heat transfer are mass continuity:

$$\rho_t + u\rho_x + \rho u_x + \rho u \frac{A'(x)}{A(x)} = 0 \tag{3.7a}$$

Conservation of momentum:

$$u_t + uu_x + \frac{1}{\rho}p_x = 0 \tag{3.7b}$$

And entropy conservation:

$$p_t + up_x - a^2\left(\rho_t + u\rho_x\right) = 0 \tag{3.7c}$$

Where use has been made of the fact that $ds \propto dp - a^2 d\rho$ and for a perfect gas the speed of sound a is

$$a^2 = \left(\frac{\partial p}{\partial \rho}\right)_S = \frac{\gamma p}{\rho}$$

With the method of characteristics (MOC) the partial differential equations can be reduced to a simpler system of ordinary differential equations. The Riemann invariants are along the characteristics

$$dp_\pm \pm \rho a du_\pm + \rho a^2 u \frac{A'(x)}{A(x)} dt_\pm \quad = 0 \quad \text{on} \quad \mathcal{C}_\pm \equiv \left(\frac{dx}{dt}\right)_\pm = u \pm a \tag{3.8}$$

$$dp_0 - a^2 d\rho \quad = 0 \quad \text{on} \quad \mathcal{C}_0 \equiv \left(\frac{dx}{dt}\right)_0 = u \tag{3.9}$$

One note of caution on using the MOC on the previously discussed overexpanded jet: this is troublesome for the extremely high pressure ratio of the hyperloop breach. The difference in the Prandtl-Meyer function at the equally extreme Mach numbers is too small and evaluations quickly lead to a diverging solution.

Another powerful method is the self-similar analysis employed by Taylor–von Neumann–Sedov (TvNS) on the spherically symmetrical strong shock wave. The solution is given in Section 3.2.5, but first the more general Rankine-Hugoniot equations for shock waves are presented in the next section.

3.2.4 Rankine-Hugoniot equations

The Rankine-Hugoniot relations can be derived from the 1D Euler equations (3.7) and describe the discontinuous change of flow variables across a normal shock wave:

$$[\rho v] = 0$$

$$[p + \rho v^2] = 0$$

$$\left[\rho v\left(h + \frac{1}{2}v^2\right)\right] = 0$$

Where the difference between the pre-shock state 1 and post-shock state 2 is indicated with square brackets, for instance $[x] = x_2 - x_1$. The specific enthalpy h is defined as $h \equiv e + p/\rho$. The velocity v is relative to the shock. These jump equations can be rewritten to the following practical normal shock wave relations only dependent on pre-shock Mach number M_1 and specific heat ratio γ. The pressure ratio:

$$z \equiv \frac{p_2}{p_1} = 1 + \frac{2\gamma}{\gamma+1}\left(M_1^2 - 1\right) \tag{3.10a}$$

Density ratio:

$$\frac{\rho_2}{\rho_1} = \frac{(\gamma+1)\,M_1^2}{2+(\gamma-1)\,M_1^2} \tag{3.10b}$$

And post-shock Mach number

$$\mu^2 \equiv M_2^2 = \frac{(\gamma-1)M^2+2}{2\gamma M^2-(\gamma-1)} \tag{3.10c}$$

Similar equations for oblique shock waves are derived in standard compressible gas books such as by Anderson [2011]. Oblique shock waves have an additional flow velocity component tangent to the shock, which is not present in normal shocks. The θ-β-M relation for the deflection angle θ and the oblique shock angle β is repeated here:

$$\tan\theta = 2\cot\beta\frac{M^2\sin^2\beta-1}{M^2(\gamma+\cos 2\beta)+2} \tag{3.11}$$

The prior equations have been recorded because are required in the following discussions, the 3D and 1D inviscid Euler equations, and shock waves are regularly mentioned.

3.2.5 Analytical strong shock

The initial stages of a breach strongly resemble those of an explosion at ground level: in both cases a hemispherical bow shock emanates from the initial breach or explosion location due to the rapid energy release. In the case of a breach, this is the sudden influx of kinetic and pressure energy; in the case of most explosions, this is the rapid conversion of chemical energy into heat due to an exothermic reaction. Figure 3.10 allows for a qualitative comparison with the shock wave from the trinity nuclear explosion. Shock waves formed due to a sudden burst of energy in a small volume are referred to as blast waves.

Taylor [1950], von Neumann [1947], and Sedov [1946] independently derived with a self-similar analysis the solution for a strong shock due to an energy release E_0. The shock radius R as a function of time t is

$$R = \beta\left(\frac{E_0 t^2}{\rho_0}\right)^{1/5} \tag{3.12a}$$

Where ρ_0 the ambient air density and constant $\beta = 1.033$ for air with $\gamma = 1.4$. The shock velocity u_s is then found by differentiating with respect to time:

$$u_s = \dot{R} = \frac{2R}{5t} \tag{3.12b}$$

Finally, the shock overpressure ζ is related to the shock velocity using the normal shock wave relation

$$\zeta \equiv \frac{\Delta p}{p_0} \overset{\text{(3.10a)}}{=} \frac{2\gamma}{\gamma+1}\left(\frac{u_s^2}{a^2}-1\right) \tag{3.12c}$$

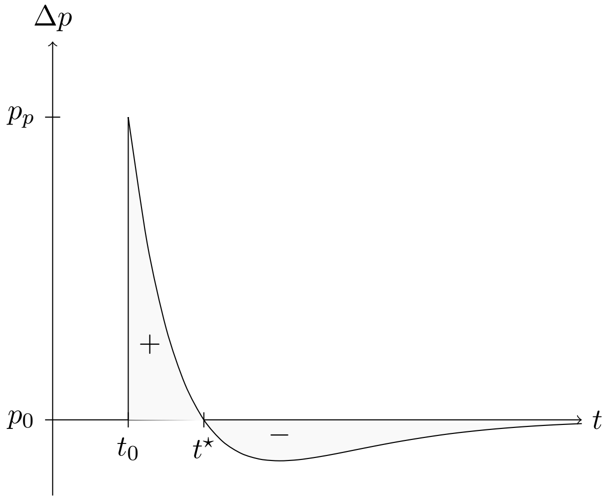

Figure 3.11: Friedlander curve showing the overpressure due to a blast wave.

A typical blast wave overpressure development at a fixed location is displayed in Figure 3.11. The pressures are given with respect to the ambient pressure p_0, i.e. they are gauge pressures. The further away from the explosion origin the pressure is experienced, the longer it takes before the positive phase starts at arrival time t_0 and the smaller the peak overpressure p_p becomes. Due to the shock wave, the pressure almost instantly rises to the peak overpressure and decreases next. The decrease results in a negative pressure with respect to the ambient pressure at critical time $t^\star$, but it has an absolute value lower than the overpressure. Finally, the pressure returns to the initial ambient pressure.

The area underneath the pressure curve during the positive phase yields the impulse caused by the blast wave. A larger area due to a larger peak overpressure or longer positive phase thus leads to higher damages. The curve is described by the Friedlander equation (Friedlander [1946])

$$p(t) = p_0 + p_p \left(1 - \frac{t}{t^\star}\right) \mathcal{H}\left(t - t_0\right) \exp\left(-\beta \frac{t}{t^\star}\right)$$

The Heaviside step function $\mathcal{H}$ is used to initialise the function.

Note that the previous discussion pertains to an idealised blast wave decay into a semi-infinite isotropic free field. For a hyperloop tube breach, the confinement of the wave adds complexity to the preliminary analysis given above. Unlike the sudden release of explosive energy, the breach blast wave is continuously sourced with additional kinetic energy until the tube pressure equals the outside pressure or the hole has been closed. The Friedlander curve may not be completely appropriate in this scenario, because after the peak overpressure, the static pressure remains high.

Moreover, depending on the pressure ratio, the strong shock assumption may not be valid. Resorting to empirical shock relations for smaller explosions may then be an option. They are presented and compared with the strong shock equations in the next section.

3.2.6 Empirical TNT shock relations

Empirical models based on experimental results have been proposed for the blast wave overpressure due to an explosion. Cube root scaling laws are popular, where the shock radius has been non-dimensionalised with the cube root of the energy released divided by preshock pressure p_{t_0}.

For instance, Brode [1959] uses $Z_B \equiv R/\alpha$ where $\alpha^3 \equiv E_0/p_{t_0}$, in which Z_B is indeed dimensionless. Alternatively, the Hopkinson-Cranz scaling law defines a reduced distance Z with released energy in terms of equivalent TNT mass W in kg. The yield energy ε of trinitrotoluene, $C_6H_2CH_3(NO_2)_3$ (TNT) is approximately 4 MJ/kg, and $E_0 = W\varepsilon$. The reduced distance in m/$\sqrt[3]{\text{kg}}$ is then

$$Z \equiv R/\sqrt[3]{W}$$

Note that the preshock pressure is excluded using this scaling method, most likely because the explosive tests are usually performed around standard atmospheric conditions.

Karlos et al. [2016] give an overview and comparison of frequently used empirical models. Three models are presented for discussion. First, Henrych [1979] suggests

$$\zeta_{\mathsf{H}}(Z) = \begin{cases} \dfrac{14.072}{Z} + \dfrac{5.540}{Z^2} - \dfrac{0.357}{Z^3} + \dfrac{0.00625}{Z^4} & \text{for } 0.05 \leq Z \leq 0.3 \\[2ex] \dfrac{6.194}{Z} - \dfrac{0.326}{Z^2} + \dfrac{2.132}{Z^3} & \text{for } 0.3 \leq Z \leq 1 \\[2ex] \dfrac{0.662}{Z} + \dfrac{4.05}{Z^2} + \dfrac{3.288}{Z^3} & \text{for } 1 \leq Z \leq 10 \end{cases} \tag{3.13a}$$

Whereas Kinney and Graham [2013] suggest

$$\zeta_{\mathsf{KG}}(Z) = \frac{808\left[1+\left(\dfrac{Z}{4.5}\right)^2\right]}{\sqrt{\left[1+\left(\dfrac{Z}{0.048}\right)^2\right]\left[1+\left(\dfrac{Z}{0.32}\right)^2\right]\left[1+\left(\dfrac{Z}{1.35}\right)^2\right]}} \tag{3.13b}$$

And the strong shock limit of TvNS yields after some algebraic manipulation

$$\zeta_{\mathsf{TvNS}}(Z) \overset{(3.12)}{=} \frac{2\gamma}{\gamma+1}\left(\frac{4\beta^5\varepsilon_{\mathsf{TNT}}}{25\gamma p_0 Z^3} - 1\right) \tag{3.13c}$$

Where the overpressure is defined as $\zeta \equiv \Delta p/p_0$. The three overpressure decay relations are compared in Figure 3.12. Note the limited application range of the Henrych model (3.13a). The strong shock limit $Z \to 0$ yields a finite overpressure ($\zeta_{\mathsf{KG}} \to 808$) in the Kinney–Graham model (3.13b). Both empirical relations are similar. The self-similar analytical solution for the strong shock overpressure (3.13c) rises indefinitely towards the strong shock limit with slope 3 on a log-log plot, but this method breaks down for weak shocks. In fact, sound wave overpressure decays inversely proportional to the distance from the source. The empirical and analytical approaches overlap around $Z = 1$.

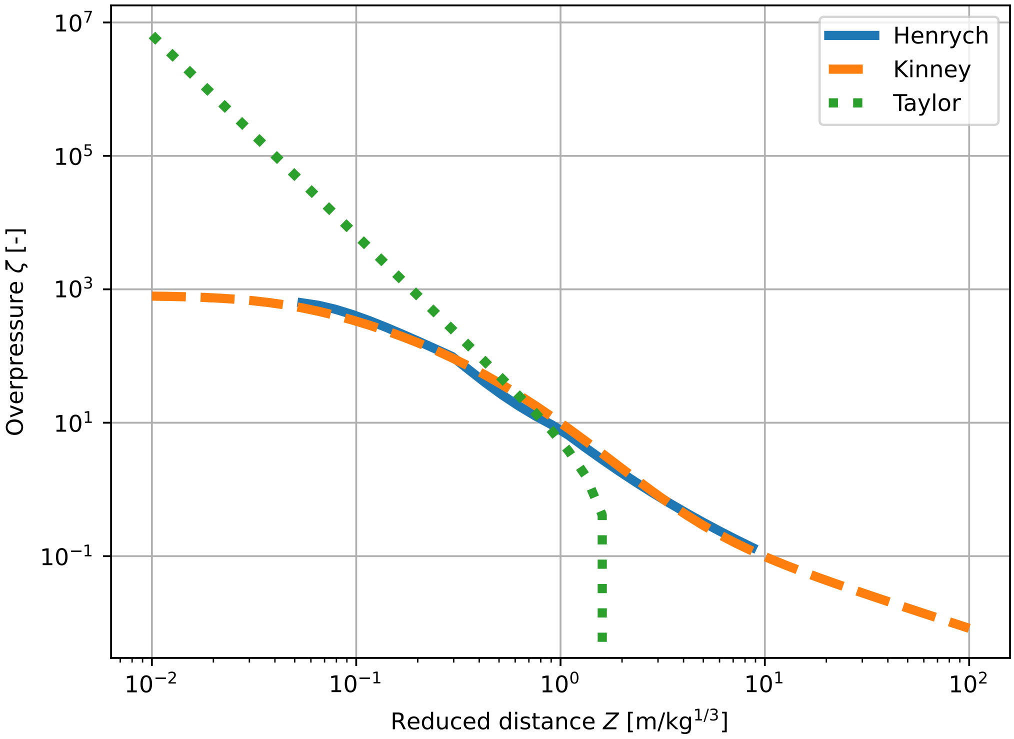

Figure 3.12: Comparison of free field decay laws.

The TNT equivalence principle allows to extend the experimental results for other explosives. The yield energy of the distinct explosive is compared to that of TNT. This allows to substitute any sudden release of energy, such as the kinetic energy released due to a loss of vacuum. A caveat is that its straightforward application is due to possibly invalid assumptions. A few final remarks on the model limits are therefore appropriate.

Only under specific conditions the equivalency yields correct results. Thus, simply extending the empirical data for TNT explosions to kinetic energy release due to a breach may lead to large errors. Note that Equations 3.13a and 3.13b are based upon experiments of explosions under approximately standard atmospheric conditions. Extrapolating this data to a partial vacuum may then be troublesome. Assimilating the preshock pressure into the reduced distance may assist in comparing both cases. Equation 3.13c is able to take into account the ambient pressure p_0 and is derived from the unsteady Euler equations for a spherically symmetric strong shock.

3.3 State-of-the-art: loss of vacuum accident

A flow field similar to a hyperloop tube breach is encountered in the analysis of a so-called loss of vacuum accident (LOVA) in a fusion reactor. Confinement of particles is required in order to achieve a fusion reaction. This can be done in a toroidal chamber with magnetic coils, a tokamak. The chamber is kept at low pressure to reduce impurities and enhance the fusion reaction. Coincidentally, the LOVA is usually analysed at a pressure level similar to that inside the hyperloop tube. Rossi et al. [2019] state that the major risk of the LOVA is resuspension of "toxic, explosive and radioactive" dust particles off the walls. They are a by-product of the plasma reaction and shall stay inside the vacuum chamber.

This is why LOVA research generally revolves about two research topics. First, the pressurisation time has to be determined. Once the torus reaches the external ambient pressure, dust may exit through the breach location. Second, the wall friction velocity, which is one of the main mobilisers of the dust particles, has to be determined. Clearly, both parameters are dependent on the scale of the LOVA. Thus, many numerical and experimental studies vary for instance the hole size and location, and pressure and temperature ratio. A few research papers are summarised and discussed next.

One of the first papers investigating a LOVA is due to Gay et al. [1998]. They use a lumped model to investigate the air leakage into the vacuum vessel for three hole sizes. The total pressure inside the 3700 m^3 vessel rises to the ambient pressure of 1 bar. The time it takes to repressurise the vessel clearly depends on the hole size, e.g. the vessel is repressurised from 0.9 bar in 20 s by a 0.3 m^2 hole, but in 5 s by a 1 m^2 hole. In the former scenario the mass flow is 45 kg/s. Air inside the vessel is heated by the 100 °C surroundings and expands, causing an outflow of 1.4 kg/s maximum. Even though the hyperloop is usually in thermal equilibrium with the surroundings, these specific results can readily be used to verify hyperloop breach models.

An example analysis closer to the pressure ratio of the hyperloop is also given: the vessel is pressurised from 0 to 1 bar. A 0.02 m^2 hole yields a constant 5 kg/s mass flow until after 350 s, when it decreases to 0 kg/s after 700 s. Also, a 0.005 m^2 hole yields a constant 1.2 kg/s mass flow until after 1450 s, decreasing to 0 kg/s after 3200 s. These values agree with the isentropic mass flow equation (2.2) in Section 2.3.

Lupelli et al. [2014] compared three common Reynolds-averaged Navier–Stokes (RANS) turbulence models — Zero-Equation (ZE), k-ω, and Shear Stress Transport (SST) — and grid resolutions with experimental results in the Stardust facility, a cylindrical vacuum chamber. The ZE model yielded acceptable results with air velocity errors smaller than 20% for all grid resolutions. The k-ω model performed worse. The SST model performed best, but at the cost of more computational effort (approximately five times longer than ZE). Another benchmark parameter provided the reason why Lupelli et al. [2014] prefer the SST model. The LOVA causes a highly underexpanded jet with a Mach disk which location can be estimated with an empirical analytic relation (as discussed in Section 3.1). Again the SST model yielded the smallest error (5%).

Xu et al. [2018] present their methodology to obtain results for a wide range of scenarios. First they vary the number of cells to determine convergence of the solution. Next they compare three turbulence models on their accuracy. In the end they chose the SST-model, also convinced by Lupelli et al. [2014]. With this fixed setup they analyse the flow at different pressures and temperatures. Further, they report maximum velocities of 700 m/s, which exceeds the speed of

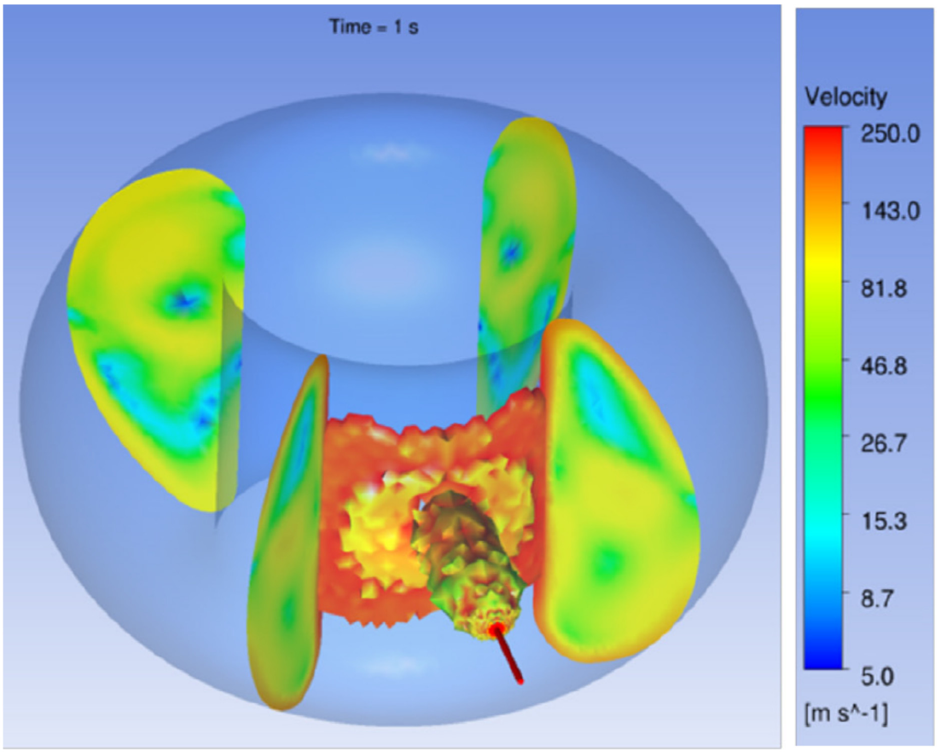

Figure 3.13: Flow velocity fields in the torus and air jet contour 1 s after initial inflow. (From: Gélain et al. [2015])

sound. Oddly, however, they do not mention any investigation on shock waves. In another report Xu et al. [2019] varies the hole area from 0.02 to 0.5 m^2.

Gélain et al. [2015] modelled the air inflow from the 1 bar atmosphere into the 150 Pa torus. Figure 3.13 shows a result of their CFD analysis. A few insights are worth mentioning. First, air enters the low-pressure torus through an underexpanded jet. This jet impinges on the surface opposite the entrance hole, spreading over the inner wall comparable to a water jet splashing from the faucet into a sink. The maximum velocity one second after the breach is 250 m/s. This contradicts the aforementioned Iresults by Xu et al. [2018], but better reflects a choked flow.

The previous papers analysed the breach numerically. An example of an experimental analysis is discussed by Rossi et al. [2019]. Unsatisfied with the initial lack of agreement with results in the Stardust facility, they use the Buckingham Pi theory to relate the scaled experimental results with the numerical full-scale results.

Chapter 4

Quasi 1D model

This chapter treats the next research sub-question: *What is the overpressure magnitude throughout the tube caused by a given breach scenario?* The discussed quasi-one-dimensional (Q1D) models can be used to analyse the transient blast wave confined by the cylindrical tunnel. First, a one-dimensional (1D) shock tube is analysed as a Riemann problem in Section 4.1. Section 4.2 discusses the development of the shock geometry. Section 4.3 uses an energy based approach, similar to the analysis of a blast wave due to an explosion. Section 4.4 describes an alternative planar approach which expands the 1D shock tube analysis. Section 4.5 then compares both methods.

4.1 Riemann shock tube

A tube in which a diaphragm separates two initially stagnant gases at different pressures can be described by a Riemann problem. A snapshot of a post-rupture state of the tube is seen in Figure 4.1. Zone 1 on the left side represents the unperturbed high pressure ambient (outside) atmosphere, and zone 4 on the right side describes the unperturbed conditions in the low pressure (inside) hyperloop tube.

Now instantaneously removing the diaphragm simulates the 1D breach: (Poisson, P) expansion waves travel outwards to the ambient atmosphere and (Hugoniot, H) pressure waves travel into

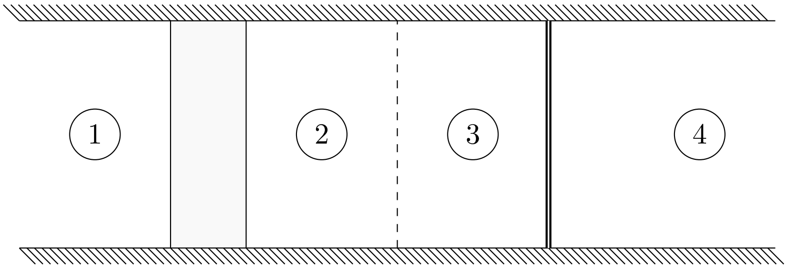

Figure 4.1: Geometry of a Riemann shock tube problem.

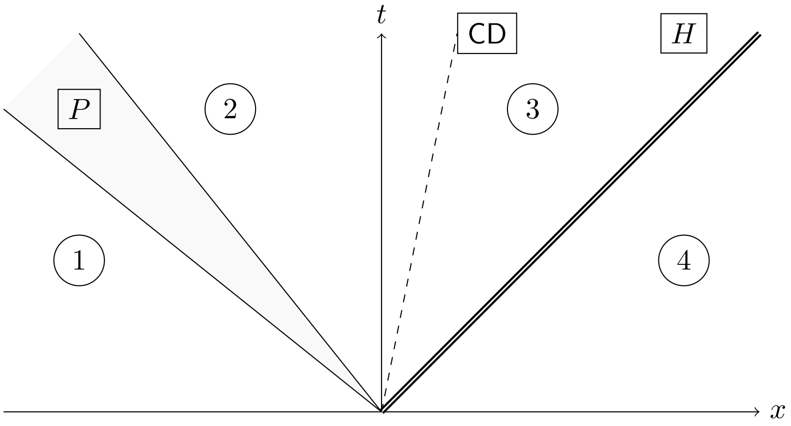

Figure 4.2: The (x,t)-diagram showing the developing expansion wave and shock wave.

the tube. Both waves separate the tube into two additional zones (2 and 3) separated by a contact discontinuity (CD). Density, specific internal energy and specific entropy jump over this discontinuity, whereas the pressure and velocity on both zones remain equal, i.e. $p_2 = p_3$ and $u_2 = u_3$.

This model uses the following assumptions:

- The diaphragm at $x = 0$ is instantaneously removed at $t = 0$.
- Zones 2 and 3 do not mix; no mass flow occurs between the zones.
- No boundary layer formation; fully inviscid except at the shock.
- No three-dimensional (3D) effects.
- Ideal gas and constant specific heat ratio γ.

The shock wave equations (3.10) can be rewritten to find for the shock wave (see e.g. Anderson [2003])

$$u_3 = \frac{a_4}{\gamma_4}\left(\frac{p_3}{p_4} - 1\right)\sqrt{\frac{\frac{2\gamma_4}{\gamma_4+1}}{\frac{p_3}{p_4} + \frac{\gamma_4 - 1}{\gamma_4 + 1}}}$$

And the expansion fan with the method of characteristics (MOC) and isentropic flow equations yields

$$u_2 = \frac{2a_1}{\gamma_1 - 1}\left[1 - \left(\frac{p_2}{p_1}\right)^{(\gamma_1 - 1)/2\gamma_1}\right]$$

The (implicit) shock tube equation then follows from $\gamma_1 = \gamma_4 = \gamma$, $p_2 = p_3$ and $u_2 = u_3$

Table 4.1: Breach initial conditions. Compare with Table 2.1

Parameter	Symbol	Value	Unit
Atmospheric (external) pressure	p_1	101325	Pa
Tube (internal) pressure	p_4	100	Pa
Temperature outside and inside the tube	T_1 T_4	15	deg C
Speed of sound outside and inside	a_1 a_4	340	m/s
Initial air speed outside and inside	u_1 u_4	0	m/s
Air specific heat ratio	γ	1.4	-

$$\frac{p_1}{p_4} = \frac{p_2}{p_4}\left[1 - \frac{(\gamma-1)(p_2/p_4-1)(a_1/a_4)}{\sqrt{(2\gamma)[2\gamma+(\gamma+1)(p_2/p_4-1)]}}\right]^{\frac{-2\gamma}{\gamma-1}} \tag{4.1}$$

Solving numerically for the presupposed design conditions in Table 4.1 yields $p_2 = p_3 =$ 1144 Pa and $u_2 = u_3 =$ 805 m/s. Compare these results with the ambient conditions inside the tube: the overpressure is an order of magnitude higher and the compressive blast wave travels at more than twice the speed of sound!

This shock tube analysis thus provides a straightforward solution for a full-rupture case, where the hyperloop tube cross-section is discontinuously exposed. Hence, this is irrespective of the scale of the breach. A Q1D model can take the hole size into consideration, but requires an understanding of the shock geometry as described in the next section.

4.2 Shock geometry

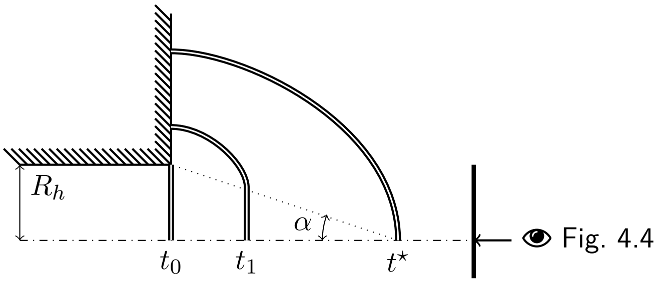

Figure 4.3: Critical shock definition.

The blast wave due to the vacuum breach is not immediately spherical. Figure 4.3 shows a shock travelling rightwards through a hole with radius R_h. This idealised shock front develops from initially planar at t_0 to an intermediate form (in part planar, in part curved) at t_1, to a full (critical) bow shock at $t^\star$. The shock remains planar in its core, until the critical shock is formed. Skews [1967] geometrically showed that for this case

$$\tan^2\alpha = \frac{(\gamma-1)(M^2-1)\left(M^2+\frac{2}{\gamma-1}\right)}{(\gamma+1)M^4}$$

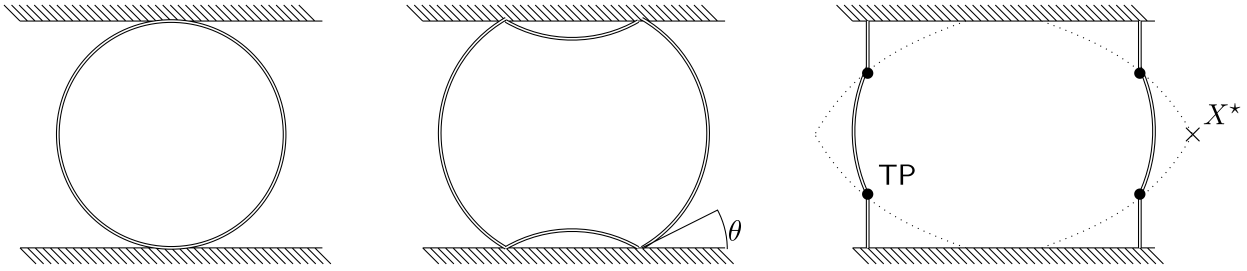

(a) $\theta = 0$ (b) $\theta < \beta_{\text{max}}$ (c) $\theta > \beta_{\text{max}}$

Figure 4.4: Spatiotemporal development of a confined spherical blast wave. Illustration of the wall reflections according to the blast wave incident angle θ: (a) incident wave, (b) regular reflection, and (c) Mach reflection.

It is to be expected that the shock wave pressure jump decays as the shock frontal area increases. Sloan and Nettleton [1975] measured that the shock wave overpressure indeed did not decay along the longitudinal axis of the hole, until the critical shock position

$$R^\star \equiv R(t^\star) = \frac{R_h}{\tan\alpha}$$

Unlike the semi-infinite domain of a hemispherical blast wave due to a ground explosive in an open field (recall Figure 3.10), the critical hyperloop breach shock is constrained by the tube walls. Now consider the projection of Figure 4.3 from the right into the hole.

Figure 4.4 shows how in a tunnel an initially spherical blast wave one-dimensionalises into a normal shock wave due to a Mach reflection: the oblique shock at the wall becomes a normal shock once the angle between the wall and the shock θ becomes larger than the maximum deflection angle β_{max}. This angle can be laboriously determined using the θ-β-M relation of oblique shock waves (3.11), but Kinney and Graham [2013] provide a more straightforward approximate hyperbolic equation to find the limiting angle in degrees

$$\beta_{\text{max}} \approx \frac{1.75}{M-1} + 39 \tag{4.2}$$

The triple point (TP) — similarly defined as for the underexpanded jet in Section 3.1 — travels along the dashed line in Figure 4.4 until point $X^\star$, where the shock becomes fully planar.

Silvestrini et al. [2009] proposed a straightforward method to take into account the confining effects of the wall geometry. They summarise the confinement effects in an energy concentration factor (ECF). For the case of a hyperloop, the free hemispherical propagation of the explosion is confined by the 1D tunnel. The ECF n is then the ratio of both volumes V

$$n = \frac{V_{\text{3D}}}{V_{\text{1D}}} = \frac{4R^2}{3D^2}$$

Recall that the blast radius is R and the tunnel diameter is D. The new reduced distance for a 1D blast wave is

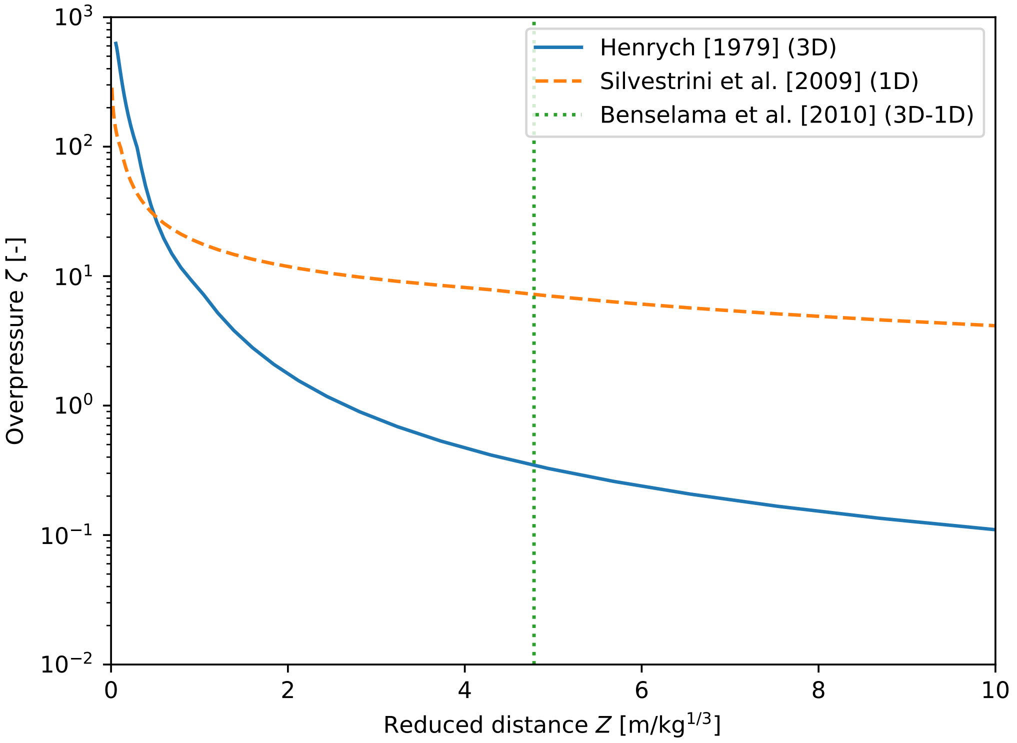

Figure 4.5: Free-field and 1D overpressure decay for 1 kg TNT in a 1 m^2 tunnel. Left of the transition (dotted green) the 3D decay applies (solid blue); right of the transition the 1D energy concentration factor has to be taken into accout (dashed orange). (From: Benselama et al. [2010])

$$Z_{\mathrm{1D}} = \frac{Z_{\mathrm{3D}}}{\sqrt[3]{n}} = \frac{R}{\sqrt[3]{nW}} = \sqrt[3]{\frac{3RD^2}{4W}}$$

Figure 4.5 shows the overpressure decay over the reduced distance in a 1 m^2 tunnel cross-sectional area for both the free-field law (3.13a) and 1D ECF corrected law. In the near field ($Z \to 0$) the free-field laws apply, whereas in the far-field ($Z \to \infty$) the ECF has to be applied.

The transition (reduced) location from the initially 3D blast to a 1D normal shock wave due to the confinement of a tunnel can be found with the correlation proposed by Benselama et al. [2010]. It estimates the transition region based on the initial blast radius relative to the tunnel radius α, which was validated experimentally. Their proposed correlation is

$$Z_{\mathrm{3D}\to\mathrm{1D}} = \frac{0.0509}{\alpha^{13/9}} \tag{4.3}$$

This transition region is indicated in Figure 4.5 by the red dotted line for a 1 kg TNT blast load in the 1 m^2 tunnel. The decay of the blast wave then first follows the solid blue line, then at $Z_{\mathrm{3D}\to\mathrm{1D}}$ jumps to the dashed green line and follows this line to $Z \to \infty$. Once more the trouble with this correlation model is that the empirical data probably only works for experiments at standard atmospheric conditions and not for vacuum tunnels.

4.3 Volumetric energy method

A Q1D framework can be set-up with the empirical blast wave models of Section 3.2.6. The driving source of those explosive blast waves is due to the sudden release of chemical (or nuclear) energy. In the breach case, the release is in the form of kinetic and pressure energy. The kinetic energy inflow can be found similar to the compressible mass flow equation with the ideal gas law and isentropic relations[1]

$$\dot{E}_{\text{kin}} = \frac{1}{2}\dot{m}U^2 = \frac{p_0 A M^3}{2}\sqrt{\gamma^3 R T_0 \left(1+\frac{\gamma-1}{\gamma}M^2\right)^{-\frac{\gamma+1}{\gamma-1}}} = \frac{p_0 A}{2}\sqrt{\gamma^3 R T_0 \left(\frac{2}{\gamma+1}\right)^{\frac{\gamma+1}{\gamma-1}}}$$

This is the ideally choked kinetic energy inflow which has to be corrected with the discharge coefficient, as discussed in Section 3.1.5. One could either multiply the energy inflow with the $C_d = 0.85$ value for high pressure ratios, or use the uncorrected energy inflow $C_d = 1$ as a conservative estimate. The breach hole remains choked as long as the pressure inside the tube is lower than the critical pressure (Equation 2.4). Also note that the kinetic energy increases with hole area A.

The kinetic energy is found by integrating with respect to time, from breach up to the time of critical shock $t^\star$ when the overpressure decay starts:

$$E_{\text{kin}} = \int_{t_0}^{t^\star} \dot{E}_{\text{kin}} dt = \frac{R^\star \dot{E}_{\text{kin}}}{u_3}$$

The pressure (internal) energy must be determined as well. The energy required to compress the hemispherical critical shock volume $V^\star$ from the tube pressure p_4 to the preshock pressure p_3 is found from the equation of state for a perfect gas (Brode [1959])

$$E_{\text{pres}} = \frac{(p_3 - p_4)V^\star}{\gamma - 1}$$

Now, the reduced distance is independent of the hole size. In fact, it is solely dependent on the temperature, pressure and fluid medium (air) inside and outside the tube. Explicitly,

$$Z^\star = \frac{R}{\sqrt[3]{W_{\text{TNT}}}} = \frac{R^\star}{\sqrt[3]{\frac{E_{\text{kin}}+E_{\text{pres}}}{\varepsilon_{\text{TNT}}}\frac{p_0}{p_4}}} = \left[\frac{\pi}{\varepsilon_{\text{TNT}}}\frac{p_0}{p_4}\left(\frac{C_d p_0}{2u_3\tan\alpha}\sqrt{\gamma^3 R T_0\left(\frac{2}{\gamma+1}\right)^{\frac{\gamma+1}{\gamma-1}}} + \frac{2(p_3-p_4)}{3(\gamma-1)\tan^3\alpha}\right)\right]^{-1/3}$$

The design conditions in Table 2.1 yield a conservative reduced distance of 0.59 m/$\sqrt[3]{\text{kg}}$ TNT at 1 atm.[2] This yields an initial overpressure of between 20 and 31 over the critical shock wave, depending on the relation used (3.13):

---

[1] Note that the total conditions of the high pressure region denoted with subscript 0 are equal to the unperturbed zone (denoted with subscript) 1.

[2] Applying the 85% correction factor for the vena contracta at high pressure ratios as determined in Section 3.1.5 would yield a reduced distance of 0.61 m/$\sqrt[3]{\text{kg}}$ TNT at 1 atm.

$$\zeta_H(Z^\star) = 20 \qquad \zeta_{KG}(Z^\star) = 29 \qquad \zeta_{KG}(Z^\star) = 31$$

The shock overpressure is larger than the 1D result, but this is its value at the critical shock wave location. The overpressure decays as the shock wave increases its area. The shock wave decay due to area increase is quantified in the next section.

4.4 Planar method

Whereas the previous model was based on the empirical models of explosions of Section 3.2.6, the Chester–Chisnell–Whitham (CCW) model is a Q1D model based on the Euler equations (Section 3.2.3). The CCW method (Section 4.4.1) yields a relation between the Mach number and the area: $M(A)$. It is also referred to as geometric shock dynamics (GSD) (Section 4.4.2), when this method is generalised from Q1D to 3D.

4.4.1 CCW model

The contributions of each of the three authors of the CCW model is as follows. Chester [1954] first analysed an asymptotic solution for a shock in a tunnel with small area increment. Because a large change is due to many small area increments, Chisnell [1957] integrated the asymptotic solution (in a different formulation) such that $Af(z)$ remains constant. Whitham [1958] then found a similar result with the MOC, but he related the area to the Mach number instead of pressure ratio, i.e. the $A - M$ relation.

The Chisnell function displayed in Figure 4.6 monotonically increases with pressure ratio. More explicitly,

$$f(z) = \frac{z^{1/\gamma}(z-1)}{\sqrt{z + \frac{\gamma-1}{\gamma+1}}} \left[\frac{1+\Gamma}{1-\Gamma}\right]^{\sqrt{\gamma/2(\gamma-1)}} \left[\frac{\Gamma - \sqrt{\frac{\gamma-1}{2\gamma}}}{\Gamma + \sqrt{\frac{\gamma-1}{2\gamma}}}\right] \exp\left[\sqrt{\frac{2}{\gamma-1}} \tan^{-1}\left\{\frac{2}{\gamma-1}\sqrt{\frac{\gamma z}{z + \frac{\gamma+1}{\gamma-1}}}\right\}\right] \tag{4.4}$$

Where

$$\Gamma \equiv \frac{1}{\sqrt{1 + \frac{\gamma+1}{(\gamma-1)z}}}$$

This model can be used to extend the 1D shock tube model and offers an alternative approach to the previously discussed empirical TNT shock equivalence method. Its procedure is as follows. First, the initial pressure ratio is determined with the shock tube equation (4.1). Next, the initial shock area (i.e. the critical shock hemispherical surface area) is dictated by the hole size. The final shock area is twice the tunnel area, cf. Figure 4.4. The final overpressure depending on the hole size is shown in Figure 4.7 for the tunnel diameter of 1 m.

The overpressure decay can be determined if the initial bow shock is approximated by a hemisphere once the critical shock has formed. The shock area is then $A = 2\pi R^2$ for $R^\star < R < R_t$. The shock overpressure does not decay once the final tube radius R_t has been achieved, although realistically the shock overpressure will eventually decay due to viscous effects. One way to introduce the decay is by employing the ECF to the expanding free field decay, instead of using the final overpressure beyond R_t.

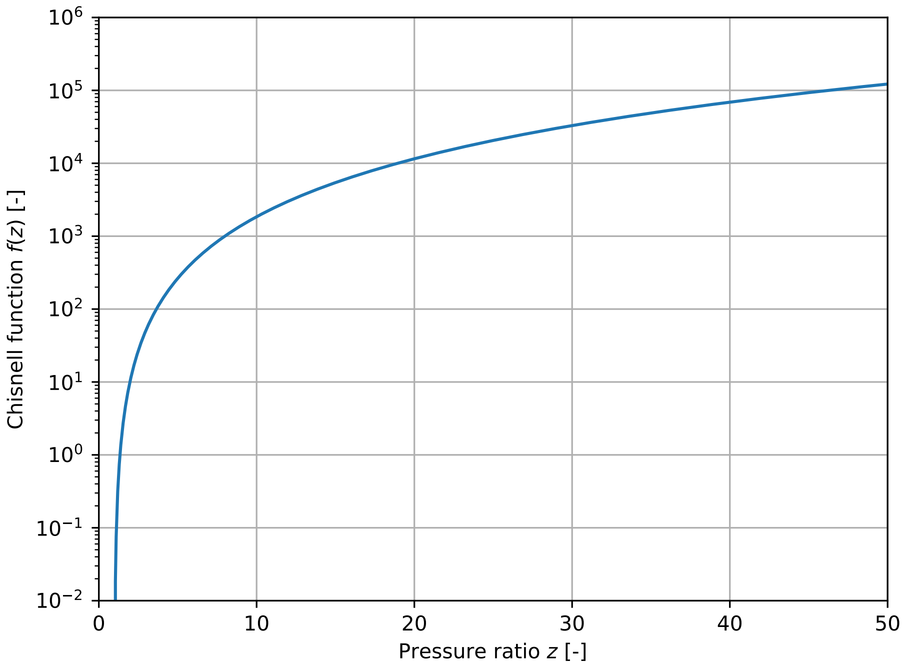

Figure 4.6: Chisnell function evaluated for pressure ratios larger than unity.

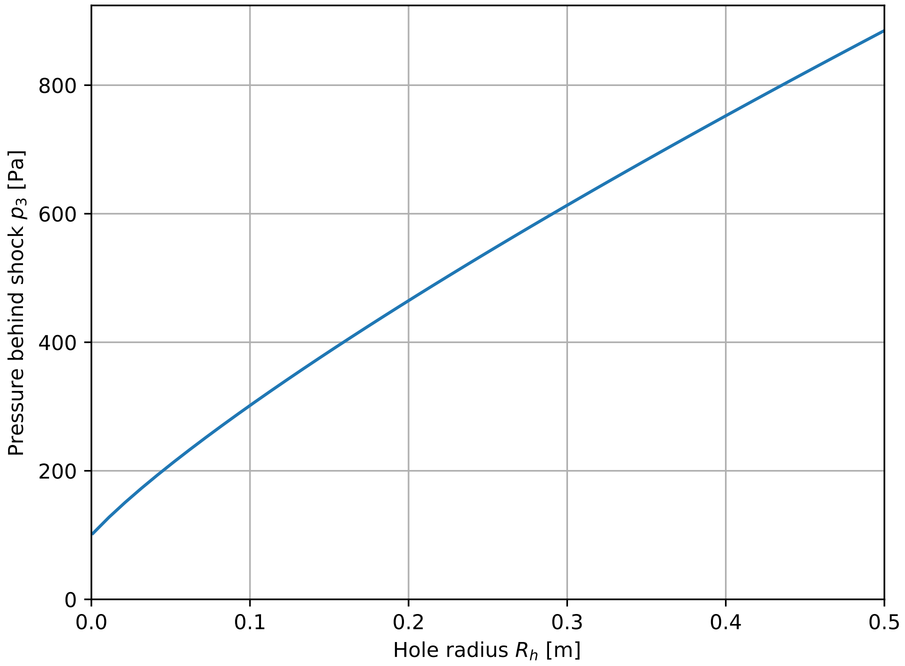

Figure 4.7: Final shock pressure for a 1 m diameter tunnel depending on the hole size.

4.4.2 GSD model

The 3D generalised model is the GSD model. The M-A relation is then

$$\frac{M\lambda(M)}{M^2-1}\nabla M+\frac{\nabla A}{A}+\mathcal{F}=0$$

With

$$\lambda(M)=\left(1+\frac{2}{\gamma+1}\frac{1-\mu^2}{\mu}\right)\left(1+2\mu+\frac{1}{M^2}\right)$$

And the post-shock Mach number μ from (3.10c). The post-shock contributions are small, $\mathcal{F}\approx 0$, when the area changes are small or in the strong shock limit. Ridoux et al. [2019] present a practical method to discretise and numerically evaluate the GSD model. An advantage is that the discretisation validates the small area change assumption, but shear interaction between the ray tubes with solid walls is neglected. Because this model is quite involved, it is only briefly mentioned here as a suggestion for future research.

4.5 Comparison of Q1D models

The blast wave overpressure decay is displayed Figure 4.8 for the (blue) 1D, (green) volumetric, and (black) planar approach using the initial conditions of Table 4.1. The breach holes have 0.02, 0.2, 0.6 and 1.0 m diameter[3] and are placed into a 1.0 m diameter tunnel (as used throughout this thesis). The grey solid line indicates the critical shock position and the grey dotted line indicates the transition location according to the correlation by Benselama et al. [2010] in Equation 4.3. As expected, larger hole size:

- Extends the critical shock position, because it increases proportionally to the hole size, and
- Reduces the transition position, because blast energies scale with the cube of the hole size. The bow shock flattens closer to the hole location, because the maximum deflection angle decreases (Equation 4.2).

The transition location is always smaller than the tube diameter. This may either indicate that the correlation does not apply to the hyperloop tube ambient (pressure) conditions or that the blast wave almost instantaneously flattens. The former explanation seems more likely, comparing once more with Figure 4.4.

The 1D overpressure model (horizontal blue solid line) does not yield any decay as previously discussed, but it presented a starting point for more in-depth Q1D analyses. The 1D model predictably yields identically the same result irrespective of the hole size, that is, the 1D overpressure does indeed not depend on hole size.

The green dashed curves are obtained by using the Kinney–Graham empirical blast wave decay relation (3.13b). The thin dashes are the uncorrected free field blast wave decays. This decay is faster than the heavy dashes of the blast wave decay corrected with the ECF. In the blast

---

[3] Section 4.3 and Section 4.4 briefly show how the breach hole size affects blast wave overpressure and how it is implemented into the respective models.

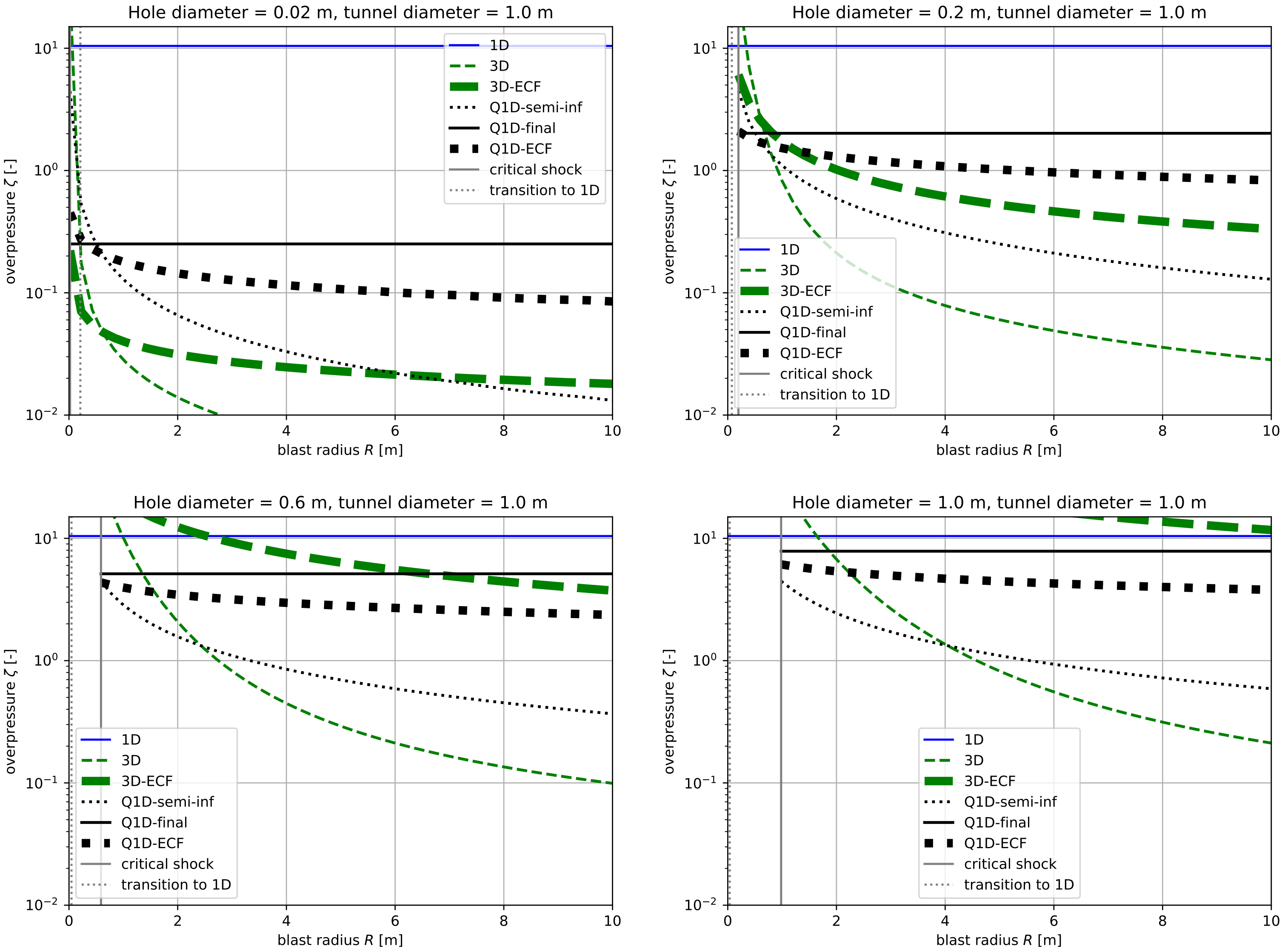

Figure 4.8: Blast wave decay models compared for four breach hole sizes.

wave decay models the shock continues to decay in the far-field, but with the tube confinement correction ECF, the decay is less rapid.

The planar Q1D model (black dotted curves) yields a decay until the final shock area has been achieved and the final overpressure agrees with Figure 4.7. The final overpressure is indicated with a black solid (horizontal) line. The Q1D model can however be extended as if the tube is infinitely large, i.e. a free-field decay. This can then be corrected for the confinement of the tunnel with the ECF. In this case the planar shock strength does decay, but the implementation is an ad-hoc correction based on expected decay due to viscous effects ignored in the original CCW model.

Close to the hole the overpressure may be enormous due to the steady state underexpanded jet, but depending on the model and hole size, the overpressure may already decay several orders of magnitude in only a few meters (or tunnel diameters).

Generally the 1D result represents the maximum attainable overpressure. However, a radial hole with the size of the tube cross-section, yields an exceptionally high blast wave according to the (corrected) volumetric energy method. Interestingly, the planar method yields a lower final overpressure, because the initial blast wave has to travel in both directions through the tube, whereas the 1D result only accounts for one normal shock wave.

Chapter 5

CFD model

This chapter discusses the penultimate sub-question regarding the validation of the one-dimensional model: *What is the accuracy of the predictions made by the one-dimensional model?* Careful considerations are required to properly analyse flows using computational fluid dynamics (CFD). Otherwise, the results may become meaningless. In the present case, the goal of the CFD analysis is to ensure the quasi-one-dimensional (Q1D) model yields adequate results. Therefore, the subsequent CFD analyses shall also employ the Euler equations (3.6).

The model setup is declared in Section 5.1 and the results of the analysis are discussed in Section 5.2. Finally, a comparison with the Q1D modelling of the previous chapter is made in Section 5.3.

5.1 Model setup

The fluid solver of Ansys Discovery AIM software is selected. The software integrates geometry, mesh and physics modelling with solving and post-processing. Details of the selected simulation options are motivated below.

The solver is based on the *finite volume* method. This solves the Euler equations in integral form, not requiring mathematical continuity. In other words, discontinuous shocks are allowed. Anderson [1995] states that this is why the integral form is "more fundamental" than the differential form. Another advantage is the applicability to unstructured meshes and of boundary conditions. The dependent variables — velocity, density, pressure and energy — are evaluated at the cell centres, whereas the boundary conditions are applied at the boundary faces. Alternative methods used to numerically analyse partial differential equation (PDE)s are finite difference and finite element methods.

In order to successfully simulate the physics it is necessary to model the physical domain (hyperloop tube) and phenomena (conservation and equations of state). The domain and the conservation equations have to be discretised and linearised in order to transform the PDEs to a system of linear algebraic equations, which can be numerically solved to find the unknowns, e.g. velocity, pressure, and temperature. Note that for transient analyses, time shall be discretised as well.

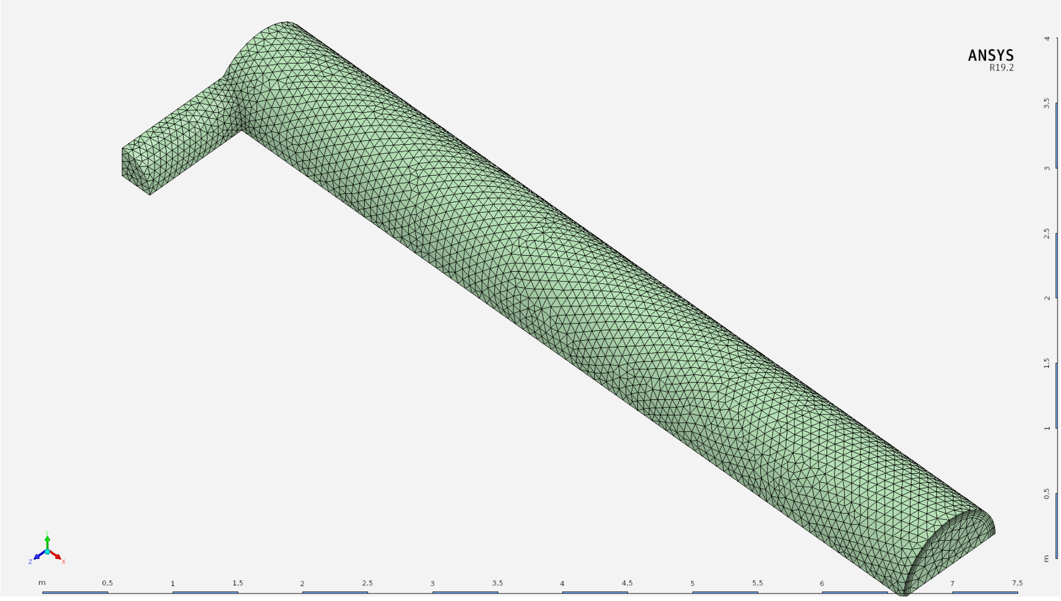

Figure 5.1: The mesh geometry of a 30 cm radius breach hole setup.

5.1.1 General settings

The following settings selection is mainly based on the software user manual, see ANSYS [2010]. The selected solving method is *pressure-based*. Historically the density-based approach was developed for compressible flows, whereas pressure-based solving was developed for incompressible flows. With current extensions, both methods are able to solve compressible flows. (ANSYS [2010]) Only the pressure-based solver is available in the used software. Both methods obtain the velocity field from the momentum conservation equations. The pressure-based approach yields the pressure field from a combination of all conservation equations. The density-based approach however only uses the continuity equation to determine the density field first, and finds the pressure field through the equation of state. The result is that the two approaches linearise the equations differently.

The aforementioned combination of conservation equations are *coupled and non-linear*. The alternative segregated approach solves for pressure by sequentially solving the equations iteratively until the convergence of results. The coupled approach, on the other hand, solves the continuity and momentum equations simultaneously and next the energy equation iteratively. The advantage is a faster convergence rate, but it is at the cost of an increased memory requirement. A coupled approach is advised for large time steps and low quality meshes. The coupled pressure-based algorithm is used instead of a segregated one (such as SIMPLE, PISO). (ANSYS [2010])

It is also advised by ANSYS [2010] to reduce the under-relaxation factor for the momentum equations in inviscid simulations, to enhance the solving stability in the pressure-based approach. The first 10 time steps to be resolved were small at 0.01 μs. Moreover, the inlet boundary was velocity based instead of mass flow or pressure definition.

The time discretisation is *second order backward Euler* which is common for transient analyses according to (ANSYS [2010]). This approach is implicit (which is more stable than explicit time schemes) and more accurate in time. The discretisation is *iterative* instead of non-iterative timeadvancing (NITA). The latter may have given a faster convergence rate because the fully coupled set of equations are not always accurately resolved in time, and as long as the error lies within the truncation error, this would be sufficient.

The pressure is interpolated with the *second order upwind* scheme, which is recommended by ANSYS [2010] for compressible flows. The spatial discretisation is second order upwind as well. Although a first order scheme converges more easily, its downside is the high numerical diffusion if the mesh is not aligned with the flow.[1]

Gradients and derivatives are determined using the *least-squares cell-based* method. For unstructured meshes, this method is accurate similarly to node-based Green-Gauss, but faster. The method is also preferred over the cell-based Green-Gauss method.

The *tolerances* of the residuals are required to be less than 10^{-5} and each time step is allowed 10 iterations to converge. The final maximum residual is 10^{-3} for continuity, 10^{-4} for the three mutually orthogonal velocity vectors and the total enthalpy. The temporal error tolerance is 10^{-3}. The largest residuals occur at the expansion at the breach hole due to the right angle turn the flow encounters at the wall.

5.1.2 Initial and boundary conditions

The simulated medium is continuous (because Kn $\ll 1$) air as a compressible ideal gas (because $M > 0.3$). The stagnant initial condition ($\mathbf{u}_0 = \mathbf{0}$) is at an absolute pressure of 101 Pa at 15 °C temperature. It is important to set the gauge pressure to zero, because all pressures are with respect to an absolute vacuum.

As previously mentioned, only a tangent flow condition (i.e. no mass transfer) suffices at the walls of the Euler equations, because a no-slip condition would be excessive. In other words, the walls behave as streamlines. The sonic inflow is at 340 m/s with static (critical) pressure 53528 Pa — i.e. 101325 Pa total pressure — at the temperature of 15 °C. The inflow is constant over the full time domain of 0.01 s, because the breach hole remains choked during this time.

The (non-reflective) outflow is at 100 Pa. Again the temperature is imposed for the energy equation at 15 °C. The outflow condition is subsonic, because the simulation is stopped before the shock reaches the outflow boundary.

Two symmetry planes are used to reduce the computational load. The quartered (symmetrical) geometry consists of a 7.5 m tunnel length by 1.0 m tunnel diameter. The inlet enters the tunnel radially and has a 1 m run-up section similar to those used in the loss of vacuum accident (LOVA) CFD analyses in Section 3.3, compare Figure 3.13 and Figure 5.1. A shock wave travelling (for example) at a constant speed of 850 m/s originating at the inflow may reach the domain outflow within the 0.01 s time domain. Based on the results in the previous chapter it is expected that the shock speed is only slightly lower, namely 805 m/s. The selected hole sizes correspond to those of the Q1D analysis: 0.02, 0.2 and 0.6 m diameter.

5.1.3 Mesh (convergence)

The domain is discretised into a tetrahedral core with a hexahedral (pseudo) boundary layer. Even though the flow is inviscid, the boundary layer is added to prevent that the solution diverges.

---

[1] This is indeed the case when using an unstructured mesh.

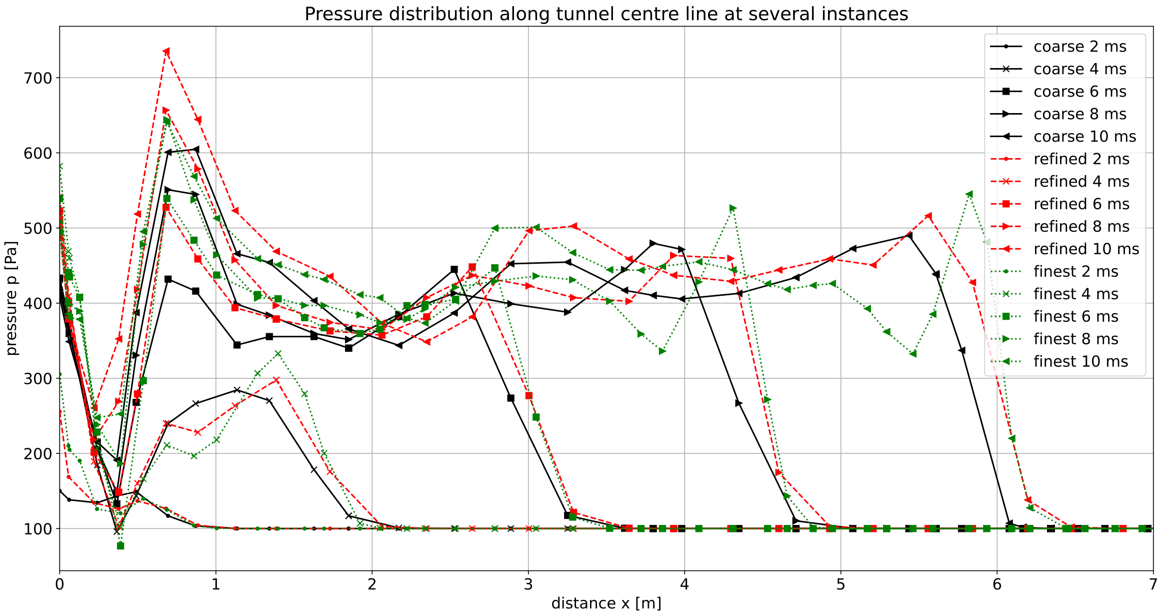

Figure 5.2: The pressure development along the tunnel center line for several mesh refinements.

Extremely low temperatures due to expansion around the corner of the hole cause peak values in the solution. Hence, this boundary layer is installed to prevent this. Due to easier implementation, an otherwise unstructured domain was preferred.

Three mesh refinements have been used to analyse their effect on the solution values. The finest mesh has smaller model error, but larger computational cost. This is because (1) more cells have to be resolved and (2) smaller time steps are required to adhere to Courant–Friedrichs–Lewy (CFL) condition that the Courant number must be smaller than unity to capture the shocks. For the finest mesh, the maximum allowed time step is in the order of 1 μs.

A coarse mesh does not pinpoint the shock position and approximates the circular geometry only as a coarse polygon. Also, a coarse mesh leads to high numerical diffusion.

The domain has been discretised into three levels of refinement: coarse, refined, and finest. The number of elements in each domain is 3401, 7493, and 20810, respectively. Figure 5.2 shows the pressure development about the tunnel center line for the three mesh refinements. Because all three results appear similar, and because the residual errors are low, it may be assumed that the simulation has sufficiently converged to a valid solution.

5.2 CFD analysis results

This section presents the results of the previously described CFD model. First, sequences of pressure and velocity contour plots give an understanding of the general aspects of the 3D flow field and next the pressure results along the tube center line are discussed. The final section of this chapter compares these results to the Q1D model of the previous chapter.

5.2.1 Pressure contour plots

Figure 5.3 shows the contour plots of the tube midplane pressure over the time domain ($0 \leq t \leq 10$ ms) with 1 ms between the frames. This is the result for a 20 cm diameter hole. The air flow develops as follows. First, atmospheric air from outside the tube enters through the run-up section of the breach hole similar to the LOVA CFD analysis in Figure 3.13. An underexpanded jet forms at the breach entrance to the tube while the blast wave travels through the tube. The blast wave indeed develops from a 3D bow shock to an imperfectly planar normal shock wave: it is only approximately uniform. A high pressure zone develops opposite of the breach hole due to the impinging jet.

The color scale of the contour plot is a logarithmic scale to clearly capture the development of the blast wave front and the full pressure range from critical pressure to tube pressure in one figure. Although the unperturbed tube is a uniform zone, the preshock conditions[2] are not.

The minimum and maximum values and their locations are indicated as well. Note that the minimum pressure occurs near the underexpanded jet and is lower than the ambient tube pressure of 0.001 atm. Particularly in the first stages, this pressure approaches absolute vacuum, which caused diverging solutions. Air moisture would condensate due to the expansion. The maximum pressure, i.e. the critical pressure, occurs at the air inlet, as expected.

---

[2] The definition of *preshock condition* may be ambiguous in this case. Spatially the zone before the shock (closest to the breach) is the preshock. It is **not** meant in a temporal sense (before the shock has passed) which would in fact be the opposite — enantiosemy.

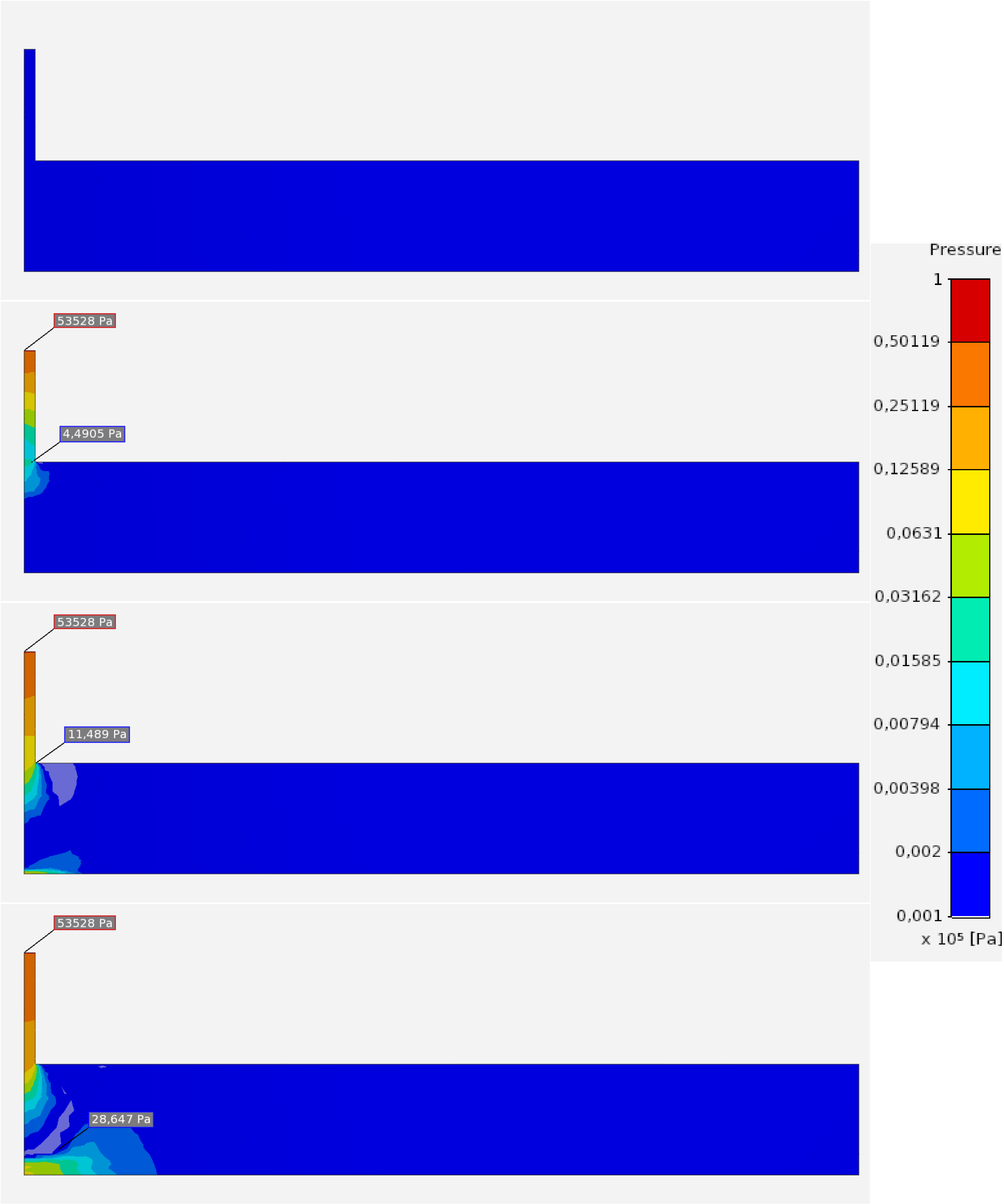
53528 Pa
4,4905 Pa
53528 Pa
11,489 Pa
53528 Pa
28,647 Pa
Pressure
1
0,50119
0,25119
0,12589
0,0631
0,03162
0,01585
0,00794
0,00398
0,002
0,001
x 10⁵ [Pa]

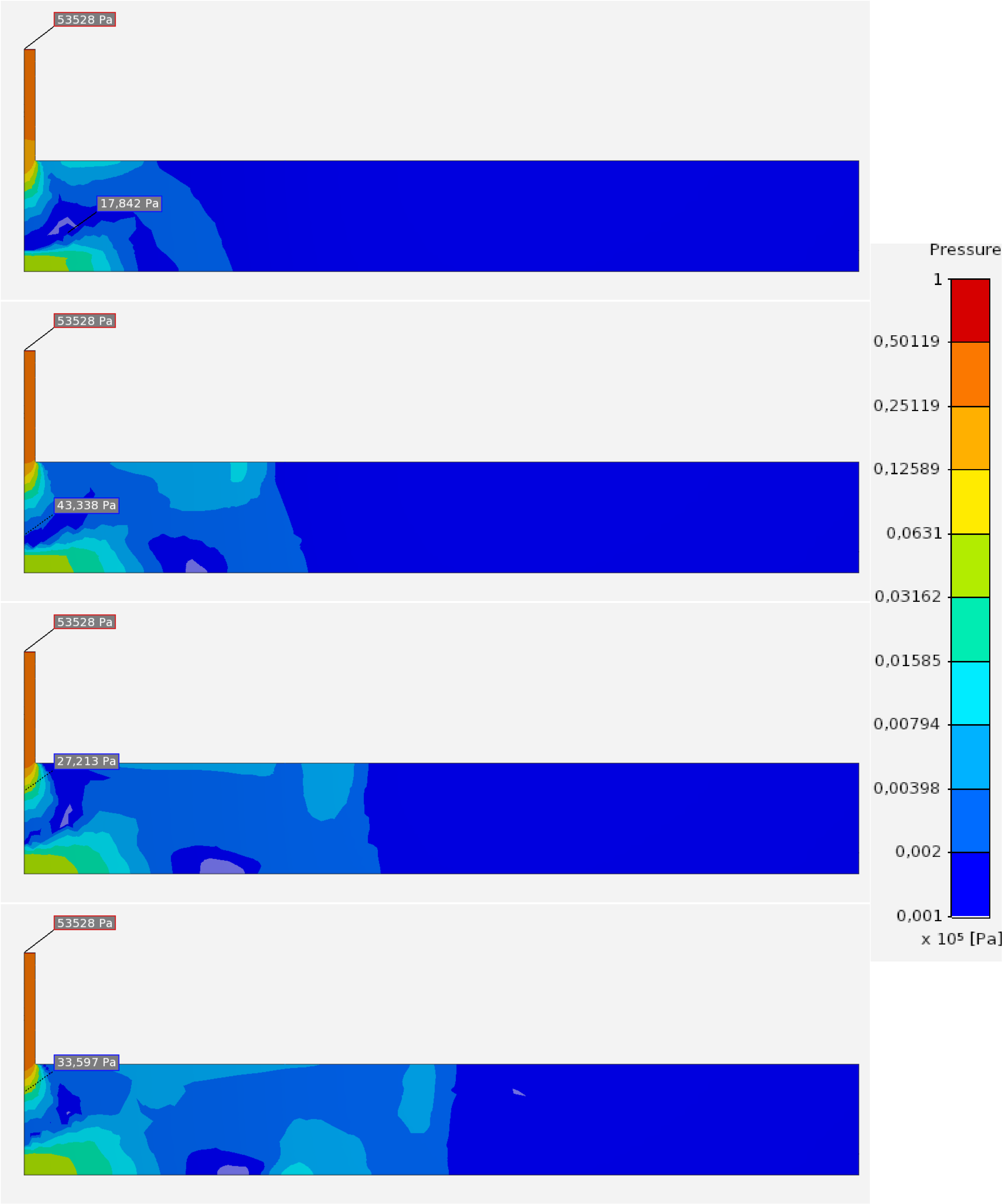
53528 Pa
17,842 Pa
53528 Pa
43,338 Pa
53528 Pa
27,213 Pa
53528 Pa
33,597 Pa
Pressure
1
0,50119
0,25119
0,12589
0,0631
0,03162
0,01585
0,00794
0,00398
0,002
0,001
x 10⁵ [Pa]

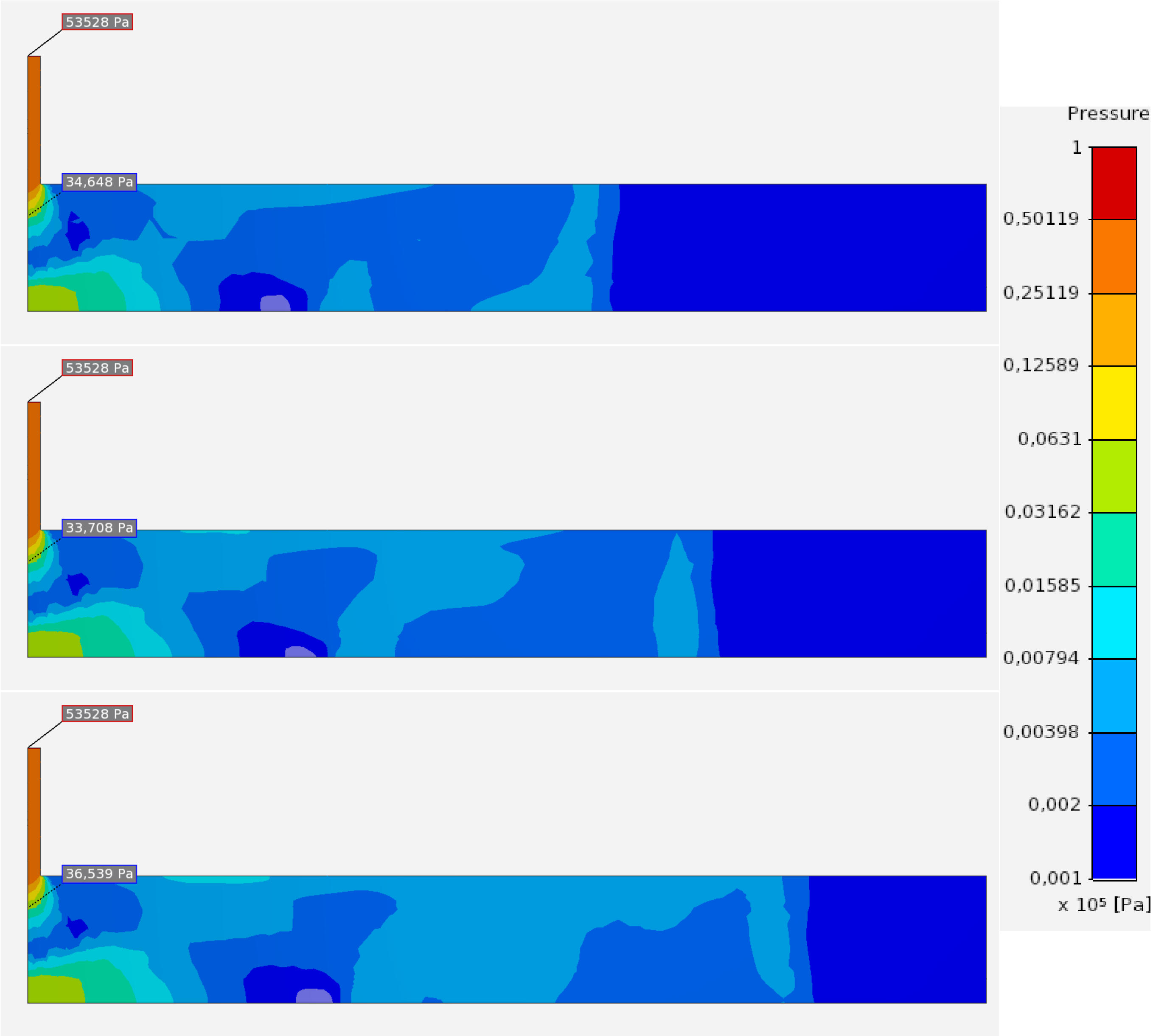

Figure 5.3: Tube pressure contour plots in time domain $0 \leq t \leq 10$ ms with 1 ms time step showing the blast wave development.

5.2.2 Velocity contour plots

Figures 5.4 and 5.5 show the velocity magnitude development on the midplane and near the tube walls respectively. The time step is again 1 ms between each frame over the same time domain as the pressure contour plots, but the first four time steps are omitted for the tube wall view, because they do not offer additional information. It is the geometry of the 10 cm breach hole as well.

The initial highly underexpanded jet indeed displays the contours of Figure 3.4 (turned 90 degrees) and only consists of one barrel shock due to the high pressure ratio. The core of the barrel slows down over time. It appears that a high-velocity vortex develops due to the impingement on the walls opposite the breach hole. This vortex then stays at a fixed position, slowing down as well. The shock position is again clearly seen marching through the tube.

The maximum velocity location shifts from inlet (i.e. the sonic initial condition), to the underexpanded jet core, to the impingement vortex core, to the tube walls. Towards the end of the simulation, high velocities are reached near the preshock zone at the walls, while a lower velocity occurs at the core flow. The wall velocity would slow down more in a viscous simulation due to the no-slip condition at the wall. Trivially, the minimum (zero) velocity is the unperturbed postshock zone.

Using the scale of the tube and time allows an approximate computation of the shock speed. The normal shock travels on average 3 m in 4 ms, or at a speed of 750 m/s. (A more in-depth analysis of the shock speed is presented in the next sections.) Nonetheless, the maximum speed of the air may be locally higher: the maximum probes indicate air speeds above 1000 m/s.

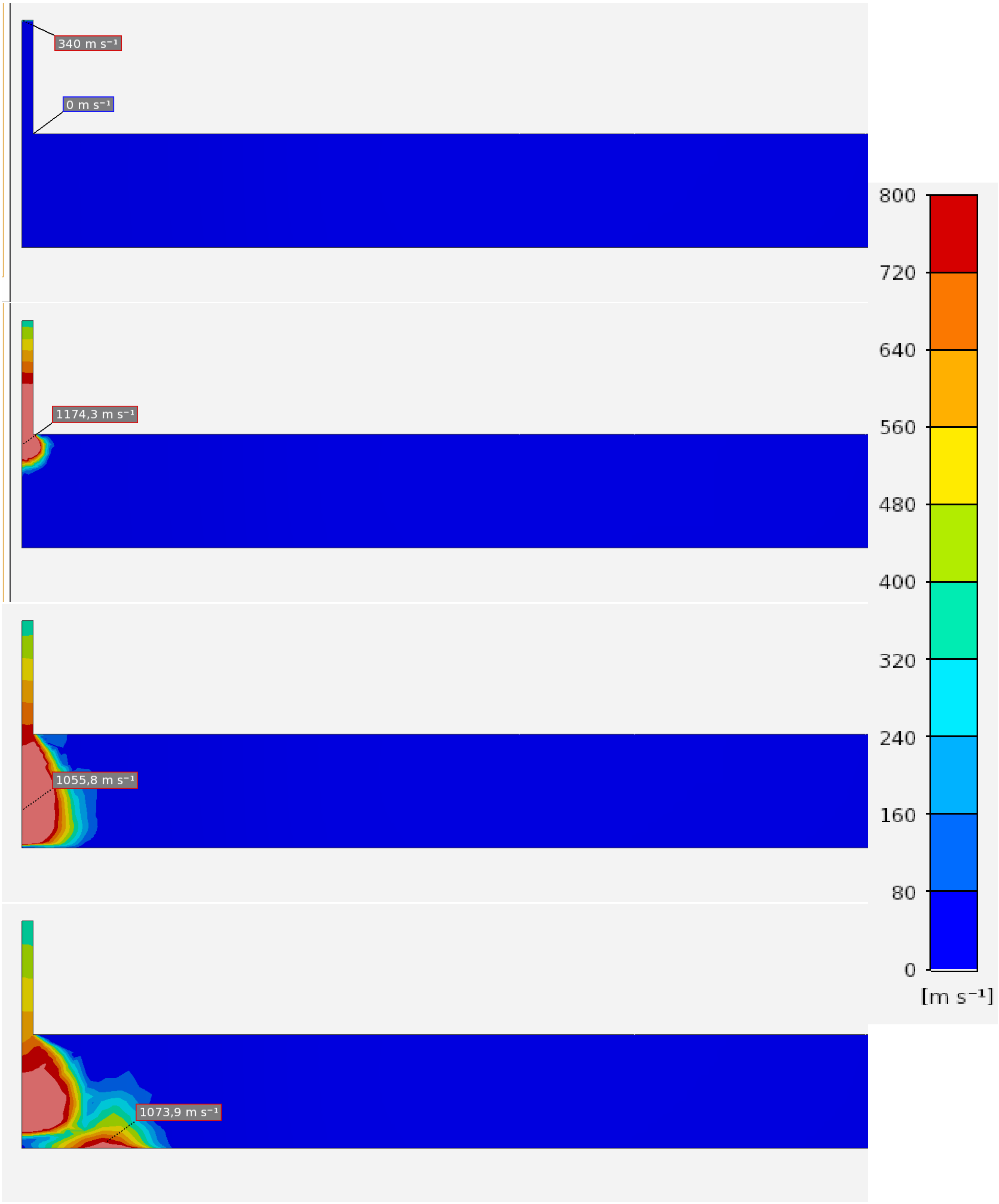
340 m s⁻¹
0 m s⁻¹
1174,3 m s⁻¹
1055,8 m s⁻¹
1073,9 m s⁻¹
800
720
640
560
480
400
320
240
160
80
0
[m s⁻¹]

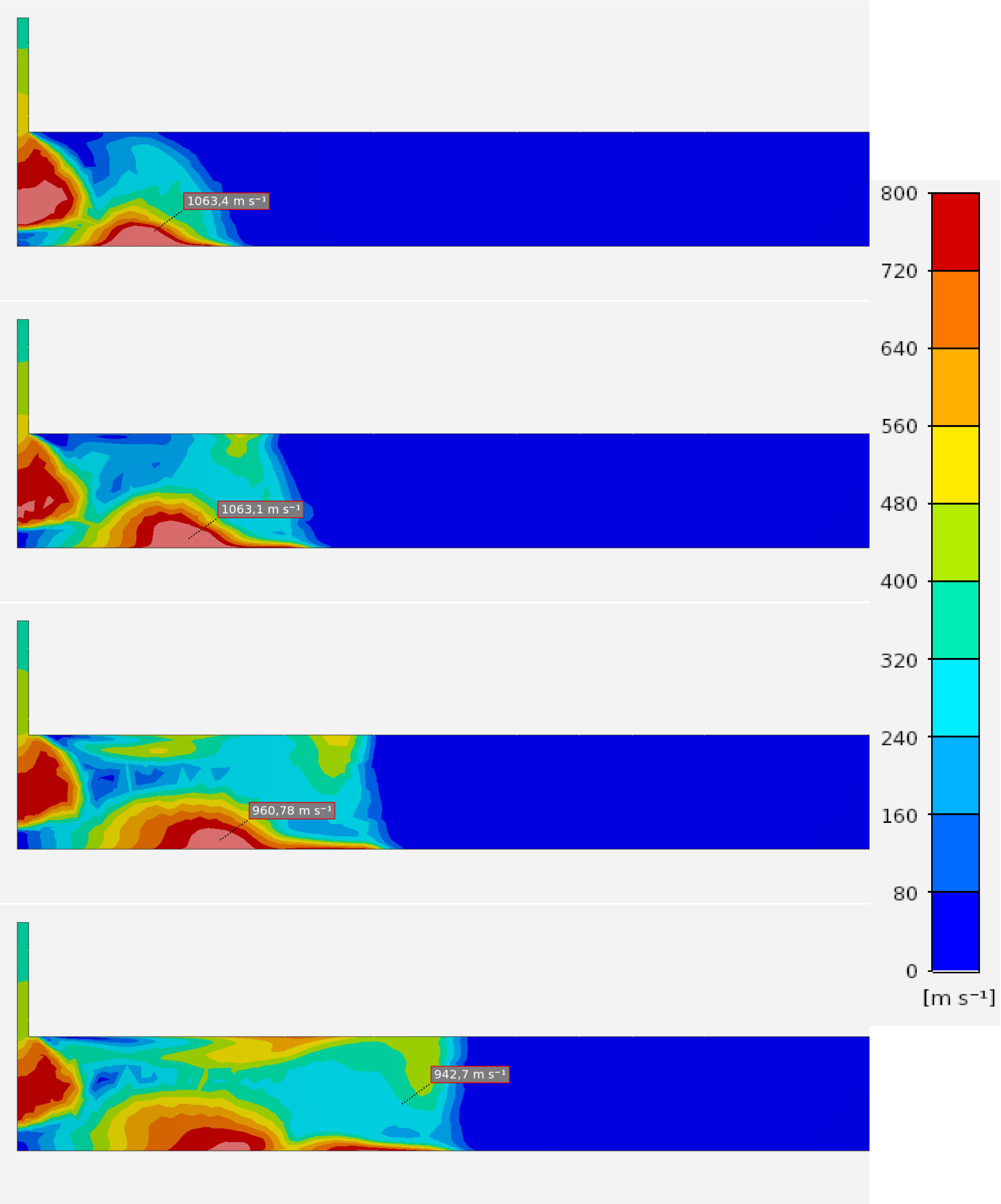
1063,4 m s⁻¹
1063,1 m s⁻¹
960,78 m s⁻¹
942,7 m s⁻¹
800
720
640
560
480
400
320
240
160
80
0
[m s⁻¹]

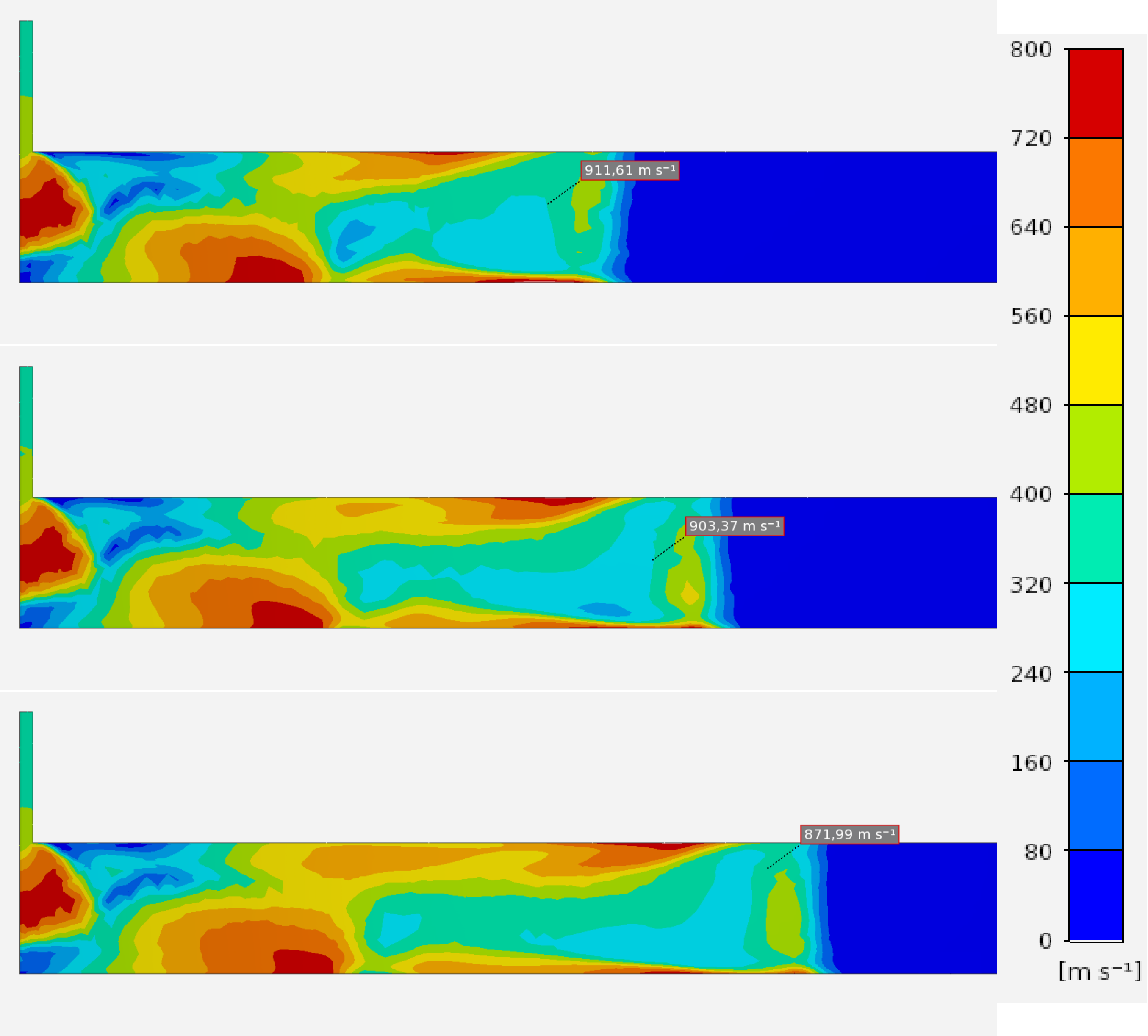

Figure 5.4: Tube velocity magnitude contour plots in time domain $0 \leq t \leq 10$ ms with 1 ms time step showing the blast wave development in the tube midplane.

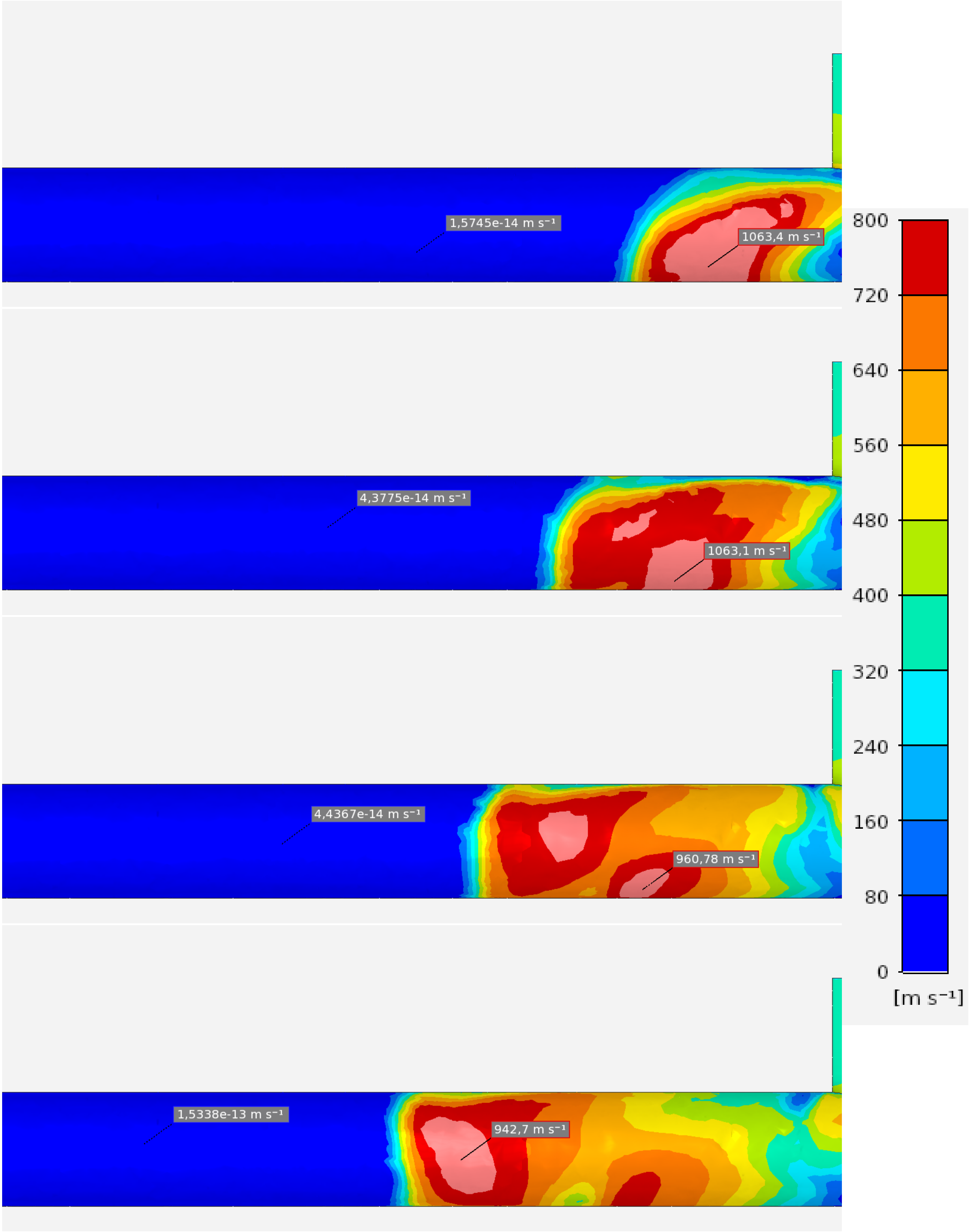
1,5745e-14 m s⁻¹
1063,4 m s⁻¹
4,3775e-14 m s⁻¹
1063,1 m s⁻¹
4,4367e-14 m s⁻¹
960,78 m s⁻¹
1,5338e-13 m s⁻¹
942,7 m s⁻¹
800
720
640
560
480
400
320
240
160
80
0
[m s⁻¹]

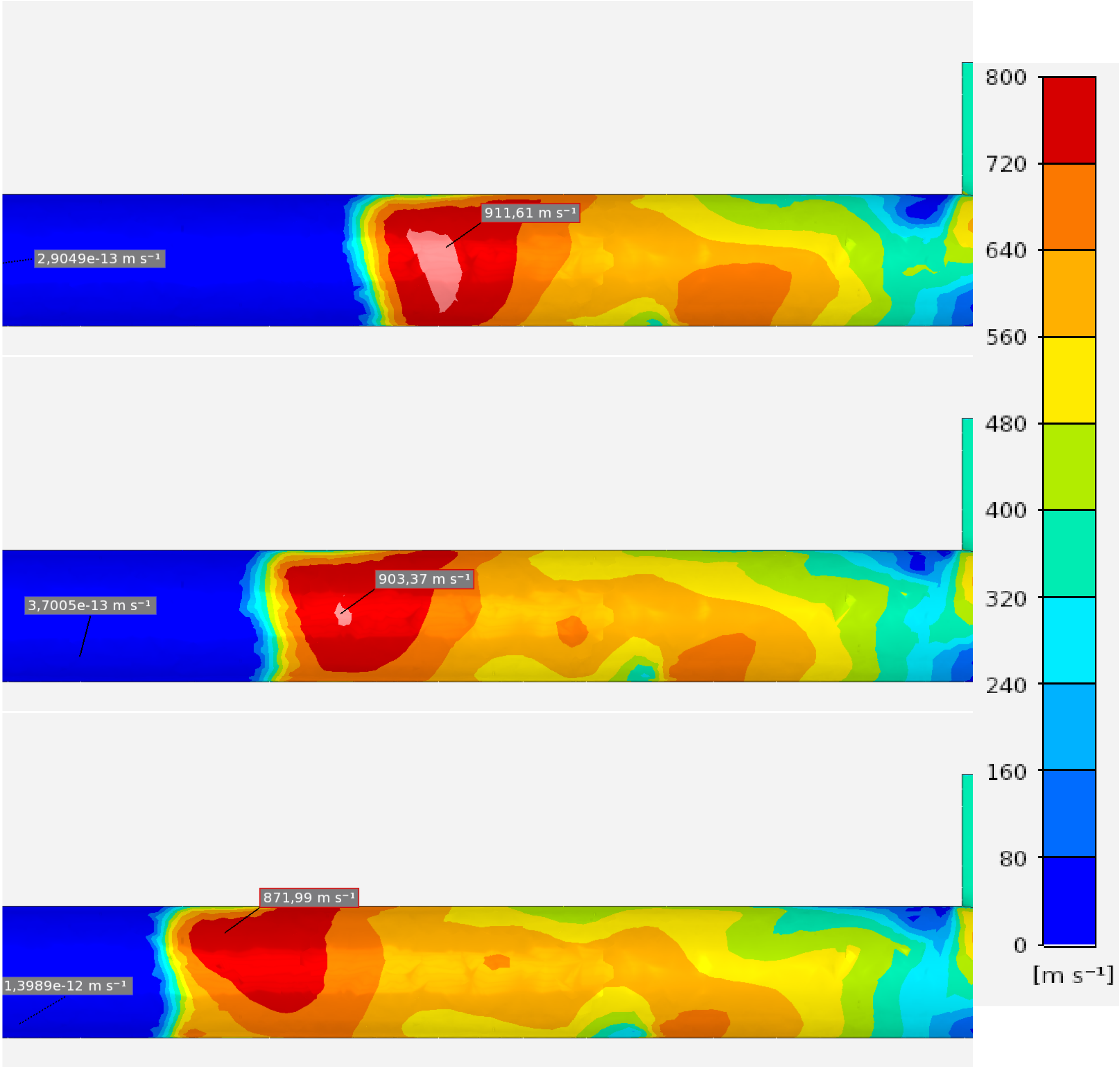

Figure 5.5: Tube velocity magnitude contour plots of the tube top view in time domain $4 \leq t \leq 10$ ms with 1 ms time step showing the blast wave development near the walls.

5.2.3 Overpressure versus hole size

Figures 5.6 and 5.7 show the pressure distribution development along the pod axis for the three breach hole sizes at low and high pressure scale, respectively. The line thickness of the pressure signal increases with time. Indeed the peak pressure increases with hole size, recall Figure 4.7. Pressure peaks at the x-location of the hole ($X = 0$) due to the underexpanded jet. In contrast, the unperturbed tube region remains around 100 Pa. Moreover, a pressure dip below the ambient tube pressure is seen near the inlet hole. This is due to the expansion of the flow around the right angle corner. The travelling waves are clearly seen and autocorrelation of the subsequent pressure signals may determine the shock speed. Alternatively, the peak overpressures are simply measured by the pressure scale.

Table 5.1 presents an overview of these results. For each hole diameter D_h, the shock speed u_s is determined by dividing the distance travelled by the shock by the time step. This shock speed is then used to find the overpressure ζ_s, according to Equation 3.12c. Alternatively, the peak overpressure ζ_p is directly retrieved from Figure 5.6, although this is undefined for the largest hole size, because it has no constant pressure region between the shock and breach origin. The rightmost column shows the final overpressure according to the planar Q1D approach, see Figure 4.7.

The overpressure found indirectly by the shock speed and directly from the pressure signal do not perfectly match. This is because the shock speed–overpressure equation (3.12c) describes a steady normal shock wave. However, as seen in the contour plots, the shock wave only approximately normalises.

The largest hole demonstrates the largest discrepancy with respect to the Q1D models. Unlike the smaller breach hole scenarios, the pressure increases towards the breach origin without plateauing. Moreover, the shock speed and overpressure are considerably larger than the maximum values expected from the Riemann shock tube analysis. The cause for this discrepancy is hypothesised in the next section. Note that once the shock reaches outflow boundary condition the solution diverges, so the largest hole simulation had to be aborted after only 8 ms.

Table 5.1: Overpressure results for each of the analysed hole diameters. (*) The peak overpressure for the 60 cm diameter hole is undefined.

D_h [m]	u_s [m/s]	ζ_s [-]	ζ_p [-]	ζ_{Q1D} [-]
0.02	405	0.49	0.82	0.25
0.2	647	3.06	3.82	2.02
0.6	1245	14.48	(*)	5.13

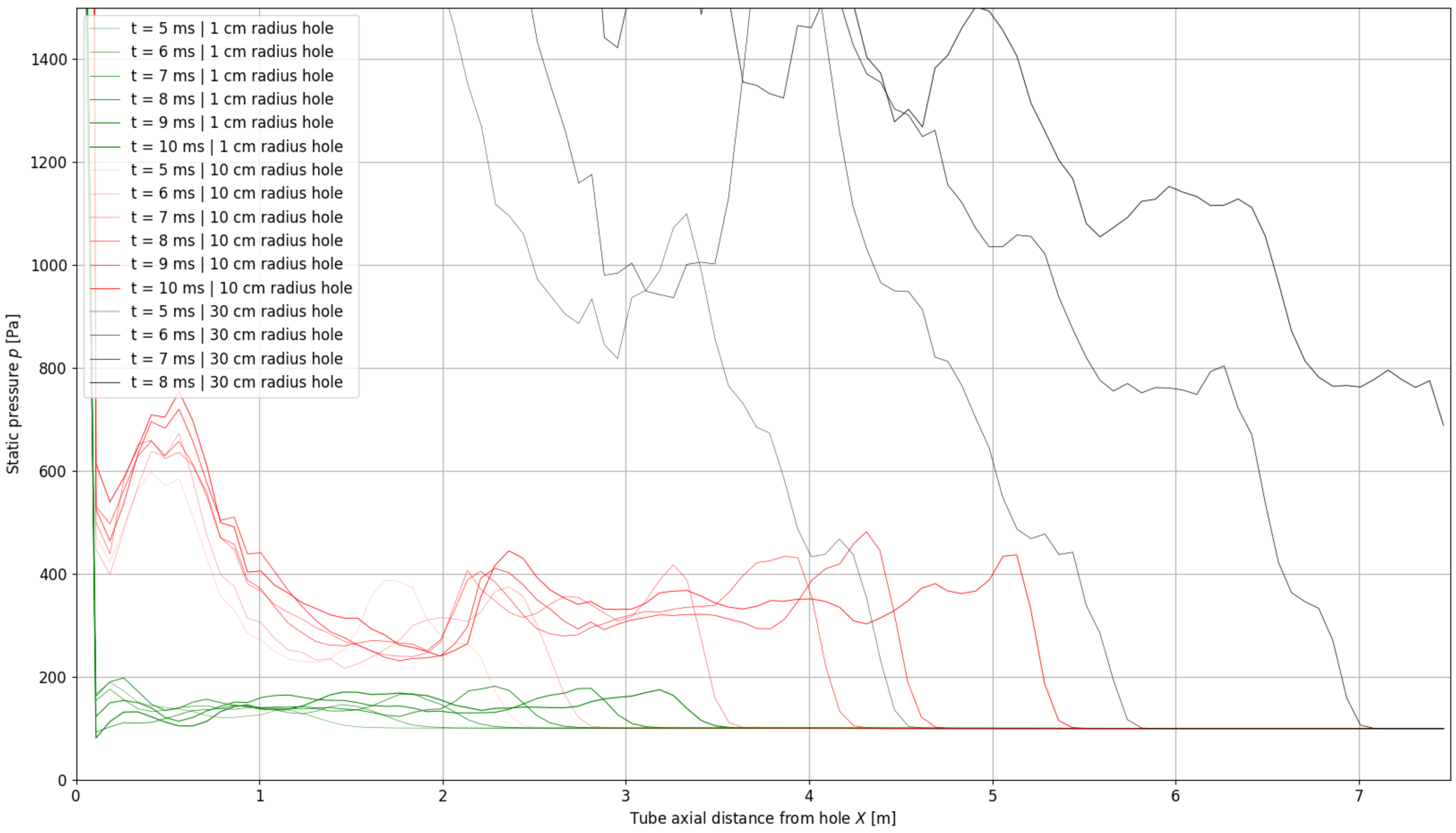

Figure 5.6: The pressure distribution along the pod axis for three different breach holes (at small overpressures).

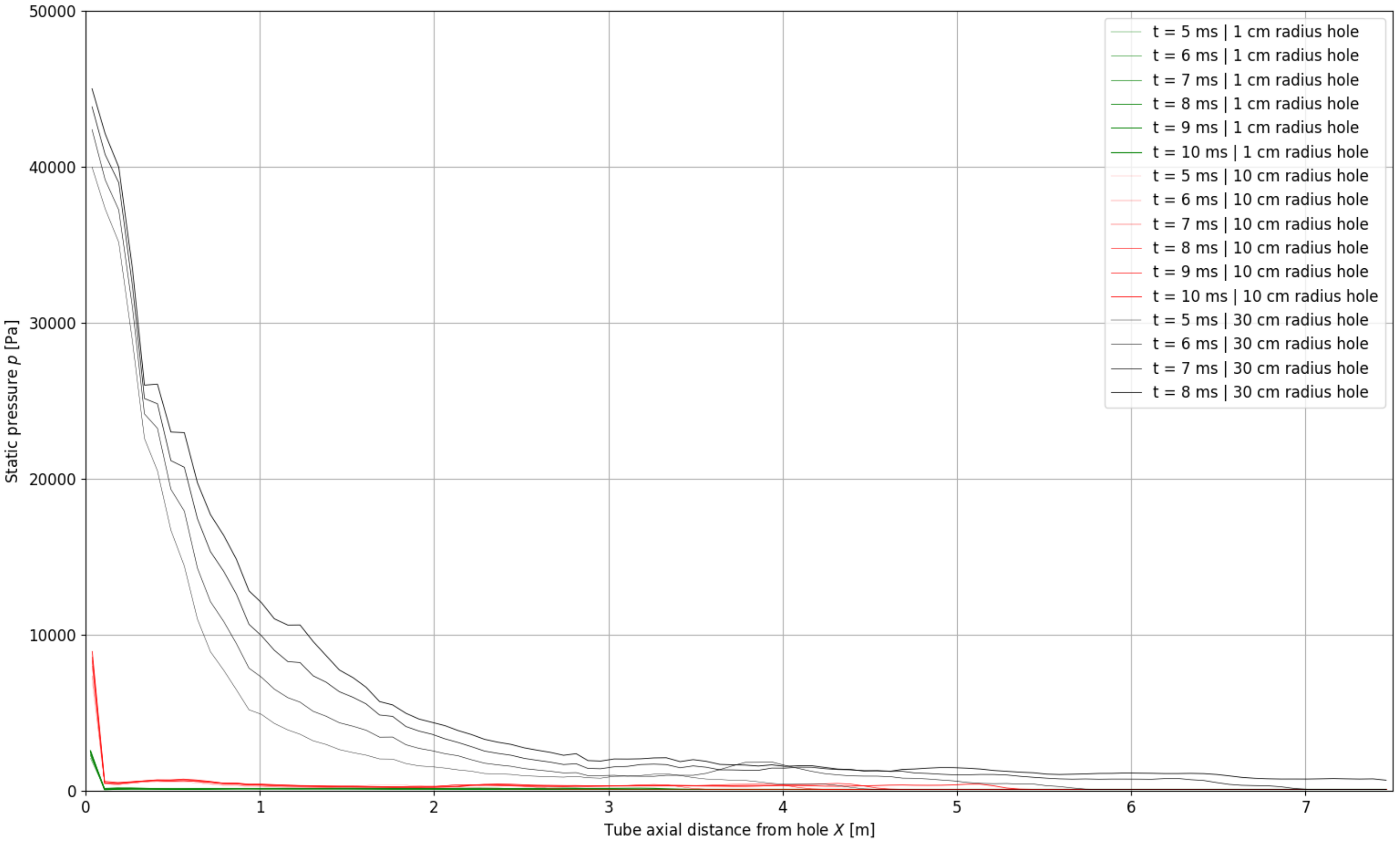

Figure 5.7: The pressure distribution along the pod axis for three different breach holes (at large overpressures).

5.3 Comparison of models

The CFD analysis of the three-dimensional (3D) Euler equations on the tube domain reveals that indeed the overpressure of the blast wave does not decay considerably. This is due to the inviscid flow: viscosity cannot dissipate the energy of the blast wave. For instance, the no-slip condition at the tube walls would slow down the preshock air flow. Still, to find the spatiotemporal development of a normal shock wave, this viscosity is not immediately required. The boundary layer emanates at the shock position.

Unlike the case of a chemical explosion, the kinetic and pressure energy of the tube breach keep adding energy to the system even after the initial critical shock. The pressure signal at one location therefore does not follow the Friedlander curve in Figure 3.11.[3] It is this continuous inflow rather than an impulsive critical shock which invalidates the Q1D model for large breach holes. The effect due to the incessant addition of energy is mainly discernible at high overpressures. This also means that overpressures beyond those calculated by the Riemann shock tube scenario are possible, although a pressure increase more gradual than the discontinuous normal shock wave is expected.

So although according to the comparison of the CFD computed overpressures with the results from the Q1D analysis, the CFD analysis does yield higher overpressures, the values still agree well for smaller hole sizes. Yet, whereas the 1D shock tube displays uniform preshock conditions, the 3D CFD analysis yields more knowledge of the flow development and interaction with the tube walls. This however comes at a higher computational cost than the simpler, low-fidelity Q1D models.

Figure 5.8 is a reiteration of Figure 4.8 and now includes the results of the CFD analysis (see Table 5.1) to emphasise the differences between both models. The fluctuating constant pressure zone in the CFD results is visualised by a wide semi-transparent red line. For the 0.6 m diameter hole (Figure 5.8c), the overpressure continues to increase towards the blast origin, cf. Figure 5.7. The final Q1D overpressure is the horizontal black line, cf. Figure 4.7. Only the corrected free field pressure decays due to the equivalent TNT (volumetric) and the CCW (planar) method are included to not overcrowd the figures. The curves start at the critical shock position. Indeed the CFD overpressures are systematically higher than those predicted by Q1D methods due to their lack of including the energy addition after the critical shock formed.

---

[3] Sidenote: the pressure signal resembles a pressure drop versus fluid bed velocity graph.

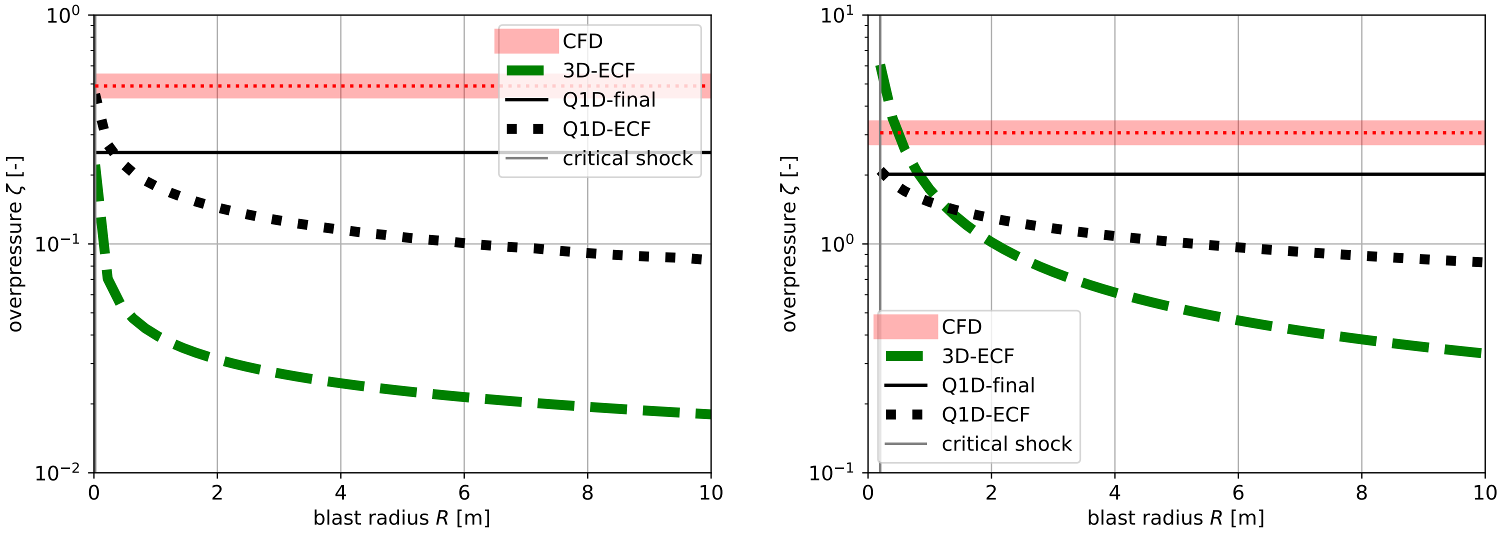

(a) The hole diameter is 0.02 m for tube diameter 1.0 m. **(b)** The hole diameter is 0.2 m for tube diameter 1.0 m.

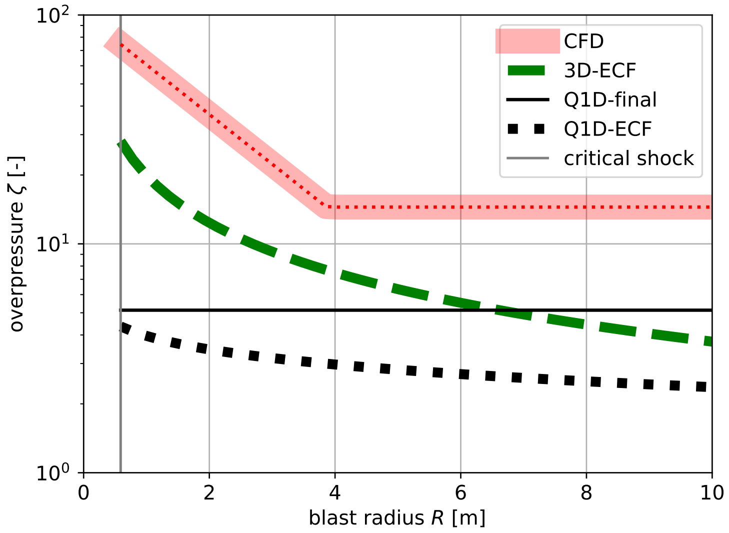

(c) The hole diameter is 0.6 m for tube diameter 1.0 m.

Figure 5.8: Comparison of results obtained by Q1D models and the CFD model.

Chapter 6

Conclusion

This chapter concludes the thesis with a discussion of the final sub-question and the main research question:

- *What is the magnitude of the expected additional forces?*
- **What are the additional aerodynamic forces on hyperloop pods that may be expected in case of a given near-vacuum tube breach scenario according to a validated one-dimensional analysis?**

The overpressure results of the different models that have been discussed in this thesis generally align with each other: the worst case scenario breach leads to overpressures with an order of magnitude higher than the ambient tube pressure. Near the breach hole, the underexpanded jet may locally cause overpressures up to three orders of magnitude higher than the ambient tube pressure.

This chapter first discusses the validity of the used models in Section 6.1, then presents the expected additional forces due to a blast wave in Section 6.2 and finally has three recommendations for future aerodynamic research on the topic of hyperloop tube breach in Section 6.3.

6.1 Model validity

Many sources for errors with respect to reality are introduced in the process of a simulation. Reality is first reduced to a physical model: conservation laws and equations of state. A large Knudsen number or extreme temperatures can invalidate these laws respectively. Next this physical model is mathematically approximated with a system of partial differential equations. Assuming an inviscid continuum and a perfect gas, this led to the Euler equations. Nevertheless, the unsteady and compressible effects have to be taken into account. Thecomputational fluid dynamics (CFD) adds a numerical error due to the spatial and temporal discretisation, iteration and machine (computer round-off) error. These errors can be reduced by improving grid quality, cell size and time step,

Table 6.1: Model strengths and weaknesses.

Model	Strength	Weakness
1D shock tube	Straightforward use	Limited applicability
Q1D volumetric	Decay empirically validated	Experiments at standard atmosphere
Q1D planar	Direct implementation of Euler	Decay is artificially added
Q1D general	Low computational cost	Excludes energy input after critical shock
CFD validation model	Offered new insights	Run-up section
CFD general	High fidelity	High computational cost

selecting a high-order methods and reducing the tolerance of residuals. A programming error may also be a source of error, but cannot be acknowledged.

Table 6.1 summarises the strength and weaknesses in each of the models used in this thesis. The 1D shock tube although simple, offered a solid basis for the Q1D models. The TNT-equivalence model has been empirically validated at standard atmosphere, but not at the low vacuum environment of the hyperloop tube. The planar formulation directly applied the Euler equations, which excludes viscous decay. Generally, the Q1D models excluded the additional energy input after the initial critical shock. The CFD model did include this, but came at a higher computational cost. Reconsidering the implementation of the CFD model, the run-up section only allows a cylindrical entry of atmospheric air. Using two connected domains at different initial pressure may show a more conically shaped inflow from outside the tube.

6.2 Additional drag due to breach blast wave

Figure 6.1 shows the added drag due to a breach blast wave of one order of magnitude higher than the ambient tube pressure, which simulates a large breach hole. The preshock pressure is thus 1000 Pa, the tube pressure 100 Pa and shock overpressure is thus 9. In the pod reference frame the shock approaches with the sum of the pod speed and shock speed, the latter determined by the overpressure, cf. Equation 3.12c. Now, the methodology used to determine the pod drag during normal operation (Figure 2.6), is used at the increased tube pressure, i.e. with the added preshock total pressure. In other words, the figure shows the drag comparison of travelling in the 100 Pa tube versus in the preshock zone.

It is clear that this overpressure causes an enormous drag increase. If the pod is slowed down from (300 m/s) cruise speed to 70 m/s before the shock wave arrives, due to timely warning by the leak detection system, then the preshock conditions would increase the pod drag back to the cruise speed level around 400 N. In absence of a timely response, the drag at cruise speed drastically increases to 23 kN.

6.3 Recommendations

The hyperloop research field in general still has many challenges ahead. This thesis also left a few stones unturned. Three major topics come to mind which may yield additional knowledge related to the aerodynamics of a hyperloop tube breach. First, the Euler equations do not account for

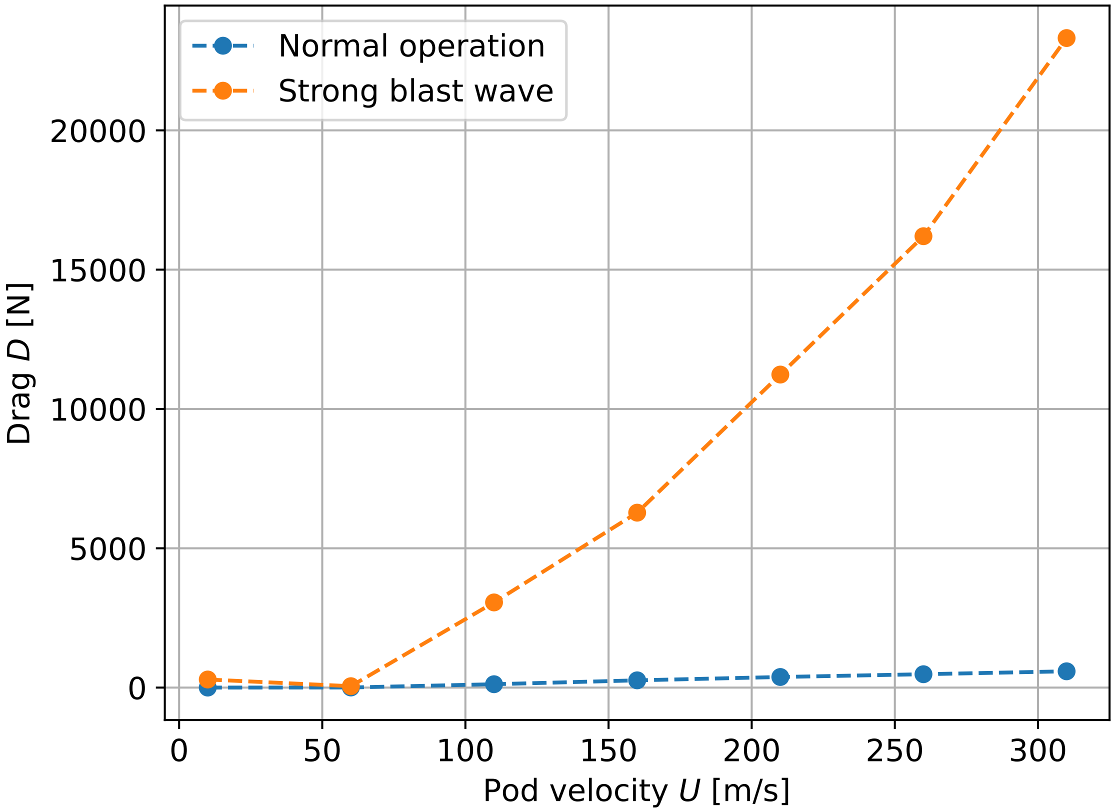

Figure 6.1: Comparison of total aerodynamic drag during normal operation and due to a tube breach.

viscosity and thus the blast wave can travel through the tube unimpeded. Although the viscous effects have been shown to be minimal for smooth pipes, it may be interesting to (experimentally) investigate the viscous decay of shock waves through the hyperloop tube. Wall roughness generally supports the viscous dissipating of flows. Could this alleviate the detrimental effects of the blast wave due to the tube breach?

The second item is further analysis of the underexpanded jet. This thesis mainly focused on the unsteady blast wave effects on the hyperloop pods. However, the underexpanded jet creates even more extreme flow conditions due to the barrel shock and large pressure differences. An analysis using the method of characteristics was unfruitful, due to the lack of variation in Prandtl-Meyer function at high Mach numbers. The jet impingement, the interaction with the wall opposite of the hole may be interesting to analyse.

Finally, the analysis of how the blast wave travels over and interacts with the pods, possibly by use of geometric shock dynamics and the analysis of how some of the proposed mitigating emergency plans (sluices) might work, they have both not been described in this thesis.

Appendix A

Additional information

A.1 Shock between two throats

The flow from the first throat until the shock and the flow after the shock until the second throat are isentropic. The throat to throat flow is adiabatic, i.e. the total temperature remains constant. The total pressure, however does not. Substituting the ideal gas law $p = \rho RT$ and the definition of the Mach number $M = v/\sqrt{\gamma RT}$ into the mass conservation $\dot{m} = \rho A v$ from the station of interest e to the first throat, where $M^\star = 1$, yields

$$\dot{m}_e = \frac{p_e}{RT_e} A_e M_e \sqrt{\gamma RT_e} = p_e A_e M_e \sqrt{\frac{\gamma}{RT_e}} = \dot{m}^\star = p^\star A^\star \sqrt{\frac{\gamma}{RT^\star}}$$

Rearranging to

$$M_e^2 = \left(\frac{A^\star}{A_e} \frac{p^\star}{p_{0_1}} \frac{p_{0_1}}{p_e} \right)^2 \frac{T_e}{T_0} \frac{T_0}{T^\star}$$

The total pressure p_{0_1} *before* the shock and *constant* total temperature T_0 have been added. Substitution of the isentropic flow relations for the temperature ratios T_e/T_0 and $T_0/T^\star$ and pressure ratio $p^\star/p_0$ yields

$$M_e^2 \left(1 + \frac{\gamma - 1}{2} M_e^2 \right) = \left(\frac{A^\star}{A_e} \frac{p_{0_1}}{p_e} \right)^2 \left(\frac{2}{\gamma + 1} \right)^{\frac{\gamma+1}{\gamma-1}}$$

This quadratic equation is algebraically solved with

$$a = \frac{\gamma - 1}{2}, \quad b = 1, \quad c = -\left(\frac{A^\star}{A_e} \frac{p_{0_1}}{p_e} \right)^2 \left(\frac{2}{\gamma + 1} \right)^{\frac{\gamma+1}{\gamma-1}}$$

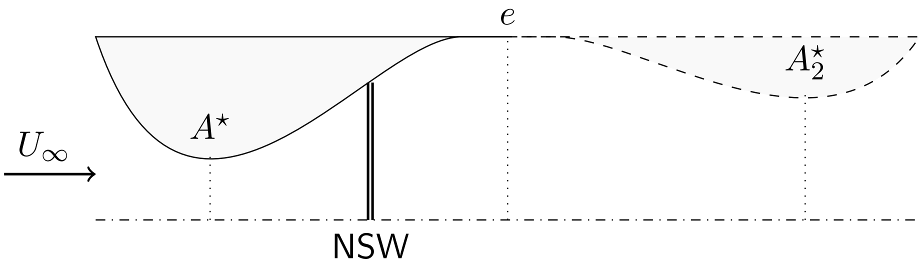

Figure A.1: A nozzle with two throats and a normal shock wave (NSW).

$$M_e^2 = \frac{\sqrt{b^2-4ac}-b}{2a} = \frac{\sqrt{1+2(\gamma-1)\left(\frac{A^\star}{A_e}\frac{p_{0_1}}{p_e}\right)^2\left(\frac{2}{\gamma+1}\right)^{\frac{\gamma+1}{\gamma-1}}}-1}{\gamma-1}$$

Bibliography

John D. Anderson, Jr. *Computational Fluid Dynamics: The Basics with Applications*. McGraw-Hill, 1995. ISBN: 0-07-113210-4.

John D. Anderson, Jr. *Modern Compressible Flow: With historical Perspective*. McGraw-Hill, 3rd edition, 2003.

John D. Anderson, Jr. *Fundamentals of Aerodynamics*. McGraw-Hill, fifth edition, 2011.

John D. Anderson Jr. Hypersonic and high-temperature gas dynamics, 2006. ISBN: 978-1-56347-780-5.

ANSYS. *ANSYS FLUENT User's Guide*. ANSYS Inc., Canonsburg, PA, 2010.

Arup, BCI, TNO, and VINU. Main report: Hyperloop in the Netherlands. Technical report, TNO, 2017. Report nr. 2017 R10715. Download link.

Arturo Baron, Michele Mossi, and Stefano Sibilla. The alleviation of the aerodynamic drag and wave effects of high-speed trains in very long tunnels. *Journal of Wind Engineering and Industrial Aerodynamics*, 89(5):365–401, 2001. ISSN 0167-6105. doi: https://doi.org/10.1016/S0167-6105(00)00071-4. URL http://www.sciencedirect.com/science/article/pii/S0167610500000714.

Adel M. Benselama, Mame J.-P. William-Louis, François Monnoyer, and Christophe Proust. A numerical study of the evolution of the blast wave shape in tunnels. *Journal of Hazardous Materials*, 181:609–616, 2010. DOI: https://doi.org/10.1016/j.jhazmat.2010.05.056.

C. Binder, M. Kinell, E. Utriainen, D. Eriksson, M. Bahador, J. Kneer, and H. Bauer. Experimental study on pressure losses in circular orifices for the application in internal cooling systems. *Journal of Turbomachinery*, 137(3):031005, 2015. doi: 10.1115/1.4028347. URL https://doi.org/10.1115/1.4028347.

James Braun, Jorge Sousa, and Cem Pekardan. Aerodynamic design and analysis of the hyperloop. *AIAA Journal*, 55(12):4053–4060, 2017. doi: 10.2514/1.J055634. URL https://doi.org/10.2514/1.J055634.

Harold L Brode. Blast wave from a spherical charge. *The Physics of Fluids*, 2(2):217–229, 1959.

F. Chen, A. Allou, Q. Douasbin, L. Selle, and J.D. Parisse. Influence of straight nozzle geometry on the supersonic under-expanded gas jets. *Nuclear Engineering and Design*, 339:92–104, 2018. ISSN 0029-5493. doi: https://doi.org/10.1016/j.nucengdes.2018.09.003. URL https://www.sciencedirect.com/science/article/pii/S0029549318309919.

W. Chester. Cxlv. the quasi-cylindrical shock tube. *The London, Edinburgh, and Dublin Philosophical Magazine and Journal of Science*, 45(371):1293–1301, 1954. doi: 10.1080/14786441208561138. URL https://doi.org/10.1080/14786441208561138.

R. F. Chisnell. The motion of a shock wave in a channel, with applications to cylindrical and spherical shock waves. *Journal of Fluid Mechanics*, 2(3):286—298, 1957. doi: 10.1017/S0022112057000130.

B. E. L. Deckker and Y. F. Chang. Paper 7: An investigation of steady compressible flow through thick orifices. *Proceedings of the Institution of Mechanical Engineers, Conference Proceedings*, 180(10):312–323, 1965. doi: 10.1243/PIME_CONF_1965_180_307_02. URL https://doi.org/10.1243/PIME_CONF_1965_180_307_02.

Erwin Franquet, Vincent Perrier, Stéphane Gibout, and Pascal Bruel. Free underexpanded jets in a quiescent medium: A review. *Progress in Aerospace Sciences*, 77:25–53, 2015. ISSN 0376-0421. doi: https://doi.org/10.1016/j.paerosci.2015.06.006. URL http://www.sciencedirect.com/science/article/pii/S0376042115000548.

Frederick Gerard Friedlander. The diffraction of sound pulses i. diffraction by a semi-infinite plane. *Proc. R. Soc. Lond.*, 186:322–344, 1946. ISSN 2053-9169. doi: http://doi.org/10.1098/rspa.1946.0046. URL http://royalsocietypublishing.org/doi/abs/10.1098/rspa.1946.0046.

J.M. Gay, G. Marbach, and W. Gulden. Response of ITER to loss of vacuum accidents. *Fusion Engineering and Design*, 42(1):89–93, 1998. ISSN 0920-3796. doi: https://doi.org/10.1016/S0920-3796(98)00145-8. URL http://www.sciencedirect.com/science/article/pii/S0920379698001458.

Esther Christine Goddard. Vacuum tube transportation system, 1945. US Patent no.: US2511979A. Download link.

T. Gélain, A. Rondeau, S. Peillon, J.C. Sabroux, and F. Gensdarmes. Cfd modelling of the wall friction velocity field in the iter tokamak resulting from airflow during a loss of vacuum accident—consequences for particle resuspension. *Fusion Engineering and Design*, 100:87–99, 2015. ISSN 0920-3796. doi: https://doi.org/10.1016/j.fusengdes.2015.04.043. URL http://www.sciencedirect.com/science/article/pii/S0920379615002720.

Hardt Hyperloop. Frequently asked questions. https://hardt.global/faq/, 2020. Accessed: April 11th, 2020 (Archive link).

Josef Henrych. *The dynamics of explosion and its use*. Elsevier Amsterdam, 1979.

Frank P. Incropera, David P. DeWitt, Theodore L. Bergman, and Adrienne S. Lavine. *Fundamentals of Heat and Mass Transfer*. John Wiley & Sons, 6th edition, 2006. ISBN: 0-471-45728-0.

Ryan Janzen. TransPod ultra-high-speed tube transportation: Dynamics of vehicles and infrastructure. *Procedia Engineering*, 199:8–17, 2017. DOI: `https://doi.org/10.1016/j.proeng.2017.09.142`.

W. Jitschin, M. Ronzheimer, and S. Khodabakhshi. Gas flow measurement by means of orifices and Venturi tubes. *Vacuum*, 53:181–185, 1999. DOI: `https://doi.org/10.1016/S0042-207X(98)00352-2`.

Arthur Kantrowitz and Coleman Dup Donaldson. Preliminary investigation of supersonic diffusers. Technical report, National Advisory Committee on Aeronautics (NASA), 1945. Download link.

Vasilis Karlos, George Solomos, and Martin Larcher. Analysis of the blast wave decay coefficient using the kingery–bulmash data. *International Journal of Protective Structures*, 7(3):409–429, 2016.

Tae-Kyung Kim, Kyu-Hong Kim, and Hyeok-Bin Kwon. Aerodynamic characteristics of a tube train. *Journal of Wind Engineering and Industrial Aerodynamics*, 99(12):1187–1196, 2011. ISSN 0167-6105. doi: https://doi.org/10.1016/j.jweia.2011.09.001. URL `http://www.sciencedirect.com/science/article/pii/S0167610511001723`.

Gilbert F Kinney and Kenneth J Graham. *Explosive shocks in air*. Springer Science & Business Media, 2013.

Xiaopeng Li, Rui Zhou, Wei Yao, and Xuejun Fan. Flow characteristic of highly underexpanded jets from various nozzle geometries. *Applied Thermal Engineering*, 125:240 — 253, 2017. DOI: `https://doi.org/10.1016/j.applthermaleng.2017.07.002`.

Kevin William Linfield. *A study of the discharge coefficient of jets from angled slots and conical orifices*. PhD thesis, University of Toronto, 2000. Download link.

Ivan Lupelli, Pasquale Gaudio, Michela Gelfusa, Andrea Malizia, Ivan Belluzzo, and Maria Richetta. Numerical study of air jet flow field during a loss of vacuum. *Fusion Engineering and Design*, 89(9):2048–2052, 2014. ISSN 0920-3796. doi: https://doi.org/10.1016/j.fusengdes.2014.03.064. URL `http://www.sciencedirect.com/science/article/pii/S0920379614002439`. Proceedings of the 11th International Symposium on Fusion Nuclear Technology-11 (ISFNT-11) Barcelona, Spain, 15-20 September, 2013.

James N Moss and Graeme A Bird. Direct simulation of transitional flow for hypersonic reentry conditions. *Journal of spacecraft and rockets*, 40(5):830–843, 2003.

Elon Reeve Musk. Hyperloop alpha. Technical report, SpaceX, 2013. `https://www.spacex.com/sites/spacex/files/hyperloop_alpha.pdf`.

Max M. J. Opgenoord and Philip C. Caplan. Aerodynamic design of the hyperloop concept. *AIAA Journal*, 56(11):4261–4270, 2018. doi: 10.2514/1.J057103. URL `https://doi.org/10.2514/1.J057103`.

Daryl Oster, Masayuki Kumada, and Yaoping Zhang. Evacuated tube transport technologies (ET3)$^{\mathrm{TM}}$: a maximum value global transportation network for passengers and cargo. *Journal of Modern Transportation*, 19(1):42–50, 2011. DOI: `https://doi.org/10.1007/BF03325739`.

J. Patterson, N.W. Page, and J.B. Ritchie. Contraction coefficients for compressible flow through axisymmetric orifices. *International Journal of Mechanical Sciences*, 12(5):405–415, 1970. ISSN 0020-7403. doi: https://doi.org/10.1016/0020-7403(70)90103-7. URL http://www.sciencedirect.com/science/article/pii/0020740370901037.

Matei I. Radulescu and Chung K. Law. The transient start of supersonic jets. *Journal of Fluid Mechanics*, 578:331—369, 2007. doi: 10.1017/S0022112007004715.

Raghu S. Raghunathan, H.-D. Kim, and T. Setoguchi. Aerodynamics of high-speed railway train. *Aerospace Sciences*, 38:469–514, 2002. DOI: https://doi.org/10.1016/S0376-0421(02)00029-5.

E. Rajakuperan and M. A. Ramaswamy. An experimental investigation of underexpanded jets from oval sonic nozzles. *Experiments in Fluids*, 24(4):291–299, 1998. ISSN 1432-1114. doi: 10.1007/s003480050176. URL https://doi.org/10.1007/s003480050176. DOI: https://doi.org/10.1007/s003480050176.

Julien Ridoux, Nicolas Lardjane, Laurent Monasse, and François Coulouvrat. Beyond the limitation of geometrical shock dynamics for diffraction over wedges. *Shock Waves*, 29(6):833–855, 2019. doi: https://doi.org/10.1007/s00193-018-00885-w.

Riccardo Rossi, Jean-François Ciparisse, Pasquale Gaudio, and Andrea Malizia. A scaling law of pressurisation time in the case of loss of vacuum accidents (lovas): Theoretical and experimental analysis. *Fusion Engineering and Design*, 143:16–23, 2019. ISSN 0920-3796. doi: https://doi.org/10.1016/j.fusengdes.2019.03.112. URL http://www.sciencedirect.com/science/article/pii/S0920379619304454.

R. M. Salter. The very high speed transit system. Technical report, Rand Corporation, 1972. Report nr. P-4874. https://www.rand.org/content/dam/rand/pubs/papers/2008/P4874.pdf.

L.I. Sedov. Propagation of strong blast waves. *Journal of Applied Mathematics and Mechanics*, 10:241–250, 1946.

M. Silvestrini, B. Genova, and F.J. Leon Trujillo. Energy concentration factor. a simple concept for the prediction of blast propagation in partially confined geometries. *Journal of Loss Prevention in the Process Industries*, 22(4):449–454, 2009. ISSN 0950-4230. doi: https://doi.org/10.1016/j.jlp.2009.02.018. URL https://www.sciencedirect.com/science/article/pii/S0950423009000382.

B. W. Skews. The shape of a diffracting shock wave. *Journal of Fluid Mechanics*, 29(2):297—304, 1967. doi: 10.1017/S0022112067000825.

S. A. Sloan and M. A. Nettleton. A model for the axial decay of a shock wave in a large abrupt area change. *Journal of Fluid Mechanics*, 71(4):769—784, 1975. doi: 10.1017/S0022112075002844.

SpaceX. *2019 SpaceX Hyperloop Pod Competition — Rules and Requirements*. Space Exploration Technologies Corp., Hawthorne, California, 2018. Download link.

SwissMetro. Hauptstudie 94–98. Technical report, Elektrowatt Engineering, 1999. Download link.

K. Takayama, A. Sasoh, O. Onodera, R. Kaneko, and Y. Matsui. Experimental investigation on tunnel sonic boom. *Shock waves*, 5:127–138, 1995. DOI: `https://doi.org/10.1007/BF01435520`.

G. I. Taylor. The formation of a blast wave by a very intensive explosion i. theoretical discussion. *Proceedings of the Royal Society of London*, 201(1065):159–174, 1950. doi: https://doi.org/10.1098/rspa.1950.0049.

Virgin Hyperloop One. Facts & frequently asked questions. `https://hyperloop-one.com/facts-frequently-asked-questions`, 2020. Accessed: April 11th, 2020 (Archive link).

J. von Neumann. Blast wave, the point source solution. Technical Report LA-2000, LOS ALAMOS SCIENTIFIC LABORATORY, 1947. Download link.

V. Vuorinen, J. Yu, S. Tirunagari, O. Kaario, M. Larmi, C. Duwig, , and B. J. Boersma. Large-eddy simulation of highly underexpanded transient gas jets. *Phys. Fluids*, 25, 2013. DOI: `https://doi.org/10.1063/1.4772192`.

A.J Ward-Smith. Critical flowmetering: The characteristics of cylindrical nozzles with sharp upstream edges. *International Journal of Heat and Fluid Flow*, 1(3):123–132, 1979. ISSN 0142-727X. doi: https://doi.org/10.1016/0142-727X(79)90028-6. URL `https://www.sciencedirect.com/science/article/pii/0142727X79900286`.

Frank M. White. *Viscous Fluid Flow*. McGraw-Hill, third edition, 2006.

G. B. Whitham. On the propagation of shock waves through regions of non-uniform area or flow. *Journal of Fluid Mechanics*, 4(4):337–360, 1958. doi: 10.1017/S0022112058000495.

Felix T. H. Wong. Aerodynamic design and optimization of a hyperloop vehicle. Master's thesis, TU Delft, 2018. Download link.

Youyou Xu, Songlin Liu, Xuebin Ma, Xiaoman Cheng, Kecheng Jiang, and Xiaokang Zhang. Numerical simulation of airflow characteristics during the loss of vacuum accident of CFETR. *International Journal of Hydrogen Energy*, 43(24):11160–11172, 2018. ISSN 0360-3199. doi: https://doi.org/10.1016/j.ijhydene.2018.04.228. URL `http://www.sciencedirect.com/science/article/pii/S0360319918314526`.

Youyou Xu, Songlin Liu, Xiaoman Cheng, and Xuebin Ma. Numerical analysis of loss of vacuum accident (lova) and preliminary discussion about dust resuspension for cfetr. *Fusion Engineering and Design*, 143:82–90, 2019. ISSN 0920-3796. doi: https://doi.org/10.1016/j.fusengdes.2019.03.159. URL `http://www.sciencedirect.com/science/article/pii/S0920379619304922`.